

DISS. ETH No. 29075

VAN DER WAALS HETEROSTRUCTURES  
FOR INTEGRATED ON-CHIP  
PHOTONICS

A thesis submitted to attain the degree of  
DOCTOR OF SCIENCES OF ETH ZURICH  
(Dr. sc. ETH Zurich)

presented by

RONJA TAMAR KHELIFA

M.Sc., Albert-Ludwigs University, Freiburg, Germany

born on 03.07.1991

citizen of Germany

accepted on the recommendation of  
Prof. Dr. Lukas Novotny, examiner  
Prof. Dr. Alexandre Bouhelier, co-examiner  
Prof. Dr. Juerg Leuthold, co-examiner

2023

This work was carried out at the  
*Photonics Laboratory,*  
*Department of Information Technology and Electrical Engineering,*  
*ETH Zurich*

---

## Acknowledgments

This PhD has been a long journey. A journey with wonderful moments, filled with joy, fascination, excitement, enthusiasm, fun, and teamwork. But also challenging moments, filled with bad surprises, struggle, frustration, disappointment, endurance, resilience, and tears. The beautiful part those moments almost all have in common is that I was allowed to share them with other people and was never left alone. Here, I want to take the time to thank all the people that have been important for me during the last years.

First, I would like to thank Lukas for giving me the opportunity to join the Photonics Lab and for being my mentor. I think that part of my PhD journey might have challenged you and the Photonics Lab from a different and new side. I am grateful and happy that together we have managed to face and deal with these extraordinary circumstances. Thank you for an inspiring, trusting environment with a good balance of guidance and freedom that allows to realize the PhD project as part of the group and yet independently.

In this concern, I am also extremely thankful for your support, Barbara. Thank you – not only for your help in all organizational matters but also for being so rational and professional while at the same time supporting me emotionally.

I am no less grateful to the rest of the group, former as well as new group

## Acknowledgments

---

members. Thanks for an environment that allowed focused work but also fun coffee breaks, merendas, kicker games, and balcony beers. I want to thank the newbies (Anna, Sotos, Fons, Alfonso, Cla, Andrei (and Eric)) who have started and ended the PhD journey at similar times and whom I shared good and bad experiences with. Especially my two most important 2Dler, Anna and Sotos: I am so happy that I have had both of you with me on this journey – thank you so much! I want to thank all my office mates for the fun atmosphere we always had. Thank you, Alfonso, for your positivity and your nice and motivating words that have often made me smile. Mo, thank you so much for being my go-to person, when I needed advice, for listening to me, my concerns, and my thoughts. Your direct and realistic input has helped me so many times. Klaus, you cannot believe how happy I am that you have been my first direct supervisor in the Photonics lab. Thanks for your perfectly loose guidance, your support, and introductions, especially the long E-Beam sessions with interesting discussions. I will keep the Photonics Lab in great memory, and I am so happy that many of you have become friends whom I will also share some next adventures with.

Lastly, I want to thank my family and friends. I am a person, who can only succeed within a loving, fruitful, busy, honest, supportive, and active environment. For this I want to thank all my friends from back home, in Freiburg and newer friends from Zurich. Thanks for listening to me and for distracting me whenever necessary.

I am lucky to have an amazing diverse and large family, distributed throughout the whole world. Thank you all! Not to forget, I would like to thank my grandparents, who were not in our world during my PhD years, but nevertheless did their part even before then. With their input, their support, their love, and their further and different perspectives they have helped me lay foundations to become the person I am now.

But most importantly I want to thank my parents, Frieda and Gilles and my sister Mariam. Thank you for always being there for me. Thank you for your love and your constant support in whatever I decide is good for me. What

I appreciate most within this loving environment, is your honest questioning to help me be as happy as possible while finding the best path for me and us.

Last but not least, I want to thank you, Julian. I know that at times the last few years have been as difficult for you as they have been for me. I thank you so much for helping me in every aspect to master the challenges, while still making sure that whenever necessary I have distraction and take care of myself and us. I love the life we have built up together and I am looking so forward to our next adventures.



---

## Abstract

In the field of nanophotonics, one important goal is optical information processing with photonic integrated circuits. Substantial research efforts have led to significant advances in the integration of active and passive devices into photonic circuits. Yet to this day, it is still a challenge to integrate one of the most important components: light sources. In this thesis, we demonstrate on-chip integration of optically and electrically driven light sources in a photonics platform solely based on van der Waals (vdW) heterostructures. These heterostructures are assembled from two-dimensional materials that provide a promising platform to engineer structures with desired optoelectronic properties. As first devices, we sandwich monolayer transition metal dichalcogenides (TMDs) as active material between slabs of the dielectric material hexagonal boron nitride (h-BN) and pattern the vdW stack into waveguide-coupled disk resonators. We demonstrate cavity-coupled emission from intralayer excitons in a monolayer TMD, as well as from interlayer excitons in a heterobilayer of two dissimilar monolayer TMDs. The integration directly inside the light-confining h-BN allows us to place the active materials in areas of high optical field intensity, thereby improving the mode overlap. Furthermore, in a single vdW heterostructure we combine light-emitting devices (LEDs) based on recombination of excitons in TMDs with photonic waveguides made of h-BN. Waveguide-coupled emission is obtained by embedding the LED between two thick h-BN layers and patterning the vdW stack into the desired photonic structure. Our work on on-chip light generation and waveguiding illustrates a promising platform for integrated vdW photonics and optoelectronics.





---

## Zusammenfassung

Informationsverarbeitung mit Hilfe integrierter optischer Schaltungen ist ein wesentliches Ziel der Nanophotonik. Intensive Forschung hat bemerkenswerte Fortschritte bei der Integration aktiver und passiver Bauteile in photonischen Schaltkreisen hervorgebracht. Dennoch ist es stets eine Herausforderung, eine der zentralsten Komponenten, nämlich Lichtquellen zu integrieren. In dieser Arbeit präsentieren wir eine Plattform, welche die “on-Chip-Integration” von optisch und elektrisch angeregten Lichtquellen ermöglicht. Unsere Plattform basiert ausschliesslich auf van-der-Waals (vdW)-Heterostrukturen, welche aus verschiedenen zweidimensionalen (2D) Materialien aufgebaut sind. 2D Materialien, wie zum Beispiel Übergangsmetall-Dichalcogenide (TMDs) und hexagonales Bornitrid (h-BN), sind eine vielversprechende Materialklasse. Sie ermöglichen unter anderem Flexibilität beim Design von optoelektronischen Bauteilen. Als erste Struktur fügen wir Monolagen von TMDs zwischen zwei Schichten h-BN ein und strukturieren den resultierenden Stapel direkt in wellenleitergekoppelte Scheibenresonatoren (engl.: disk resonators). Dabei zeigen wir die Kopplung von Intralayer Exzitonen aus TMD Monolagen und von Interlayer Exzitonen die in einer Heteroschicht aus Monolagen zweier unterschiedlicher TMDs entstehen, an die Scheibenresonatoren. Die Integration direkt im Dielektrikum (h-BN) ermöglicht es uns, die aktiven Materialien in Bereichen mit hoher optischer Feldintensität zu positionieren und so die Überlappung der Moden zu verbessern. Zusätzlich zeigen wir wellenleitergekoppelte, elektrisch betriebene Lichtquellen. In einer

vdW-Heterostruktur werden lichtemittierende Bauelemente (LEDs), die auf Exzitonenrekombination in Monolagen von TMDs basieren, mit photonischen h-BN-Wellenleitern kombiniert. Die wellenleitergekoppelte Lichtemission wird erzielt, indem die LED zwischen zwei h-BN Schichten eingebettet und der gesamte vdW-Stapel zu einer photonischen Struktur strukturiert wird. Insgesamt kombiniert die beschriebene Plattform zwei wesentliche Eigenschaften: 1) eine verbesserte optische Modenüberlappung und 2) Wellenleiterkopplung. Die hier präsentierte Lichterzeugung und -wellenleitung stellt daher eine vielversprechende Plattform für on-Chip-vdW-Photonik und integrierte Optoelektronik dar.

---

## Foreword

Over the past four and a half years, I have received constant support, for which I am very grateful. At this point, I would like to highlight the contributions of other people that have been essential to this work. Especially at the beginning of my PhD, the introductions and mentoring by others were very important and helpful. For this, I acknowledge the supervision by Nikolaus Flöry, Achint Jain, Patrick Back, Markus Parzefall, and Lukas Novotny. Furthermore, the latter two initiated this project. The starting point of the recipe developed for the etching of h-BN disks was set by Konstantin Malchow and Markus Parzefall. Shadi Nashashibi has developed COMSOL simulations and Matlab scripts that laid the foundation for the optimization of the h-BN disk radii. Dominik Windey advised me on Python programming. Patrick Back stacked the heterostructure discussed in chapter 4 in the glovebox of the group of Prof. Ataç İmamoğlu at ETH Zurich. I performed all cleanroom fabrication processes in the FIRST-Lab of ETH Zurich. For the work discussed in chapter 5, I thank Shengyu Shan for the collaboration. Specifically, I want to point out that she performed a big part of the fabrication steps that required the cleanroom or the use of chemicals. Furthermore, she developed in her master thesis (supervised by Lujun Wang and me) an electron beam lithography recipe that was used for one fabrication step of the devices in chapter 5. She also performed the photoluminescence measurement, shown in Fig. 5.5d. The Blender images of the atomic lattices in Fig. 1.1 were made by Sotirios Papadopoulos. The transmission measurement plotted as a comparison in Fig. 5.11c was performed

by Antti Moilanen. The measurements to correct the spectra for the transmission characteristics of the setup were performed by Anna Kuzmina, Yang Xu and Yesim Koyaz. Anna Kuzmina, Ueli Koch, Antti Moilanen, Shadi Nashashibi, Shengyu Shan, Nikolaus Flöry, Moritz Cavigelli, Laura Shaw and Julian Müller proofread and corrected parts of this thesis. Overall I want to additionally acknowledge the discussions and input received by Sebastian Heeg, Rene Reinmann, Anna Kuzmina, Sotirios Papadopoulos, Lujun Wang, Shengyu Shan and Sebastian Busschaert. I thank Stefan Köppli for inspiring discussions and ideas regarding the integration of our platform with silicon photonics. During the last year, Ueli Koch, supported me as a co-advisor, for which I am very grateful. Moreover, for the last months Sotirios Papadopoulos and I have had daily meetings to discuss details of our theses and the writing progress; I greatly appreciate his help. Lastly, I want to point out that this thesis is based on publications that were collaboratively written with the co-authors.\* Whenever a chapter or section is largely based on a publication, it is indicated. However, in order to optimize the flow of this thesis, parts of the publications are adapted and also included in other sections of the thesis.

---

\*R. Khelifa, P. Back, N. Flöry, S. Nashashibi, K. Malchow, T. Taniguchi, K. Watanabe, and L. Novotny. *Coupling Interlayer Excitons to Whispering Gallery Modes in van der Waals Heterostructures*, *Nano Letters*, **20**, 6155-6161 (2020).

R. Khelifa<sup>†</sup>, S. Shan<sup>†</sup>, A. J. Moilanen, T. Taniguchi, K. Watanabe, and L. Novotny. *WSe<sub>2</sub> Light-Emitting Device Coupled to an h-BN Waveguide*, *ACS Photonics*, **10**, 1328-1333 (2023).

<sup>†</sup> These two authors contributed equally.

---

# Contents

<b>Acknowledgments</b>	<b>i</b>
<b>Abstract</b>	<b>v</b>
<b>Zusammenfassung</b>	<b>vii</b>
<b>Foreword</b>	<b>ix</b>
<b>Introduction</b>	<b>1</b>
<b>1 Two-dimensional (2D) materials and van der Waals (vdW) heterostructures</b>	<b>7</b>
1.1 Graphene (Gr)	9
1.2 Hexagonal boron nitride (h-BN)	9
1.3 Transition metal dichalcogenides (TMDs)	11
1.4 Heterobilayer (HBL) of two dissimilar monolayer TMDs	14
1.5 TMD based LEDs	16
<b>2 On-chip h-BN photonic structures</b>	<b>19</b>
2.1 Fundamentals	20
2.2 h-BN photonics	24
2.3 Integration of TMD-based emitters with h-BN photonic structures	29
2.4 Conclusion	33

<b>3</b>	<b>Integration of monolayer TMDs inside h-BN-based disk resonators</b>	<b>35</b>
3.1	Device concept	36
3.2	Optical characterization	38
3.3	Comparison to evanescent coupling (on top)	39
3.4	Conclusion	42
<b>4</b>	<b>Coupling interlayer excitons to whispering gallery modes (WGMs) of h-BN disk resonators</b>	<b>43</b>
4.1	Device concept and design optimization	44
4.2	Optical characterization	46
4.3	Conclusion	51
<b>5</b>	<b>Waveguide-coupled exciton LEDs</b>	<b>53</b>
5.1	Device concept and design	54
5.2	Optoelectronic characterization of the unpatterned exciton LED	59
5.3	Optoelectronic characterization of the waveguide-coupled exciton LED	61
5.4	Conclusion	71
<b>6</b>	<b>Conclusions &amp; Outlook</b>	<b>73</b>
6.1	Conclusions	73
6.2	Outlook	74
<b>A</b>	<b>Appendix</b>	<b>81</b>
	<b>References</b>	<b>103</b>
	<b>List of Publication</b>	<b>121</b>
	<b>Curriculum Vitae</b>	<b>123</b>

---

## Introduction

Modern life without the use of the internet or telecommunication is no longer imaginable. Friends, family and professional contacts are spread all over the world. And yet we are more connected than ever before. Without questioning it, our daily life relies more and more on information and communications technology (ICT), which is associated with a strong growth in data traffic [1]. The drastic increase has been further forced by the COVID-19 pandemic, which propelled digitalization through isolation at home, remote work and video calls [2]. Estimates anticipate that the growing ICT sector might take over more than 20 % of the worldwide energy consumption in 2030 [3, 4]. While our interconnected world pushes the need for further expansion and speed improvements, global warming compels a more sustainable lifestyle. These two almost contradictory demands impose high requirements on the technological advancements in this field.

One promising technology for meeting both requirements is photonics – not only for long-range data transmission via optical fibers, but also at the chip level. On-chip photonics is expected to further advance applications and to increase data rates, while consuming minimal power and lowering the cost [5–7]. Also other fields benefit from the developments of photonic integrated circuits (PICs). Examples are sensing applications for medical diagnostics and environmental monitoring [8, 9].

Different platforms for PICs have evolved during the last decades. In particular silicon (Si) photonics, based on integrated circuits in Si-on-insulator (SOI) or Si nitride (SiN), has evolved as a leading architecture. The main reason for this are the mature fabrication processes that have been developed for complementary metal-oxide semiconductor (CMOS) technology, which enable dense integration and compatibility with microelectronics [10, 11]. While SOI PICs are mainly of interest for the ICT sector in the relevant telecommunication wavelengths, SiN offers a broader transparency window and is therefore also useful for applications in the visible range [12]. However, Si's weak intrinsic electro-optic effect and its indirect band gap introduce challenges for the development of integrated active devices such as modulators and light sources [11]. This led to the growth of other material platforms, such as for example, lithium niobate (LN). The fairly strong intrinsic electro-optic effect of LN has made it a promising material for integrated modulators [13, 14]. Moreover, due to its broad optical transparency and the advances of the LN on insulator (LNOI) platform, it also has evolved as a relevant platform for large-scale PICs [15].

However, for both of these material platforms, the efficient integration of light sources has remained a challenge [15, 16]. An attractive path is the integration of other material classes with better light emission properties. Commonly, for example, III-V semiconductor light sources are combined with Si PICs by using heterogeneous integration, which involves complex fabrication methods such as wafer bonding [16, 17]. Two-dimensional (2D) materials are a suitable material class, which have demonstrated great promise for integrated optoelectronic devices [18–21]. The fabrication process could be simplified, as 2D materials can be placed on pre-patterned photonic structures without constraints of lattice matching [22]. Photodetectors based on Graphene (Gr) or transition-metal dichalcogenides (TMDs) have reached high-speed performance [23, 24] and large photoresponsivities [25–27]. Furthermore, 2D material-based modulators have been integrated with on-chip photonic circuits [28, 29]. In 2017 Bie et al. demonstrated a TMD-based light emitting diode that was integrated with a prepatterned Si-based waveguide [19]. Recently an electrically driven emitter was coupled to a CdS Nanoribbon, which could



act as the waveguiding medium [30].

The low number of demonstrations of 2D-based waveguide-integrated light sources is surprising, given the extensive research efforts that have been put into the design of novel light emitting devices [31, 32]. To build these, van der Waals (vdW) heterostructures with smooth interfaces between layers can be formed by the vertical assembly of different 2D materials. They can be stacked without lattice matching requirements because neighboring layers of 2D materials are held together by weak vdW forces, allowing a new degree of freedom in device architecture [33, 34]. Band structure engineering with atomic precision enables the design of Schottky junctions [35, 36], light emitting quantum wells [37, 38], p–n diodes [39–41], as well as tunnel junctions [42]. Furthermore, light emitting devices with intriguing properties like polarization control [43], fast modulation speed [44] and single photon emission [45] have been demonstrated.

In most devices, the light emitters are based on TMDs, a semiconducting class of the 2D material family. Like all 2D materials, TMDs can be thinned down to a single monolayer. In contrast to their bulk counterpart, in the single-layer form, TMDs can exhibit a direct band gap with exciton emission at room temperature [46, 47]. This makes TMD monolayers excellent candidates not only for optoelectronic devices but also for integration with optical cavities for enhanced light-matter interactions [48–54].

By combining two dissimilar TMD monolayers into a heterobilayer (HBL), interlayer excitons with spatially separated electrons and holes can be formed [55]. Their charge carrier dynamics [56] and electrically tunable exciton resonances [55, 57] are providing fascinating possibilities for materials engineering. While monolayer TMDs emit in the visible to near-infrared (IR) range [58, 59], interlayer exciton emission can extend even further towards the IR [60]. Motivated by a growing interest in nanolasers, interlayer excitons were coupled to Si-based photonic crystals [61], as well as grating cavities [62], to realize surface emitting, optically pumped lasers at room-temperature.

Co-integration of 2D optoelectronic devices with on-chip photonics was

demonstrated by placing 2D materials onto Si-based waveguides in order to couple via evanescent fields [19, 24, 25, 63]. The coupling strength obtained in this manner is modest because in such architectures the TMD is not placed at the highest field intensity, which is found inside the light confining dielectric medium. Plasmonic structures or photonic cavities have been used to improve device functionalities such as the responsivity of waveguide-integrated photodetectors [23, 64]. A second approach to enhance the light-matter interaction is the integration of active layers directly inside dielectric waveguides or resonators to reach improved mode overlap [49, 65, 66]. For systems with optical excitation, this was demonstrated, for example, by embedding a monolayer TMD as the active material inside a free-standing microdisk made of  $\text{Si}_3\text{N}_4$ /hydrogen silsesquioxane (HSQ) [49]. This approach can be adopted for photonic structures entirely made of 2D materials: the lattice independent stacking of vdW materials allows the sandwiching of monolayers or heterostructures of 2D materials between thick layers of a dielectric 2D material.

To accomplish this, hexagonal boron nitride (h-BN), a dielectric 2D material, has been proposed as a confinement layer for on-chip photonics with integrated optoelectronic devices [67]. It has emerged as an attractive candidate to fabricate photonic structures [68–70], for which it has further been shown that quantum emitters can be monolithically integrated [71, 72]. First integrations have been achieved with monolayer TMDs sandwiched inside h-BN disks to couple exciton photoluminescence (PL) to the resonator modes [65]. However, in these integrated structures the disk is freestanding and is not easily compatible with on-chip photonics. Furthermore, these structures require optical excitation with external lasers, which impedes full-scale integration.

## Thesis Outline

In this thesis, we exploit the diversity of the 2D materials family to further advance the integrated on-chip photonics platform solely based on vdW heterostructures. We couple TMD-based optically excited emitters to whispering gallery modes (WGMs) in waveguide-coupled disk resonators. The

platform is then further expanded by the demonstration of waveguide-integrated electrically-driven light sources. Our approach combines two important attributes: 1) an enhanced optical mode overlap and 2) waveguide coupling for on-chip integration. In this work, we focus on the demonstration of integrated structures in the visible to near-IR range (660 – 920 nm).

In **chapter 1** we present the first building block of the integrated platform: 2D materials and their heterostructures. We describe the fundamental basics of h-BN, Gr and TMDs. Focus is placed on vdW heterostructures with monolayer TMDs. We discuss interlayer excitons that can be formed in HBLs of two dissimilar monolayer TMDs and introduce TMD-based exciton light emitting devices (LEDs).

As the second building block of the presented platform, in **chapter 2** we introduce passive photonic structures made of h-BN. Basic theoretical properties of waveguiding and WGMs in disk resonators are discussed and first measurements of h-BN waveguides and waveguide-coupled disk resonators are presented. Furthermore, h-BN is introduced as a light confining dielectric for the integration of active devices inside the vertical center of photonic structures.

After the introduction of the individual building blocks, in **chapter 3** we finally combine vdW heterostructures and h-BN photonics to present the first integrated device concept. We integrate monolayer TMDs inside the vertical center of a waveguide-coupled h-BN disk resonator at high field intensities and demonstrate cavity-coupled exciton PL. We then compare the integration at high field intensities to an evanescently coupled device with a monolayer TMD placed on top.

In **chapter 4** the waveguide-coupled disk resonators are further advanced by integrating a HBL of two dissimilar TMDs. We thereby demonstrate cavity-coupled emission from interlayer excitons.

Lastly, in **chapter 5** we turn to the integration of electrically-driven LEDs with h-BN photonic waveguides. We use the same approach as for the optically

excited systems and integrate the TMD-based LEDs inside h-BN waveguide structures to achieve a high mode overlap.

In **chapter 6**, we summarize the results of this work and discuss future device optimizations. Further developments of the introduced platform by integrating other vdW-based optoelectronic devices and the expansion of the platform to longer wavelength ranges are proposed.

\*

---

\*This introduction is in part adapted from the article R. Khelifa, P. Back, N. Flöry, S. Nashashibi, K. Malchow, T. Taniguchi, K. Watanabe, and L. Novotny. *Coupling Interlayer Excitons to Whispering Gallery Modes in van der Waals Heterostructures*, *Nano Letters*, **20**, 6155-6161 (2020). Adapted in part with permission from [73]. Copyright 2020 American Chemical Society.

# 1

---

## Two-dimensional (2D) materials and van der Waals (vdW) heterostructures

**2**D materials are crystalline materials with a layered structure. In these crystals, individual layers have strong covalent bonds, but adjacent layers are only weakly bonded by vdW forces [74]. This allows delamination from a bulk crystal into a small number of layers or even monolayers, while maintaining the crystalline structure within the individual layer. A typical method for obtaining monolayers is exfoliation, which uses a sticky scotch-tape to peel off individual layers from the bulk crystal [75, 76]. In recent years, 2D materials have also been grown by methods such as chemical vapor deposition (CVD) [77, 78].

The first experimental demonstration of high-quality few-layer and monolayer Gr was achieved by Geim and Novoselov (2004 and 2005) [75, 79]. In 2010, they received the Nobel prize for their discovery and studies on Gr [80], and research on 2D materials began to grow rapidly. The family of 2D materials was further explored and interesting properties of other 2D materials such as TMDs and h-BN were discovered [74, 81, 82]. One remarkable feature that

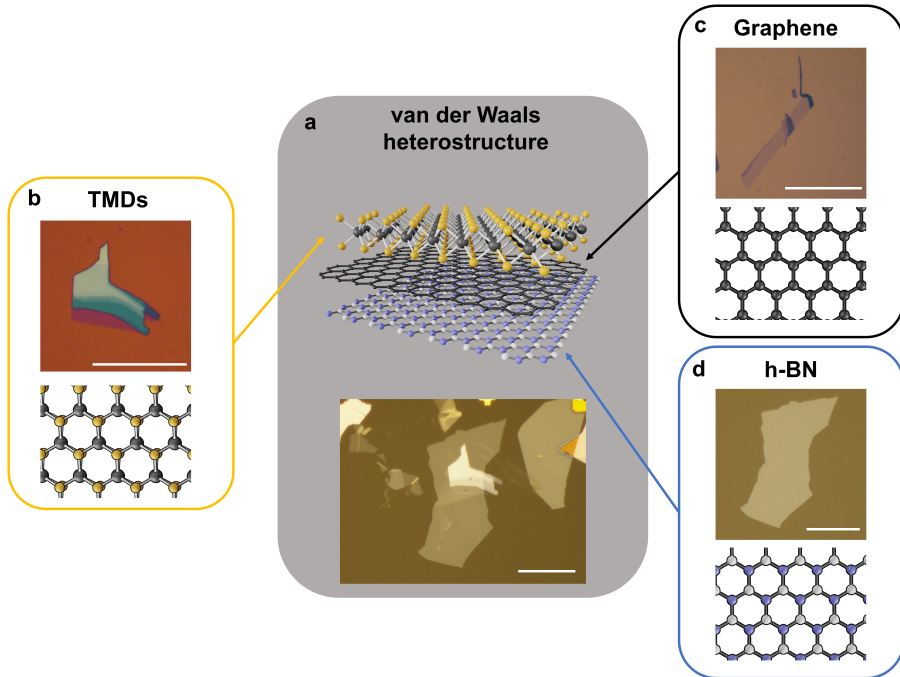


**Figure 1.1:** (a)\* Schematic illustration of a vdW heterostructure that consists of (b) TMDs (yellow), (c) Gr (black), and (d) h-BN (blue). And an optical microscope image of a heterostructure on a glass substrate after exfoliation. (b) Optical microscope image of an exfoliated TMD, the light purple part is a monolayer, whereas the attached white and blue regions are several layers. Below: top view of the crystallographic structure of a TMD. (c) A monolayer Gr flake and its corresponding crystal structure. (d) Multilayer h-BN flake and the crystal structure of a monolayer h-BN. The scale bar in every optical microscope image is 25  $\mu\text{m}$ .

they all share is the vertical assembly of different 2D materials to form so-called vdW heterostructures (cf. Fig. 1.1a\*). Adjacent layers are held together by weak vdW forces, which enables the stacking of dissimilar materials without constraints of lattice matching [33, 34]. Therefore, with the conducting material Gr, semiconducting TMDs and the insulating h-BN, the family of 2D materials opens up a new degree of freedom: layers with different electronic properties can be combined to design desired device architectures.

\*The illustrations of the atomic crystals were made by Sotirios Papadopoulos.

In this thesis, exfoliated 2D materials and the combination of them to vdW heterostructures form the first building block for the design of the integrated photonics platform. In the following, we introduce in more detail the 2D materials that are used throughout this thesis: Gr, h-BN and TMDs. We then discuss the combination of two dissimilar monolayer TMDs to form HBLs, and the design of LEDs based on emission from TMD monolayers.

## 1.1 Graphene (Gr)

Gr is the monolayer form of graphite, which consists of a single layer of carbon atoms that are arranged in a honeycomb lattice (cf. Fig. 1.1c). Besides its excellent thermal conductivity [83] and high mechanical robustness [84], the electronic properties of Gr are particularly exceptional [85]. The band structure has a linear dispersion relation, often called Dirac cone band structure. Gr is classified as a zero-band gap material because the valence and conduction band touch at the Dirac point. The associated transport properties of Gr are outstanding and high electron mobilities have been reported [86, 87]. This has made Gr an interesting candidate for high speed electronic and optoelectronic devices [23, 88]. However, the lack of a band gap limits the optoelectronic applications as it increases for example the dark current in photodetectors [24, 89].

The light absorption of monolayer Gr in the visible range is  $\sim 2.3\%$  [90]. The low absorption in the spectral range considered throughout this work (660 – 925 nm) [91, 92], combined with its good electrical conductivity, makes Gr a valuable material for electrodes of optoelectronic devices.

## 1.2 Hexagonal boron nitride (h-BN)

h-BN is an insulating 2D material that consists of boron and nitrogen atoms. As in Gr, these are arranged in a hexagonal lattice (see Fig. 1.1d). While the lattice mismatch between Gr and h-BN is only  $\sim 1.5\%$ , h-BN has a wide band gap of  $\sim 6\text{eV}$  [93–96].

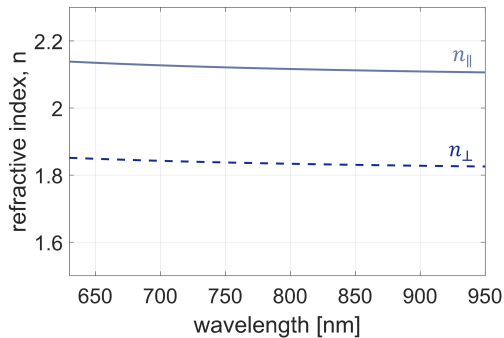


**Figure 1.2:** In-plane ( $n_{\parallel}$ ) and out-of-plane ( $n_{\perp}$ ) refractive index of h-BN, according to Ref. [93].

The most common application of h-BN is its usage as encapsulating layer: active 2D materials can be sandwiched between two h-BN slabs. First, the atomic flatness of h-BN makes it a perfect substrate material for active monolayer devices. For instance, it has been shown that Gr monolayers conform to the rough surface of Si/SiO<sub>2</sub> chips [97]. Using instead h-BN as a substrate can lead to flat monolayer devices, which can show for example improved mobilities and carrier homogeneities in Gr electronics [98]. Second, h-BN is used as protection layer on top, because it is free of dangling bonds and is resistant to oxidation in air (up to 850°) [82]. This can especially protect active 2D materials that are unstable in ambient conditions (like black phosphorous and MoTe<sub>2</sub>) [99, 100]. But also for materials that are generally stable in ambient conditions, encapsulation can help to increase device lifetime and performance (e.g. emission linewidth narrowing of encapsulated monolayer TMDs) [101, 102].

Furthermore, high-quality h-BN flakes have a high breakdown voltage, which makes them particularly suitable as tunnel barriers [103, 104]. The variability of choosing the number of layers enables precise control over the thickness of the atomically smooth barrier. Light emission from h-BN tunneling devices has been demonstrated and enabled novel architectures for light-emitting devices [42, 105, 106].



Lastly, we discuss the optical properties of h-BN. Figure 1.2 shows the refractive index of h-BN,  $n$ , as a function of wavelength [93]. h-BN is a birefringent material with an in-plane refractive index  $n_{\parallel}$  that is slightly higher than the out-of-plane refractive index  $n_{\perp}$ . The extinction coefficient of h-BN for a photon energy of 1 eV was estimated to be  $\kappa_{\parallel} = 0.000048$  and  $\kappa_{\perp} = 0.000043$  [107]. For the visible to near IR range, it was concluded from measurements that the extinction coefficient for thin films is negligible (thicknesses of 150–500 nm) [93]. The associated low absorption makes h-BN also suitable for the encapsulation of optoelectronic components. It has been shown that h-BN hosts quantum emitters [108], that have for example been monolithically integrated inside photonic waveguides, patterned into the h-BN itself [71]. Furthermore, h-BN can be used to fabricate more complex passive photonic structures (thicknesses in the range of several 100 nm) [68–70, 94] and for the co-integration of optical emitters [65, 67, 71]. In chapter 2, h-BN photonics are discussed in more detail, as this is of great importance for this thesis. In general, in this work, we do not only take advantage of h-BN for fabricating photonic structures but we also encapsulate active devices inside h-BN and use h-BN as a tunneling barrier in light emitting devices (chapter 5).

### 1.3 Transition metal dichalcogenides (TMDs)

Among the family of 2D materials, TMDs take over a major role for optoelectronic devices, because they can exhibit semiconducting properties. TMDs have the form  $\text{MX}_2$ , whereby 'M' is a transition metal atom, like Mo, W, etc. and 'X' is a chalcogenide atom such as S, Se or Te. In their monolayer form, TMDs consist of 3 atomic planes, namely a layer of 'M' atoms is sandwiched between two layers of 'X' atoms (X-M-X, see Fig. 1.1b). Therefore, the thickness of an individual monolayer exceeds the thickness of Gr and h-BN monolayers. [109]

In this thesis we focus on three TMDs:  $\text{MoS}_2$ ,  $\text{MoSe}_2$  and  $\text{WSe}_2$ . All of these are used in their 2H crystal structure, in which they are stable under ambient conditions and exhibit semiconducting properties [109]. Most

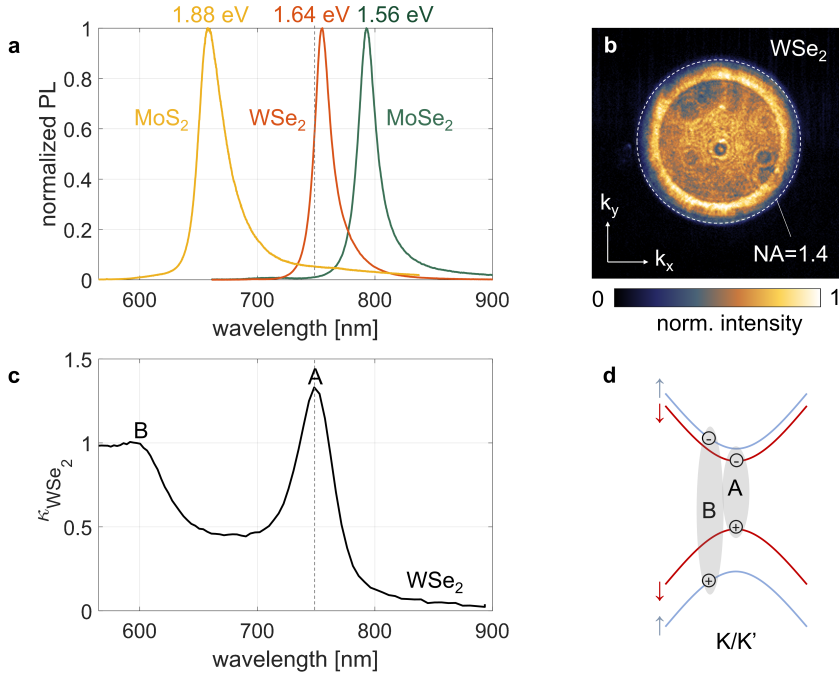


**Figure 1.3:** (a) PL spectra from monolayer MoS<sub>2</sub>, WSe<sub>2</sub> and MoSe<sub>2</sub>. For all measurements the monolayers are encapsulated by h-BN. MoS<sub>2</sub> is excited with a 532 nm continuous wave (cw) laser, whereas WSe<sub>2</sub> and MoSe<sub>2</sub> are excited with a 633 nm cw laser. (b) Normalized Fourier space image of the PL emission from a monolayer WSe<sub>2</sub>, adapted from Ref. [110]. (c) Extinction coefficient of a monolayer WSe<sub>2</sub>, from Ref. [111]. (d) Schematic to indicate the charge carrier origins for the bright A-exciton and the energetically higher B-exciton transition of a monolayer TMD.

importantly these materials exhibit an interesting transformation: when being thinned down from bulk to monolayer their band gap changes from indirect to direct (at K/K'-point), leading to an increased PL in monolayer form [46, 47].

The emission from monolayer TMDs is dominated by strongly bound electron-hole pairs, so-called excitons. In contrast to III-V semiconductors, these excitons have a much higher binding energy in the range of several 100 meV and are therefore observable at room temperature [109, 112–114]. The reason for this is the weak dielectric screening in 2D layers which gives

rise to enhanced Coulomb interactions [112, 113].

The PL emission at room temperature for monolayer MoS<sub>2</sub>, MoSe<sub>2</sub> and WSe<sub>2</sub> shown in Fig. 1.3a, can be mainly attributed to neutral A-excitons. As shown in Fig. 1.3d, in TMDs a strong spin-orbit coupling leads to a large spin-orbit splitting in the valence band (the splitting in the conduction band is comparably small) [109, 113, 115]. As indicated, A-excitons are spin-conserving direct transitions with the smallest energy. Whereas B-excitons are spin-conserving direct transitions with energies several hundreds of meV higher than the A-exciton. In addition to A-excitons, a small fraction of the PL emission can be assigned to trions, excitons that are bound to another free charge carrier. Trions have a slightly lower emission energy and their contribution increases with the doping level of the monolayer [116, 117]. Throughout this thesis whenever we mention excitons and exciton emission, we refer to A-excitons; trions and B-excitons are otherwise specified.

The exciton emission from monolayer MoS<sub>2</sub>, MoSe<sub>2</sub> and WSe<sub>2</sub> is mainly attributed to in-plane (parallel to the monolayer) oriented incoherently radiating dipole emitters [118, 119]. Figure 1.3b shows the Fourier Space image of the PL from a monolayer WSe<sub>2</sub> encapsulated in h-BN at room temperature (oil immersion objective with NA=1.4\*). The resulting emission pattern agrees with the pattern from in-plane oriented emitters encapsulated inside h-BN layers.

The absorption characteristics of monolayer TMDs are also governed by the exciton transitions. For a single monolayer, the absorbance is in the range of 10 % [46, 120, 121]. The absorbance is strongly wavelength-dependent, with a resonant absorption peak close to the resonance wavelength of the exciton emission. For a visualization, in Fig. 1.3c the imaginary part of the refractive index of a monolayer WSe<sub>2</sub>,  $\kappa_{\text{WSe}_2}$ , is plotted [111].

---

\*By imaging the back focal plane, the angular distribution (radiation pattern) of the emission can be characterized. Details on the measurement setup and the Fourier space imaging can be found in the Appendix A.1.2.

## 1.4 Heterobilayer (HBL) of two dissimilar monolayer TMDs

\*

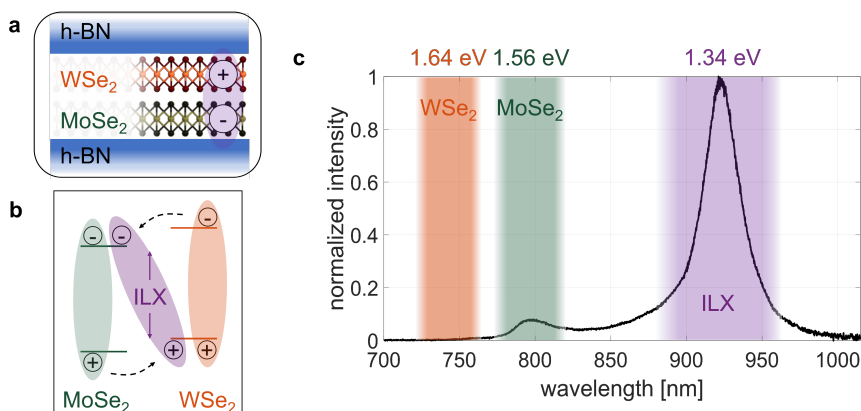


**Figure 1.4:** (a) Illustration of an interlayer exciton (ILX) that is formed in a WSe<sub>2</sub>/MoSe<sub>2</sub> HBL that is encapsulated by h-BN. (b) Band structure of the WSe<sub>2</sub>/MoSe<sub>2</sub> HBL, indicating the type-II band alignment, which gives rise to the formation of interlayer excitons. (c) PL spectrum of the HBL upon excitation with a 633 nm cw laser. At the overlap, the interlayer exciton emission peak is very strong, while the intralayer exciton emission of the two individual monolayers is quenched.

Two dissimilar monolayer TMDs can be combined in one heterostructure to form a HBL. The strong Coulomb interaction can thereby lead to the formation of interlayer excitons, with the electron and hole each spatially separated in an individual layer, as shown in Fig. 1.4a. Due to the spatial separation, interlayer excitons have a long lifetime [55, 56, 62, 122] and an out-of-plane oriented static electric dipole [57, 123]. By applying out-of-plane fields, interlayer exciton diffusion can be manipulated [123] and the emission energy can be tuned [57]. In this section and in chapter 4 we refer to the excitons from the individual monolayers as intralayer excitons to highlight their difference

\*This section is in part adapted from the article R. Khelifa, P. Back, N. Flöry, S. Nashashibi, K. Malchow, T. Taniguchi, K. Watanabe, and L. Novotny. *Coupling Interlayer Excitons to Whispering Gallery Modes in van der Waals Heterostructures*, *Nano Letters*, **20**, 6155-6161 (2020). Adapted with permission from [73]. Copyright 2020 American Chemical Society.

compared to interlayer excitons that are formed among the two adjacent monolayers.

The energy of the interlayer exciton can be explained by the type-II band alignment of the two monolayers [55, 62, 124], shown for MoSe<sub>2</sub> and WSe<sub>2</sub> in Fig. 1.4b. The twist angle between the two dissimilar monolayers translates into a rotation in momentum space. This means that for two rotationally aligned monolayers the interlayer exciton exhibits a direct band gap character (at K/K' point) [125].

Upon laser excitation, the absorption of a photon in a monolayer is followed by a charge transfer to the energetically favorable band of the neighboring monolayer, leading to a spatial separation of electron and hole (see Fig. 1.4b). This results in a pronounced interlayer exciton peak, which is observable in the PL spectrum of a MoSe<sub>2</sub>/WSe<sub>2</sub> HBL shown in Fig. 1.4c. The charge-transfer to another monolayer is a fast process in the order of 20 – 50 fs and competes with the radiative recombination in the individual monolayers [56]. As a result, a strong decrease of the intralayer exciton emissions can be observed. The strong interlayer peak in combination with the quenching of intralayer exciton emission in Fig. 1.4c consequently verifies the good electrical coupling and the near perfect rotational alignment of the two layers. By using back focal plane imaging, experimentally the interlayer exciton emission has been attributed mainly to in-plane oriented dipole emitters [126].

The HBL exhibits a low intrinsic absorption at energies of the interlayer exciton [127, 128]. This is due to the low oscillator strength of the interlayer transition, resulting from the spatial separation of the charge carriers [127, 129]. The oscillator strength of the interlayer exciton in MoSe<sub>2</sub>/WSe<sub>2</sub> has been experimentally determined to be two to three orders of magnitude lower than that of the intralayer exciton [128, 129].

## 1.5 TMD based LEDs

The new degree of freedom brought by lattice-independent stacking of 2D materials enables the development of novel device architectures for electrically driven light emission. In 2015, Withers et al. demonstrated light emission from monolayer TMDs by quantum wells engineering with atomic precision [37]. The device architecture is schematically shown in Figs. 1.5a and b. The LEDs are composed of a monolayer TMD embedded between two thin h-BN tunneling barriers (several layers each) and two Gr monolayers as electrodes [37, 38, 44]. The two Gr electrodes enable the vertical charge carrier injection via tunneling through the thin h-BN layers (see Fig. 1.5c). The formation of excitons within the TMD and their radiative recombination results in light emission from the overlap area [37, 38]. For  $\text{WSe}_2$ , a room temperature external quantum efficiency of 5% has been shown [38]. To further enhance the emission, multiple monolayer tunneling LEDs were stacked on top of each other and external quantum efficiencies of 8.4% were achieved [37].

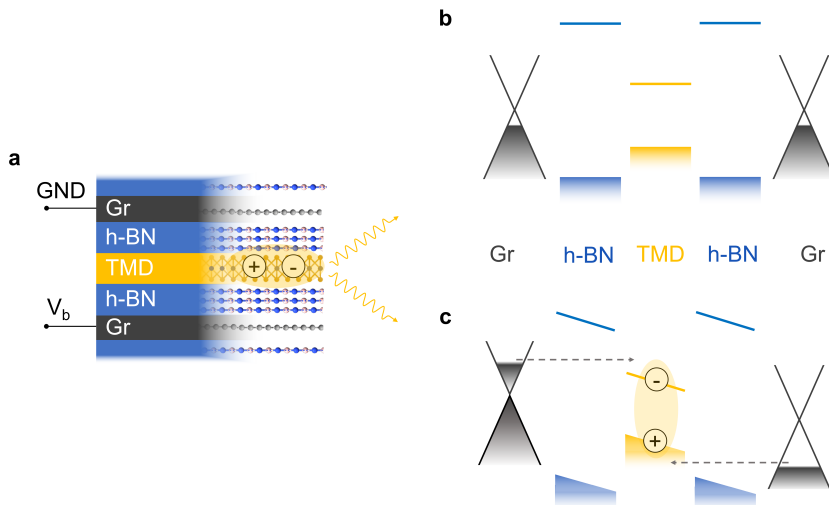


**Figure 1.5:** (a) Schematic illustration of the Gr – h-BN – TMD – h-BN – Gr LED design. Band alignment at (b) zero bias and (c) for an applied bias, allowing charge carrier injection from both Gr electrodes.

At first, light emission from such a tunneling LED was expected to only occur for voltages high enough to enable charge carrier injection from the Gr into the conduction and valence band of the monolayer TMD (see Fig. 1.5c) [37]. However, electrically driven emission has already been reported for voltages below the electronic band gap [38, 130]. Binder et al. attributed this to direct tunneling of carriers into excitonic states in the monolayer TMD [130]. It has been shown that for several different light-emitting diodes from a broad range of material classes other than 2D materials (perovskite, III-V semiconductors, organic, ...) light emission for biases below the optical band gap can be detected [131]. This was explained by the radiative recombination of charge carriers close to the band edge, where the distribution is defined by the tail of the Fermi-Dirac function [131]. Recently, in our group, other explanations have developed. These rely on the tunneling of charge carriers from one electrode to the other. Thereby an exciton can be formed by direct energy transfer [132, 133].

In chapter 5, we focus on the integration of an exciton LED based on WSe<sub>2</sub> in the tunneling design, shown in Fig. 1.5. Nevertheless, it is noteworthy that electrically driven TMD-based exciton emission was also observed for other device architectures of vdW heterostructures [35, 36, 39–41]. Furthermore, light-emitting devices with HBLs and electrically driven interlayer exciton emission have been realized [57, 129, 134]. This fast progress highlights the diverse potential for band structure engineering of LEDs with monolayers and HBLs of TMDs.





# 2

---

## On-chip h-BN photonic structures

The second building block to design and develop integrated on-chip photonics based on 2D materials are passive photonic structures. One basic, but most important component of PICs are optical waveguides. They tie the circuit together by enabling optical interconnection between different integrated devices. The first section of this chapter introduces the fundamentals of waveguiding and aims to establish an understanding of the properties of confined waveguide modes. We then further expand the discussion on a second photonic structure, namely disk resonators and first elaborate on their fundamental properties and typical figures of merit.

Among the 2D material family, h-BN has evolved as a promising candidate for the fabrication of passive photonic structures. In the second part of this chapter, we introduce h-BN-based waveguides and disk resonators. To deepen the understanding, we discuss first design requirements and numerical simulations.

Lastly, we address how other 2D materials and heterostructures can be integrated with h-BN photonics. We conclude this chapter by elaborating on the coupling of emitters to photonic structures.

## 2.1 Fundamentals

### 2.1.1 Waveguide properties

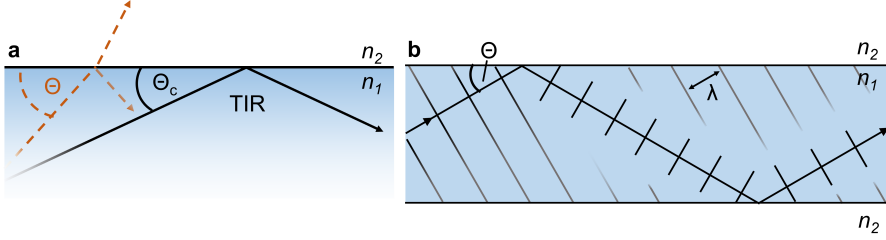


**Figure 2.1:** (a) TIR at an interface, whereby  $n_1 > n_2$ . Oriented on Ref. [135].  
 (b) Plane-wave inside a waveguide: constructive interference with itself after two reflections at the interface. Oriented on Ref. [136].

By considering a ray optical approach, in the following, we want to establish an intuitive understanding of waveguiding [135–138].\* More precisely, each ray is considered to be a plane wave. Let us have a look at a material with the refractive index  $n_1$ , that is surrounded by a medium with the refractive index  $n_2$ , for which  $n_1 > n_2$  holds. Waveguiding inside the material with the higher refractive index occurs if two requirements are fulfilled: 1) total internal reflection (TIR) at the interface and 2) constructive interference with itself after reflection at the interface [135, 136]. For TIR the incident light is reflected back from the  $n_1/n_2$  interface, instead of being refracted into the outer medium. As shown in Fig. 2.1a, this occurs if the incident angle  $\Theta$  is smaller than the critical angle  $\Theta_C$  [135, 136], which is defined as

$$\Theta_C = \cos^{-1} \left( \frac{n_2}{n_1} \right). \quad (2.1)$$

As a second requirement, the reflected light has to constructively interfere with itself. In Fig. 2.1b this so-called self-consistency condition is met: the plane wave is in phase with itself after two reflections [136]. This leads to a discrete set of confined optical waveguide modes, with corresponding mode angles.

\*The ray optical approach offers a less complete picture, a more elaborated description can be found in [135, 136].

Here a mode describes a spatial distribution of the electric field that propagates inside the waveguide while remaining constant in shape [135–138].

In this thesis, we focus on h-BN ridge waveguides ( $n_{\text{h-BN}}$ ) on top of a glass substrate ( $n_{\text{glass}}$ ) and surrounded by air ( $n_{\text{air}}$ ) (see outlines in Fig. 2.2). Due to the complex 2D geometry, numerical methods are commonly used to find solutions that satisfy the Helmholtz equation [137]. Thus, to determine these waveguide modes, we perform finite-difference time-domain (FDTD) simulations (Lumerical Inc.). Depending on the geometrical properties of the waveguide, the refractive indices, and the wavelength, a specific number of modes can be supported. Hence, depending on the desired application, the dimensions of the waveguide can be adjusted such that, for example, only the fundamental mode is supported for the selected optical wavelength.

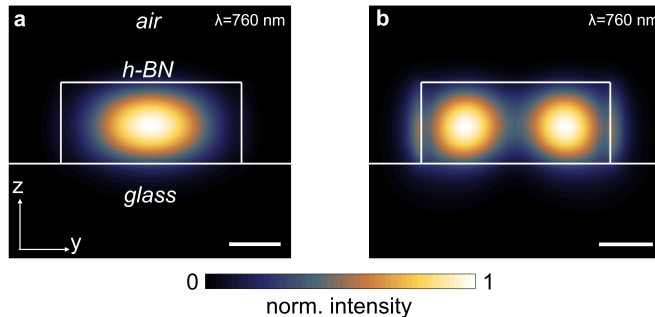


**Figure 2.2:** Mode profiles of an h-BN waveguide on top of a glass substrate. (a) Fundamental TE mode and (b) first order TE mode for a wavelength of 760 nm. The scale bar is 200 nm.

Figure 2.2a displays the simulated field intensity of the fundamental transverse electric (TE) mode (wavelength of 760 nm) for a waveguide with the indicated dimensions. The mode is confined inside the dielectric, with the highest field intensity close to the vertical center. The asymmetry of the surrounding material on top and below leads to a shift of the field maximum towards the substrate (with the higher refractive index).

In addition to the fundamental TE mode, at a wavelength of 760 nm the given waveguide also supports a fundamental transverse magnetic (TM) mode and a 1st order TE mode (see Fig. 2.2b). TE (TM) modes have no electric (magnetic) field component in the propagation direction\* [136–138]. For the TE modes, the characteristic component of the electric field is polarized along the y-direction [136, 137, 139].

Each mode is associated with a certain effective refractive index,  $n_{\text{eff}}$ . A less confined mode experiences more of the surrounding medium with lower refractive index and consequently has a lower effective refractive index. Here, the material and the waveguide properties play a role: the refractive index and the conditions for waveguiding both change with wavelength. The effective refractive index can then decrease further to a cutoff at which, for a given wavelength,  $n_{\text{eff}}$  equals  $n_{\text{glass}}$  and no more modes are supported [136, 138].

### 2.1.2 Whispering gallery modes (WGMs) in disk resonators

In a dielectric disk, repeated TIR at the outer interface can lead to a guided mode (cf. Fig. 2.3a). For wavelengths that can fit precisely integer times into the optical path length of one round trip, constructive interference leads to a resonance. So-called WGMs have first been described for acoustic waves by Rayleigh [140]. In the field of photonics, spherical cavities have gained much attraction due to their high quality (Q)-factors associated with the WGM resonances. Typical applications for disk and ring resonators are as spectral filters and laser cavities, for optical communication and sensing [141, 142].

Different WGMs can be confined inside the disk. The number of maxima in radial direction defines the radial mode number, and the azimuthal mode number describes the number of lobes in azimuthal direction [143]. Figure 2.3b shows in a cross-sectional view the simulated electric field distribution (absolute value) near the rim of a disk resonator (COMSOL). For a wavelength of 660 nm

---

\*This is only valid in 1D. Modes in 2D also have a small component in the direction of propagation. More precisely they are called quasi-TE and quasi-TM modes. For simplicity, throughout this thesis we refer to them as TE (TM) modes.

and a disk radius of  $3\ \mu\text{m}$  the most confined mode is mainly in-plane polarized and has one maximum in radial direction. The spectral spacing between the modes is called free spectral range (FSR) [143].

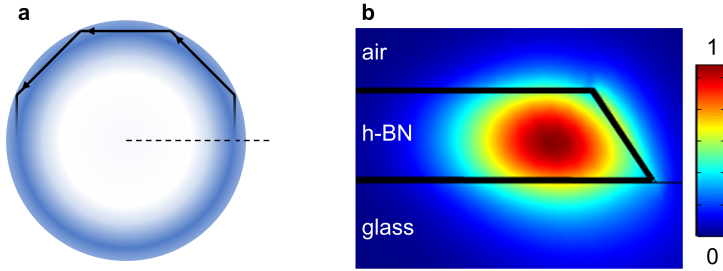


**Figure 2.3:** (a) Schematic illustration of the disk resonator. TIR is observed at the outer sidewall. (b) Simulated electric field distribution (absolute value) near the rim of a disk resonator (cross-sectional view, indicated by the dashed line in (a)). Adapted with permission from [73]. © 2020 American Chemical Society.

Due to the curvature of the disk, the resonant modes are leaky, and even in perfect conditions energy is lost due to radiation [143, 144]. This loss is often referred to as whispering-gallery, tunnel, or bending loss [145]. To quantify losses the Q-factor is introduced. It describes the optical cycles inside the cavity before the confined energy is lost. The Q-factor can be written as

$$Q = \frac{\omega_0}{\Delta\omega}, \quad (2.2)$$

with the center frequency of the resonant mode  $\omega_0$  and half the width of the resonance  $\Delta\omega$  [143, 144].

Commonly, however, the measured Q-factor in fabricated devices is governed by other losses. The total Q-factor can then be further extended [145–147], e.g. as:

$$\frac{1}{Q_{\text{tot}}} = \frac{1}{Q_{\text{bend}}} + \frac{1}{Q_{\text{scatt}}} + \frac{1}{Q_{\text{surf}}} + \frac{1}{Q_{\text{abs}}} + \frac{1}{Q_{\text{ext}}}. \quad (2.3)$$

In addition to the bending losses  $Q_{\text{bend}}$ ,  $Q_{\text{scatt}}$  accounts for photons that are

scattered due to imperfections such as the sidewall roughness of the disk.  $Q_{\text{surf}}$  is related to losses due to contamination at the surface.  $Q_{\text{abs}}$  accounts for absorption losses of the material and can be defined as

$$Q_{\text{abs}} = \frac{2\pi n_{\text{eff}}}{\alpha \lambda}, \quad (2.4)$$

where  $\alpha$  is the mean absorption coefficient, and  $\lambda$  and  $n_{\text{eff}}$  are the wavelength and effective refractive index of the mode [145, 147].

The coupling to the resonator with a waveguide enables the connection of the cavity mode to the rest of a photonic circuit. Commonly, the coupling is achieved by placing a waveguide nearby to couple via the evanescent fields. Depending on the distance between waveguide and disk the coupling can be optimized [148]. For critical coupling conditions, on resonance 100% of the light in the waveguide is transmitted to the resonator [149]. Depending on the coupling conditions, the total Q-factor is influenced, which can be accounted for by  $Q_{\text{ext}}$  [150].

## 2.2 h-BN photonics

As introduced in section 1.2, h-BN is a wide-band gap insulator. Among 2D materials, it has evolved as a good candidate for the fabrication of passive photonic structures. Within our spectral range of interest ( $\sim 660 - 930\text{nm}$ ), h-BN is nearly non-absorbing [93, 107], and the in-plane and out-of-plane refractive indices can be approximated to  $n_{\parallel} \approx 2.1$  and  $n_{\perp} \approx 1.8$  (cf. Fig. 1.2) [93].

Waveguides, ring and disk resonators, as well as photonic crystal waveguides and cavities, have been demonstrated throughout the last years [68, 69, 71, 72]. Q-factors up to 5000 have been achieved for photonic crystal cavities [72]. Different types of fabrication techniques, like reactive ion etching (RIE) [151] and electron beam-induced etching (EBIE) [69], have been introduced for the fabrication of these devices. Recently, by using thermal scanning-probe lithography and RIE, freeform photonic landscapes have been patterned into

h-BN flakes [70].

Also for the fabrication of the photonic structures for the devices presented in this thesis, h-BN is a good candidate. Therefore, before discussing integrated devices, in this section, we first investigate the properties of passive h-BN photonic structures without integrated TMDs.

### 2.2.1 h-BN-based waveguides

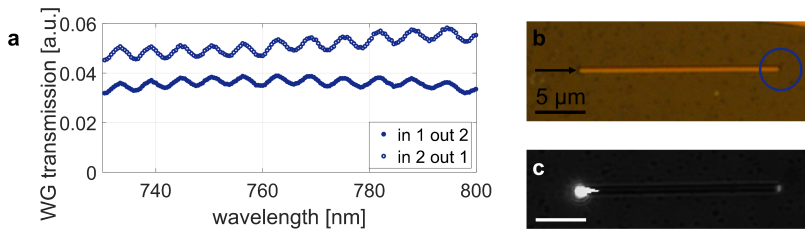


**Figure 2.4:** (a) Transmission curve of a bare h-BN waveguide. A broadband laser is coupled into one waveguide end and the transmitted light is detected at the other end (as indicated in (b)). Each line corresponds to excitation and detection at one waveguide end. (b) Optical microscope image of the h-BN waveguide. (c) Real space image while focussing the laser on the left waveguide end. Light can be detected at the other waveguide facet. The scale bar is 5  $\mu\text{m}$ .

### Experiment

As a first experimental photonic structure, we introduce h-BN-based waveguides. These can be fabricated by patterning mechanically exfoliated h-BN flakes by means of electron beam lithography (EBL) and RIE.\* Figure 2.4b shows the optical microscope image of an h-BN waveguide with a thickness of  $\sim 240$  nm and a base width of  $\sim 550$  nm. From scanning electron microscope (SEM) imaging on a reference device, a sidewall angle of  $\sim 55^\circ$  was determined. This is defined by the etching process, used for patterning of the device.

As depicted in the real space image in Fig 2.4c, when focusing a broadband

\*The fabrication procedure is discussed in more detail in chapter 3 and in the Appendix A.1.1.2.

laser source on one end facet of the waveguide, light can be detected at the other waveguide end. The oil immersion objective (NA=1.4) that we use can capture at high angles the out-coupled light that is refracted into the glass substrate.\* The light measured at the end of the waveguide was then normalized to the laser spectrum (measured reflection). The transmission spectrum in the given spectral range is plotted in Fig. 2.4a. Each curve corresponds to the excitation/detection at one waveguide side. We attribute the observed oscillations to the abrupt ends of the waveguide structure, which introduce cavity resonances. It is important to mention, that this measurement technique is limiting because the spectral in-coupling characteristics are not known. This is because the light is coupled into the waveguide without grating couplers, but due to scattering at the edges when the laser is focused on the end facet. Nevertheless, the measurements show the successful implementation of h-BN waveguides and their transmission in the given wavelength range.

### Simulations

The introduced waveguide is designed such, that for a wavelength of 760 nm only the fundamental TE mode is supported. For this matter, FDTD simulations (Lumerical Inc.), were performed. The effective refractive index  $n_{\text{eff}}$  for the fundamental TE and TM modes, as well as for the 1st order TE modes are plotted in Fig. 2.5a as a function of the base width of the waveguide. The blue area indicates the refractive index of the glass substrate ( $n_{\text{glass}} = 1.515$ ). The waveguide thickness of 240 nm and the sidewall angle of  $55^\circ$  were adapted to the flake thickness and the etching angle, respectively. For a base width of 550 nm (as in the earlier discussed waveguide) the criterion of single mode propagation at the target wavelength is fulfilled. The simulated field intensity for the corresponding fundamental TE mode is shown in Fig. 2.5b.

---

\*The out-coupled light is collected with the same objective as used for the focusing of the input laser (see details on the experimental setup in the Appendix A.1.2).



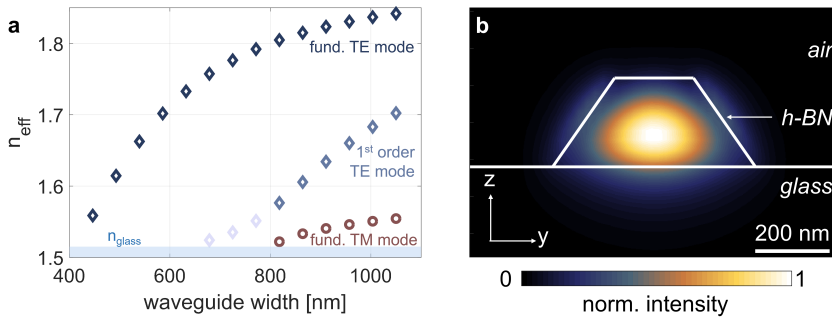


**Figure 2.5:** (a) Effective refractive index  $n_{\text{eff}}$  as a function of the waveguide base width for a wavelength of 760 nm. The fundamental TE mode is plotted in dark blue (diamonds); the first order TE mode, and the fundamental TM mode are plotted in light blue (diamonds) and red (circles), respectively. For the light blue diamonds following the trend of the 1st order TE modes, the modes are not anymore mainly TE polarized but hybrid. The blue area indicates the region below the refractive index of the glass substrates for which no more confined modes exist. (b) Mode profile of the fundamental TE mode (760 nm) in an h-BN waveguide on a glass substrate, with the dimensions as experimentally implemented. Adapted from Ref. [110].

### 2.2.2 h-BN waveguide-coupled disk resonators

\*

#### Experiments

Next, we discuss h-BN waveguide-coupled disk resonators as shown in the schematic in Fig. 2.6b. To characterize such devices, one waveguide end is illuminated with a tightly focused, broadband excitation source. In Fig. 2.6a, the transmission measurement of an h-BN waveguide-coupled disk resonator, is shown. The disk resonator has a radius of 3  $\mu\text{m}$  and a height of  $\sim 220$  nm, the designed waveguide top width is 200 nm.

To characterize the device, Lorentzian lineshapes were fitted to the measured resonances and Q-factors of up to  $\sim 1000$  were determined (blue diamonds

\*This subsection is in part adapted from the article R. Khelifa, P. Back, N. Flöry, S. Nashashibi, K. Malchow, T. Taniguchi, K. Watanabe, and L. Novotny. *Coupling Interlayer Excitons to Whispering Gallery Modes in van der Waals Heterostructures*, *Nano Letters*, **20**, 6155-6161 (2020). Adapted with permission from [73]. Copyright 2020 American Chemical Society.

in Fig. 2.6d). Depending on the disk thickness and radius the Q-factors and the spectral resonance positions change: within a certain wavelength range (600 – 700nm), devices with Q-factors varying from 200 – 1000 were fabricated. Consequently, to develop an understanding on the most suitable geometries, we used simulations as a guide to optimize our devices. This way the best thicknesses and disk radii were determined depending on the desired wavelength range.

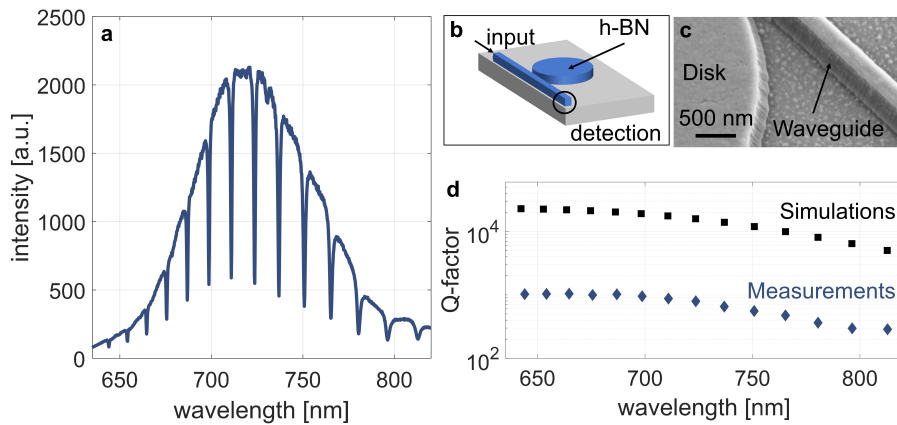


**Figure 2.6:** (a) Transmission spectrum of an h-BN waveguide-coupled disk resonator without integrated TMD. The dips correspond to the resonances of the WGMs and the envelope function is determined by the spectrum of the broadband laser source and the transmission characteristics of the setup and waveguide. (b) Sketch of the h-BN waveguide-coupled disk resonator. (c) SEM image of a representative h-BN disk resonator directly after etching (metal mask is still on top). (d) Q-factors determined from the measurements in (a) (blue diamonds), and from simulations (black squares).

## Simulations

2D simulations of the disk resonator without coupled waveguide were performed (COMSOL). The h-BN disk was simulated on top of a glass substrate ( $n = 1.52$ ) and surrounded by air ( $n = 1$ ). Figure 2.6d shows the simulated Q factors (black squares) for an h-BN disk with a radius of  $3\ \mu\text{m}$  and a height of  $\sim 220\ \text{nm}$  (same as in experiment). The FSR and resonance wavelengths of the simulated resonances agree with the measured resonances

(blue triangles in Fig. 2.6d). However, the simulated Q-factors are higher than the ones determined from measurements. This is not surprising and the main reason for this is attributed to fabrication imperfections, like for example the sidewall roughness, which is evident in the SEM image of a representative device in Fig. 2.6c.\*

A decrease in Q-factor for increasing wavelengths is observable in measurements and in simulations. This can be explained by the fact, that for longer wavelengths the radiative losses due to the curvature of the disk increase, leading to a decrease of the Q-factor.

The simulations do not include the adjacent waveguide. As discussed in subsection 2.1.2, the waveguide and its distance to the disk can indeed have an influence on the device properties. Further design optimizations could be achieved, but this is above the scope of this work.

### **2.3 Integration of TMD-based emitters with h-BN photonic structures**

The use of h-BN as a material for passive photonic structures also provides an additional advantage for the integration of other 2D materials as active devices. The lattice-independent stacking of vdW materials opens up a new degree of freedom because it enables the integration of the active layers inside the dielectric by sandwiching it between thick layers of h-BN [65, 67]. These h-BN layers then determine the vertical height of the photonic structure. This approach stands in contrast to conventional fabrication methods, in which lattice matching and other material requirements restrict growth methods and integration. To co-integrate vdW devices with Si- or III-V semiconductor-based PICs, commonly the vdW heterostructures are placed on top of prefabricated photonic structures [19, 24, 25, 29, 63, 64, 152]. In this way, the light emitted by an LED [19] or by optically excited TMDs [59, 153] was evanescently coupled

---

\*Note that these devices were etched with a metal etch mask, which can be seen on top of the h-BN. The main introduction to the fabrication process of these devices will be given in chapter 3.

to pre-patterned waveguides and waveguide-coupled ring resonators. In this section, we elaborate on the advantage of embedding TMD-based emitters inside h-BN photonic structures and compare it with integration on top.

### 2.3.1 Integration of monolayer TMDs as active materials

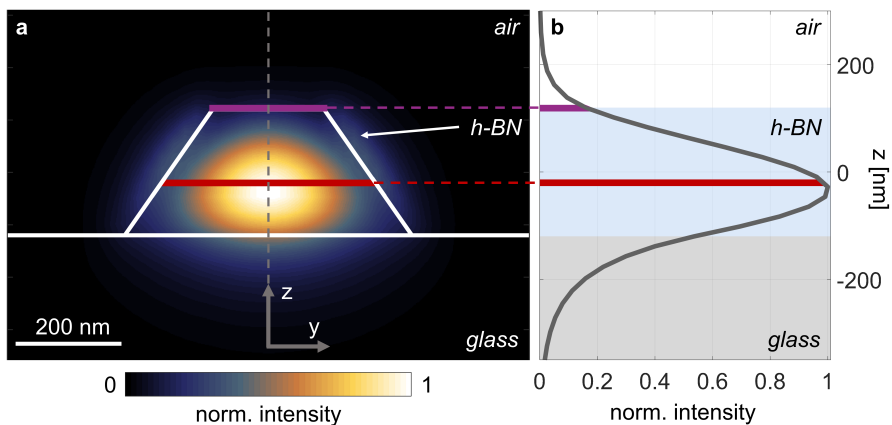


**Figure 2.7:** (a) Intensity distribution of the fundamental TE mode (760 nm) in an h-BN waveguide placed on top of a glass substrate. (b) Intensity profile along the  $z$ -direction (gray line in (a)), whereby  $z = 0$  nm, is the vertical center of the waveguide. The peak maximum is shifted towards the glass substrate, due to its higher refractive index. The purple and the red lines, indicate possible positions of integrated monolayers and illustrate the corresponding field intensity at their positions. (a) and (b) Adapted from Ref. [110].

The atomically thin nature of monolayer TMDs intrinsically restricts the strength of the light-matter interaction [49, 154]. This reinforces the need to enhance their performance by properly engineering the photonic environment. In the following, we would like to illustrate this on the example of waveguide-integrated structures. In subsections 2.1.1 and 2.2.1, we have seen that waveguiding enforces light fields to propagate as confined modes inside a dielectric slab. As shown in Figs. 2.7a and b the intensity of the mode attains its maximum near the vertical center of the waveguide. By placing a monolayer

TMD at the specified location inside the dielectric (red line in Figs. 2.7a, b)\*, the overlap between waveguide mode and active layer can be enhanced. For comparison, the purple line in Figs. 2.7a and b indicate the field intensity when positioning the monolayer on top, where the devices are placed in conventional coupling schemes. Note that the field intensities in Fig. 2.7 are simulated for a bare h-BN waveguide placed on top of a glass substrate. The field intensity at the indicated position inside (red line) is  $\sim 6$  times higher than the field intensity on top (purple line). This in turn leads to an increase of the field that is confined inside the monolayer. Consequently, the light-matter interaction can be optimized, which is for example favorable for improved absorption in photodetectors [89]. While in this section we have motivated the sandwiched integration for waveguides, the same is applicable for WGM resonators.

### 2.3.2 Coupling of emitters to photonic structures

Lastly, we want to introduce characteristic properties when coupling emitters to photonic structures. In this work, we integrate electrically driven light sources inside h-BN waveguides. For this reason, we discuss at this point a figure of merit to characterize waveguide-integrated emitters, namely the coupling efficiency. Furthermore, we integrate optically driven emitters inside h-BN disk resonators. Therefore, we discuss the influence that the surrounding environment has on the emission characteristics of the embedded emitter and introduce the Purcell factor.

#### Coupling efficiency to a waveguide

When integrating a light source with a waveguide one key figure of merit is the coupling efficiency  $\beta$ , which describes how much of the emitted light is coupled to the waveguide.  $\beta$  can be determined according to

$$\beta = \frac{I_{\text{WG}}}{I_{\text{WG}} + I_{\text{free}}}, \quad (2.5)$$

---

\*The dimensions are the same as for the experimentally demonstrated waveguide, discussed in subsection 2.2.1 and in chapter 5. Furthermore, the vertical position of the integrated monolayer is adapted to the position of the device presented in chapter 5, which is close to the field maximum.

where  $I_{\text{WG}}$  and  $I_{\text{free}}$  are the emitted intensity into the waveguide and into free-space in presence of the waveguide, respectively [155–157]. For efficient on-chip integration of an LED with a waveguide, it is favorable to engineer the structure such that a large fraction of the light is emitted into the desired waveguide mode. One way to increase the coupling efficiency is to optimize the mode overlap between the emitter and the guided light field. This can be achieved by following our approach and placing the emitter inside the light confining dielectric.

Another characteristic that influences the coupling efficiency is the dipole orientation of the emitter with respect to the polarization of the confined light field. Here, we focus on the coupling of TMD-based exciton emission. As discussed in section 1.3, the exciton emission from monolayer TMDs is governed by in-plane oriented dipoles. These emitters can consequently couple most efficiently to modes polarized along the in-plane direction. For the integration, the waveguide design should therefore be optimized to support fundamental TE modes.

Numerical simulations help to evaluate how much emission of a dipole source integrated inside a bare h-BN waveguide (dimensions as shown in Fig. 2.7) is coupled to the fundamental TE mode. The dipole (emission at 760 nm) is oriented along the y-axis and is placed in the lateral center of the waveguide, while the z-position is varied. For an embedded dipole emitter (at the z-location indicated in red in Fig. 2.7) the coupling efficiency is  $\sim 5$  times higher compared to placing the emitter on top of the h-BN (at the z-location indicated in purple in Fig. 2.7). The exact improvement in coupling efficiency depends not only on the wavelength but also on the waveguide design, since the width and sidewall angle can also affect the intensity profile of the waveguide mode. In addition, the presence of the waveguide, more precisely the vertical position of the emitter in the waveguide, can modify the emission characteristics of the emitter [158, 159].

### **Purcell factor**

The presence of the surrounding photonic environment directly affects the

emission characteristics of the emitter [144, 160]. This is due to the change in the local density of optical states (LDOS). More precisely, the LDOS change the lifetime of the emitter's excited state. This effect was first expressed in 1946 by Purcell [161]. In his analysis he described that the decay rate of an emitter inside a single mode resonator is enhanced by the factor:

$$F_P = \frac{\Gamma_{\text{res}}}{\Gamma_0} = \frac{3 \left( \frac{\lambda_0}{n} \right)^3 Q}{4\pi^2 V_{\text{eff}}}. \quad (2.6)$$

$\Gamma_0$  and  $\Gamma_{\text{res}}$  are the spontaneous decay rates in free-space and inside the resonator, respectively.  $Q$  is the quality factor and  $V_{\text{eff}}$  the mode volume of the cavity.  $\frac{\lambda_0}{n}$  is the emission wavelength of the emitter that the cavity is tuned to. Placing an emitter inside a cavity can therefore lead to an emission enhancement relative to the free-space emission [144, 160, 161].

## 2.4 Conclusion

In this chapter we have introduced the second building block for the development of integrated photonic structures solely based on 2D materials. The fundamentals of waveguides and WGMs in disk resonators were laid out and passive h-BN photonic structures were presented. Most importantly, we have seen that the integration of monolayer TMDs inside the light confining dielectric at high field intensities is advantageous. We have motivated that h-BN is a good candidate as a dielectric to sandwich other 2D materials and vdW heterostructures as emitters inside the confinement layer.





# 3

---

## Integration of monolayer TMDs inside h-BN-based disk resonators

\*

At this point the fundamentals of 2D materials and vdW heterostructures (chapter 1), as well as the basics of integrated h-BN photonics (chapter 2) have been introduced. We have therefore provided the necessary framework to introduce the versatile vdW photonics platform for efficient on-chip integration. As a first device, we present vdW heterostructures patterned into waveguide-coupled disk resonators, as illustrated in Fig. 3.1. We integrate a monolayer TMD at high field intensities inside the h-BN disk to couple the exciton PL to the WGMs of the h-BN disk resonator.

In this chapter, we first introduce the device concept and the fabrication approach. We then present optical measurements of the waveguide-coupled

---

\*This chapter is in parts adapted from the article (mainly the corresponding Supporting Information) R. Khelifa, P. Back, N. Flöry, S. Nashashibi, K. Malchow, T. Taniguchi, K. Watanabe, and L. Novotny. *Coupling Interlayer Excitons to Whispering Gallery Modes in van der Waals Heterostructures*, *Nano Letters*, **20**, 6155-6161 (2020). Adapted with permission from [73]. Copyright 2020 American Chemical Society.

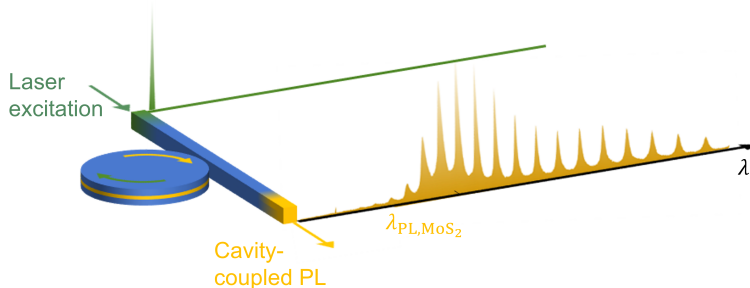


**Figure 3.1:** Illustration of a waveguide-coupled disk resonator with integrated monolayer  $MoS_2$ . The emission from the exciton is coupled to WGMs of the disk resonator and then out-coupled through the same waveguide used for excitation.

disk resonator with integrated monolayer TMD (device 1). Lastly, we compare the results to measurements of a device with a monolayer placed on top of the disk (device 2).

## 3.1 Device concept

The unique feature of this approach is that both, the active material (TMDs) as well as the dielectric (h-BN) are assembled into a single vdW heterostructure and subsequently patterned into the final photonic structure (disk resonator and waveguide). Flakes of h-BN and monolayer  $MoS_2$  were prepared by mechanical exfoliation and assembled into vdW heterostructures using a polymer-based stacking technique [162, 163]. Atomic force microscopy (AFM) was utilized to identify h-BN flakes of the desired thicknesses. Figure 3.2a shows an optical microscope image of such an h-BN –  $MoS_2$  – h-BN heterostructure on a glass substrate.

To fabricate waveguides and disk resonators from the vdW stack, EBL and metal evaporation were used to pattern aluminum (Al) as a hard mask on

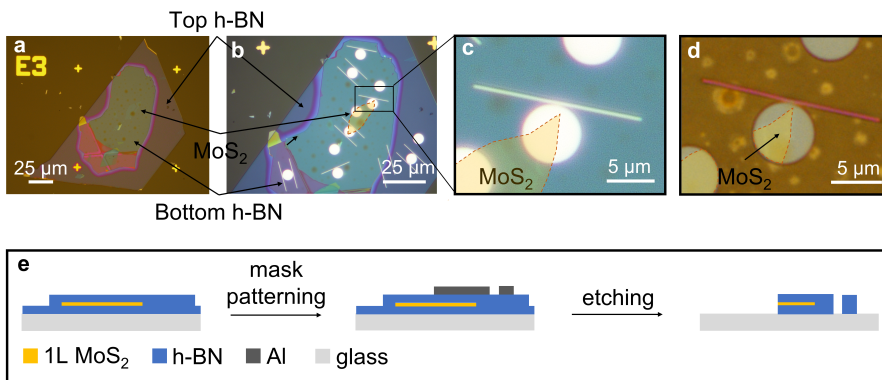


**Figure 3.2:** (a) Optical microscope images of the h-BN – MoS<sub>2</sub> – h-BN heterostructure after stacking. The heterostructure has a total thickness of  $\sim 310$  nm (bottom h-BN:  $\sim 155$  nm and top h-BN:  $\sim 155$  nm). (b,c) EBL and metal evaporation were utilized to structure Al as etch mask. (d) Final devices after patterning (RIE) the vdW heterostructure into a waveguide-coupled disk resonator with a design radius of  $3 \mu\text{m}$ . (e) Schematic of the fabrication procedure, showing cross-sections of the vdW heterostructure after stacking and after subsequent patterning into a waveguide-coupled disk resonator (not to scale).

top of the stack (see Figs. 3.2b and c). Here, a major benefit is that the photonic structure can be aligned precisely according to the position of the monolayer. This stands in contrast to conventional methods of placing a vdW stack onto prefabricated photonic structures [19, 24, 153], for which the alignment is defined by the precision of the stacking process, rather than EBL. Especially, for more complicated active devices, in which the stacking is limiting, this can be beneficial.

The heterostructure is then patterned by stepwise etching with RIE. Fig. 3.2d shows the final device after the removal of the metal mask. A summary of the fabrication procedure is shown in Fig. 3.2e. In addition, a more detailed description, the exact processing parameters, and documentation on the difficulties that might occur during etching can be found in the Appendix A.1.1.

As discussed in section 2.3, the mode overlap of an emitter and the photonic

structure can be improved by placing the active material inside the dielectric. By choosing two h-BN flakes with a thickness of  $\sim 155$  nm, the stacking allows us to sandwich the monolayer at the vertical center of the disk, near regions of high field intensity. The disk is aligned such that the monolayer MoS<sub>2</sub> is positioned inside the disk (see Fig. 3.2d), extending laterally to the outer rim of the disk, where the WGMs are confined (see Fig. 2.3b). The waveguide-coupled disk resonator has a total thickness of  $\sim 310$  nm, the waveguide has a designed top width of 200 nm and the disk has a design radius of 3  $\mu\text{m}$ . As discussed in subsections 2.1.2 and 2.2.2, the spectral positions of the resonance peaks, the Q-factors and the FSR depend sensitively on the h-BN thickness and the disk radius. Using finite element simulations as a guide (COMSOL), we define the disk radius for the given stack thickness in order to optimize the resonances for the MoS<sub>2</sub> emission spectrum.

## 3.2 Optical characterization

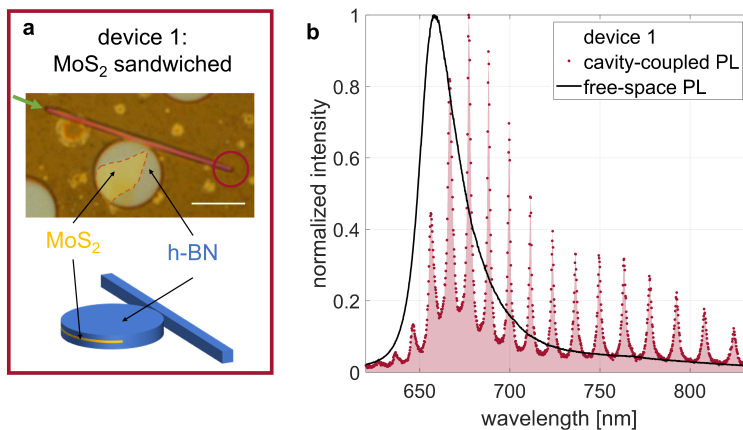


**Figure 3.3:** (a) Device 1: waveguide-coupled disk resonator with a monolayer MoS<sub>2</sub> sandwiched inside the h-BN. The scale bar is 5  $\mu\text{m}$ . Corresponding data is shown in red. (b) Cavity-coupled PL measurements with excitation at one waveguide facet and detection at the other waveguide end for a disk resonator with a monolayer MoS<sub>2</sub> sandwiched inside the h-BN (device 1, in (a)). In addition the free-space PL measurement of the monolayer MoS<sub>2</sub> is plotted for comparison.

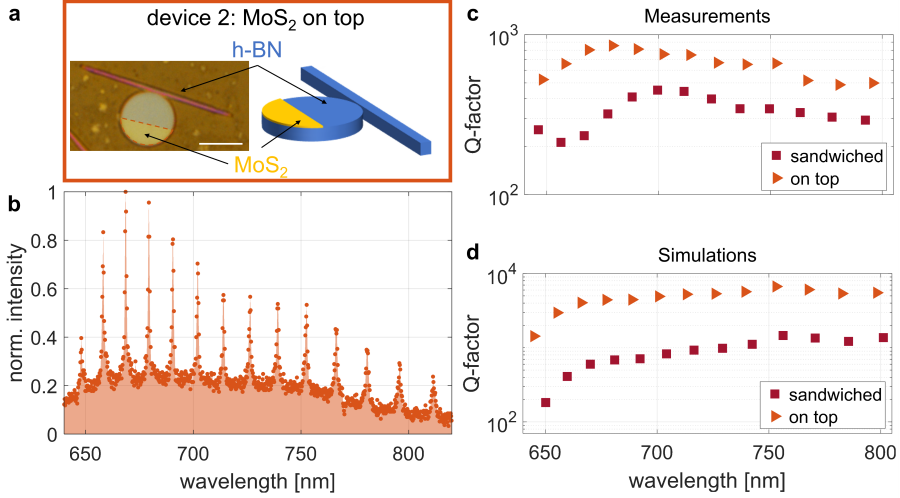
To depict the optical characteristics of the integrated device, we perform spatially resolved spectral measurements. We excite the vdW disk from one end of the waveguide with a 532 nm cw laser and detect the PL emission at the other end (as illustrated in Fig. 3.3a). The light coupled out at the end of the waveguide is captured at high angles with an oil-immersion objective (NA=1.4).

Figure 3.3b shows the spectrum (red) of the cavity-coupled exciton emission at the end of the waveguide. The recorded spectrum features sharp peaks at wavelengths that satisfy the resonance conditions of the disk resonator. These peaks are in the spectral region of the monolayer MoS<sub>2</sub> PL, and therefore verify the coupling of the exciton emission to the WGMs of the disk resonator. Interestingly, however, the envelope function of the resonances does not coincide with the free-space PL (black line in Fig. 3.3b). Instead, the highest peak intensity of the cavity-coupled PL is positioned at wavelengths longer than the free-space PL emission peak. We suggest that the reabsorption of the emitted PL in the cavity by the MoS<sub>2</sub> monolayer itself is a possible explanation for this observation, which is considered in more detail in chapter 4.

### 3.3 Comparison to evanescent coupling (on top)

In the following, we want to discuss the differences when placing a monolayer TMD on top of the photonic structure to achieve coupling via the evanescent fields. For this comparison, a device with monolayer MoS<sub>2</sub> transferred on top of the h-BN disk was fabricated (device 2) (sketch and optical microscope image in Fig. 3.4a). For this device, an area on the same vdW stack next to device 1, but without integrated MoS<sub>2</sub> was chosen. To not expose the monolayer to chemicals during the fabrication process, the MoS<sub>2</sub> monolayer was transferred on top of the already pre-patterned h-BN – h-BN structure. Both devices have an equivalent height of 310 nm, an identical geometry and the same orientation.

Figure 3.4b shows the cavity-coupled PL spectrum for device 2, obtained with the same measurement scheme as for device 1. The coupling of the monolayer to the disk is verified by monolayer MoS<sub>2</sub> PL featuring distinct peaks that



**Figure 3.4:** (a) Device 2: waveguide-coupled disk resonator with a monolayer MoS<sub>2</sub> transferred on top of the h-BN. The scale bar is 5 μm. Corresponding data is shown in orange. (b) Cavity-coupled PL measurements with excitation at one waveguide facet and detection at the other waveguide end for a disk resonator with a monolayer MoS<sub>2</sub> placed on top of the h-BN (device 2, in (a)). (c) Q-factors of device 1 (red squares) and device 2 (orange triangles), extracted from measurements. The drop at wavelengths corresponding to the exciton transition energy of the monolayer verifies the interaction of emitter and cavity. The Q-factor of device 1 is lower than that of device 2, indicating a higher interaction when sandwiching the monolayer inside, placing it at higher mode intensities. (d) Simulated Q-factors for the two structures that show qualitatively similar behavior.

correspond to the WGM resonances.

To evaluate the coupling depending on the vertical position of the monolayer, we plot in Fig. 3.4c the Q-factors of device 1 (red squares) and 2 (orange triangles) as a function of wavelength. The Q-factors of the emission peaks are wavelength dependent. We attribute this to the optical properties of the incorporated monolayer. The real part ( $n_{\text{MoS}_2}(\lambda)$ ) and the imaginary part ( $\kappa_{\text{MoS}_2}(\lambda)$ ) of the refractive index of the monolayer MoS<sub>2</sub> change with wavelength in the given range (see Fig. A.4b in the Appendix A.2.1). As discussed in subsection 2.1.2, absorption losses can influence the Q-factor.  $Q_{\text{abs}}$  is a function of absorption ( $\alpha$ ) and effective refractive index ( $n_{\text{eff}}$ ) (cf.

equation 2.4) [145, 147]. The influence of  $n_{\text{MoS}_2}(\lambda)$  on  $n_{\text{eff}}$  is negligible. However, the strong increase in  $\kappa_{\text{MoS}_2}$  around the exciton transition can lead to significant absorption and therefore to a strong drop of the total Q-factor for wavelengths in this spectral range. Thus, the drop in Q-factor verifies the interaction between the cavity and the monolayer for both devices.

In the Appendix A.2.1 another device with sandwiched monolayer MoS<sub>2</sub> that confirms the strong dip in Q factor at the exciton transition is presented. In addition, these Q-factors were determined by measurements when coupling a broadband laser source into one waveguide end and detecting at the other side. Therefore, the Q-factor can be extracted for a broader wavelength range. This enables us to even observe a second dip in Q-factor for shorter wavelengths. The dip is visible at wavelengths that overlap with the B-exciton transition, which is also visible in  $\kappa_{\text{MoS}_2}$  (see Fig. A.4 in the Appendix A.2.1). This is an additional indication that the spectral behavior of the Q-factor depends on the optical properties of the incorporated monolayer MoS<sub>2</sub>.

The overall Q-factor of device 2 is higher than that of device 1. A possible explanation for this is the increased mode overlap between the WGMs and the monolayer when positioning the emitter inside the resonator. Since a larger fraction of the mode is confined inside the monolayer, more light is absorbed, resulting in a lower Q-factor. While commonly a higher Q-factor is desired, here the reduced Q-factor verifies the improved coupling in our sandwiched device architecture.

The measurements are verified, by comparison to simulations (see Fig. 3.4d). The MoS<sub>2</sub> monolayers are integrated in the simulations by adding a layer with a thickness of 0.7 nm with a refractive index taken from Ref. [111]. The vertical position of the integrated layer was adapted to the considered stack. Even though the overall simulated Q-factor is much higher, the same trend is observable, underlining the higher interaction between cavity mode and emitter in a sandwiched structure. We want to point out that even though the experiments and simulations agree qualitatively well, other effects might also contribute. Differences in the fabrication of device 1 and device 2 might also

lead to changes in the overall Q-factor. We have verified the dip in Q-factor at the exciton transition for further waveguide-coupled disk resonators with integrated monolayer TMDs. However, for the device with the monolayer placed on top, additional reference devices are necessary to exclude the contribution of other effects.

## 3.4 Conclusion

In this chapter we have introduced the first integrated device, following our approach of integrating the active layer directly inside the light confining dielectric. We have demonstrated the coupling of the PL from a monolayer MoS<sub>2</sub> to the WGMs of a waveguide-coupled h-BN disk resonator. Furthermore, we have compared the device to a structure with a monolayer placed on top of the disk. We have seen that at wavelengths corresponding to the exciton transition, the Q-factor drops, verifying the interaction between the resonator and the monolayer MoS<sub>2</sub>.



# 4

---

## Coupling interlayer excitons to whispering gallery modes (WGMs) of h-BN disk resonators

\*

In the previous chapters, we have established a platform for the integration of ML TMDs, inside h-BN disk resonators at high field intensities. We now further expand it and take full advantage of the versatility of vdW heterostructures. By integrating a HBL of two dissimilar monolayer TMDs inside waveguide-coupled h-BN disk resonators (as illustrated in Fig. 4.1), we couple the interlayer exciton emission to the WGMs of the disk resonator.

In the following, we first discuss the device concept and what design adjustments had to be considered. We then turn to a more extended optical characterization of the device. Thereby, the coupling of the interlayer exciton emission is compared to the coupling of the intralayer exciton emission.

---

\*This chapter is based on the article R. Khelifa, P. Back, N. Flöry, S. Nashashibi, K. Malchow, T. Taniguchi, K. Watanabe, and L. Novotny. *Coupling Interlayer Excitons to Whispering Gallery Modes in van der Waals Heterostructures*, *Nano Letters*, **20**, 6155-6161 (2020). Adapted with permission from [73]. Copyright 2020 American Chemical Society.

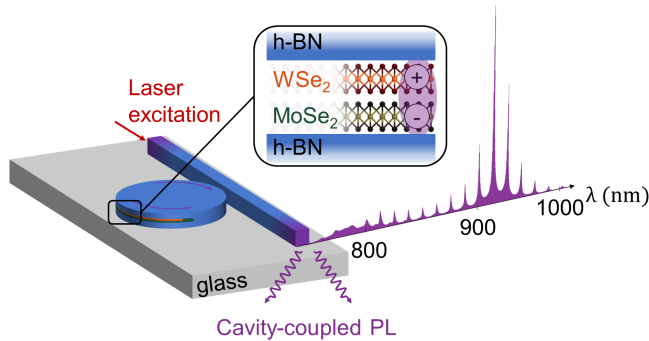


**Figure 4.1:** Illustration of a waveguide-coupled disk resonator with integrated HBL. The HBL is sandwiched between two h-BN flakes. The emission from the interlayer exciton is coupled to WGMs of the disk resonator and then outcoupled through the same waveguide used for excitation.

## 4.1 Device concept and design optimization

The device concept is based on the same approach as described in chapter 3. The major difference is that as active material, two mechanically exfoliated monolayers of WSe<sub>2</sub> and MoSe<sub>2</sub> were integrated. The crystallographic axes of the two monolayers are rotationally aligned. Figures 4.2a and b (magnified) show optical microscope images of such an h-BN – MoSe<sub>2</sub> – WSe<sub>2</sub> – h-BN heterostructure on a glass substrate. To pattern the waveguide and the disk resonator, we follow the same fabrication procedure as described in chapter 3, which is illustrated in Fig. 4.2d.\*

Figure 4.2c shows the final device. The disk resonator has a total thickness of ~310 nm (bottom h-BN: ~150 nm and top h-BN: ~158 nm) and a design radius of 4.25  $\mu\text{m}$ . The disk radius was adjusted because the emission wavelength of the interlayer exciton is at longer wavelengths (~923 nm, see Fig. 1.4c) compared to the emission of the monolayer MoS<sub>2</sub> (~660 nm, chapter 3).

---

\*One difference is that the heterostructure was stacked under inert argon (Ar) atmosphere in a glovebox (details in the Appendix A.1.1).

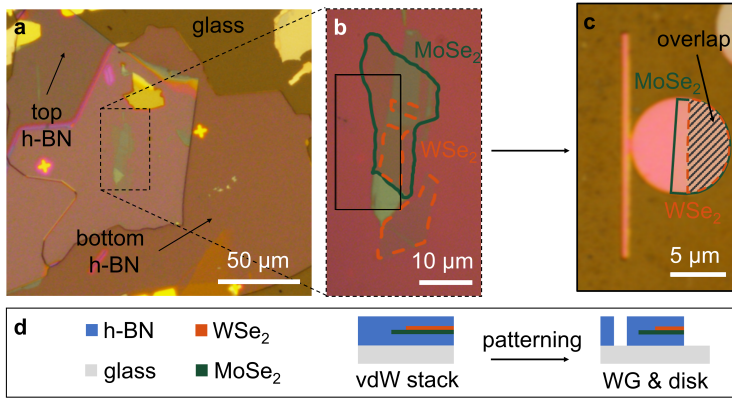


**Figure 4.2:** (a,b) Optical microscope images of the h-BN – MoSe<sub>2</sub> – WSe<sub>2</sub> – h-BN heterostructure after stacking. The heterostructure has a total thickness of ~310 nm (bottom h-BN: ~150 nm and top h-BN: ~158 nm). (c) EBL and RIE were utilized to pattern the vdW heterostructure into a waveguide-coupled disk resonator with a design radius of 4.25 μm. (d) Schematic of the fabrication procedure, showing cross-sections of the vdW heterostructure after stacking and after subsequent patterning into a waveguide (WG)-coupled disk resonator (not to scale).

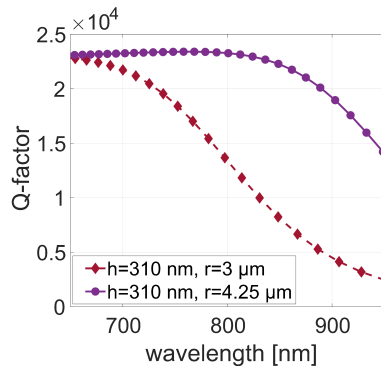


**Figure 4.3:** Simulated Q-factors of two h-BN disk resonators, both with a thickness of 310 nm. The radius was chosen as 3 μm (red diamonds, and red dashed line as guide for the eye) and as 4.25 μm (purple circles, and purple line as guide for the eye).

Figure 4.3 shows the simulated Q-factors for devices with a height of 310 nm and a radius of 3 μm (red diamonds), as well as 4.25 μm (purple circles). While a radius of 3 μm is sufficient for the integration of monolayer MoS<sub>2</sub>, a decrease

in Q-factor can be observed for longer wavelengths. Consequently, for the device with an integrated MoSe<sub>2</sub> – WSe<sub>2</sub> HBL, the designed disk radius should be adapted to a higher value. We choose 4.25  $\mu\text{m}$  and not a higher radius, because with increasing disk radius the FSR decreases. In addition, the width of the waveguide was increased to make sure that the waveguide supports fundamental modes at the emission wavelength (600 nm designed top width).

## 4.2 Optical characterization

Next, we characterize the h-BN disk resonator with integrated TMD HBL. We vary the location of the excitation in order to investigate the coupling of the interlayer emission to the WGMs of the disk. As shown in the sketch and the optical microscope image in Figs. 4.4a and b, coupling between WGMs and interlayer excitons can be achieved by placing the excitation spot near the edge of the disk. We use the same objective for excitation and detection (oil immersion, NA=1.4). The emission is detected either at the same position as the excitation spot or at the ends of the waveguide. This allows us to compare the spectra of free-space PL (detected at the excitation spot on the disk) and cavity-coupled PL (detected at the waveguide end). As shown in Fig. 4.4c, the spectrum of the free-space PL is in agreement with the expected interlayer emission of the HBL (cf. Fig. 1.4c). On the other hand, the cavity-coupled spectrum, detected at the waveguide end, exhibits distinct peaks that are separated by the FSR of the WGMs of the disk resonator. We emphasize that in contrast to several other recent studies [49, 51, 65], the waveguide-coupled spectrum features a reduced background because it is not superimposed to free-space PL.

### 4.2.1 Comparison of intralayer and interlayer coupling

As shown in Fig. 4.5a, the two TMDs forming the HBL do not overlap over the entire footprint of the disk. There are regions where only the MoSe<sub>2</sub> monolayer can be directly excited. Figure 4.5b shows the corresponding spectrum of the free-space and cavity-coupled PL. The main contribution of the cavity-coupled PL comes from the intralayer exciton emission of the MoSe<sub>2</sub> monolayer. The envelope function of the resonances does not coincide with the free-space PL,

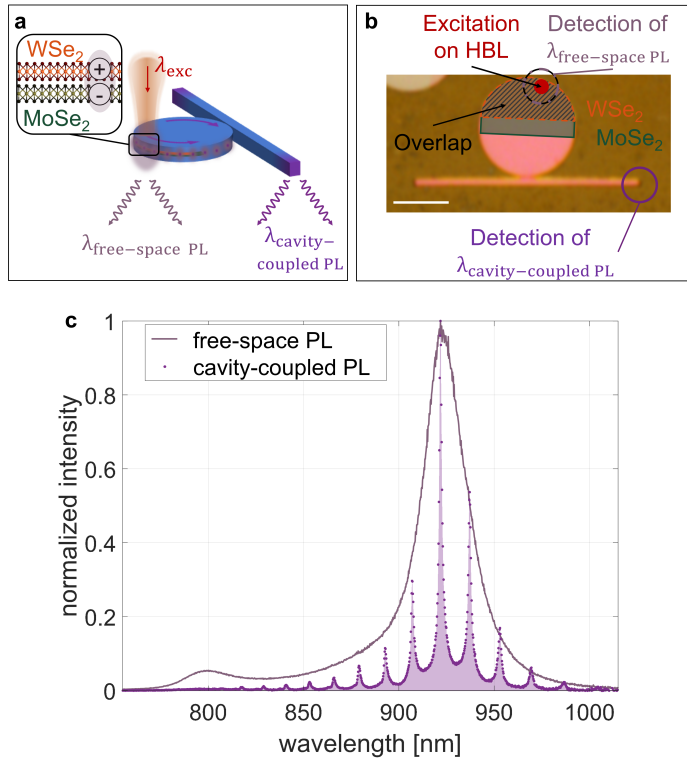


**Figure 4.4:** (a) Illustration of cavity-coupled and free-space detection. (b) Optical microscope image indicating the locations of excitation and detection, and the regions with  $\text{MoSe}_2$ ,  $\text{WSe}_2$  and their overlap (HBL region). The structure is excited with a 633 nm cw laser at the edge of the disk, on the HBL region. The scale bar is 5  $\mu\text{m}$ . (c) Measured spectrum at the waveguide end (cavity-coupled PL) and at the excitation spot (free-space PL). Interlayer exciton emission can be detected at the ends of the waveguide. The PL detected at the excitation spot coincides well with the envelope function of the cavity-coupled PL.

measured at the excitation spot, which is in agreement with the measurements of the device with integrated monolayer  $\text{MoSe}_2$  (chapter 3). As we have seen in chapter 2 and 3, the interaction between the WGMs and the monolayer in a sandwiched device is stronger, due to the increased mode overlap. This reinforces the fact that the emitted PL in the cavity can be reabsorbed by the monolayer itself. Consequently, we attribute the shifted peak maximum of the

#### 4 Coupling interlayer excitons to whispering gallery modes (WGMs) of h-BN disk resonators

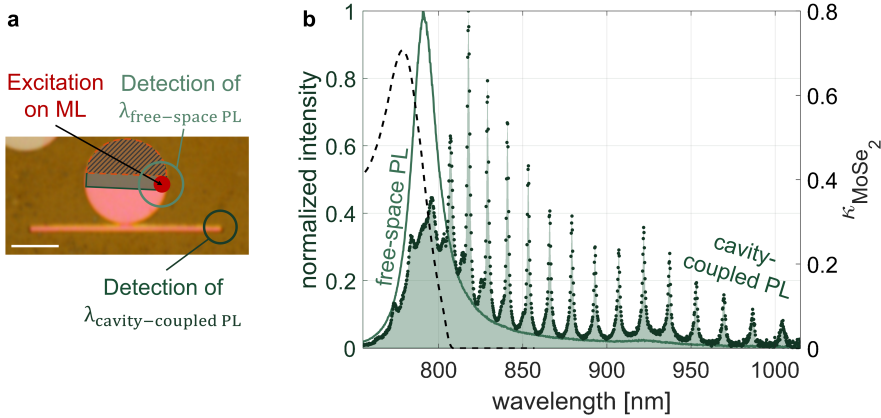


**Figure 4.5:** (a) Optical microscope image, illustrating the measurement scheme when exciting the MoSe<sub>2</sub> monolayer (ML) region. The scale bar is 5 μm. (b) Measured spectra at the waveguide end (cavity-coupled PL) and at the excitation spot (free-space PL), when exciting at the MoSe<sub>2</sub> monolayer region, as indicated in the (a). The envelope function of the cavity-coupled PL does not coincide with the free-space PL, which might be explained by reabsorption of intralayer emission by the MoSe<sub>2</sub> monolayer itself. The dashed curve indicates the imaginary part of the refractive index of MoSe<sub>2</sub>,  $\kappa_{\text{MoSe}_2}$ , from Ref. [164].

cavity-coupled PL mainly to reabsorption.

Also in other works, the improved coupling to red-shifted cavity modes can be observed [49, 54, 165, 166]. To explain this, a recent study has attributed the redshifting to phonon-exciton interactions [165]. In their model, additional phonon-mediated scattering of excitons into the cavity mode is dominating for red-detuned cavity modes. To verify their observations temperature-dependent PL measurements were performed. In their study the monolayer was placed on top of the photonic structure, hence it has a reduced mode overlap and therefore the contribution of reabsorption is expected to be smaller. In general, the influence of phonon-mediated scattering or other effects on our observations, cannot be excluded.

Our interpretation is supported by the absorption spectrum of MoSe<sub>2</sub>, visualized by the extinction coefficient,  $\kappa_{\text{MoSe}_2}$  (taken from Ref. [164]), which

we include in Fig. 4.5b (dashed curve). Thus, the spectral overlap of the PL with the extinction coefficient causes significant reabsorption for wavelengths in this spectral range. As a result, the corresponding peak intensities of the cavity-coupled PL are reduced for these wavelengths. The peaks at longer wavelengths have an additional contribution from interlayer emission from the HBL. This emission is made possible by the reabsorption of the monolayer emission in the overlap region of the two TMDs. Note that for MoSe<sub>2</sub>, it has been shown that the absorption and PL emission peak spectrally overlap more than shown in Fig. 4.5b [167]. The differences might be explained by variations between the  $\kappa_{\text{MoSe}_2}(\lambda)$  of our sample and the data from Ref. [164]. A larger overlap between the peak in  $\kappa_{\text{MoSe}_2}(\lambda)$  and the PL, further promotes the reabsorption effect.

Following this interpretation, the coupling of interlayer excitons to WGMs instead profits from low intrinsic reabsorption. As discussed in subsection 1.4, the interlayer exciton emission energy is lower than the optical band gaps of the individual monolayers, which leads to weak reabsorption of the interlayer emission. Reabsorption is further suppressed by the weak oscillator strength and the reduced absorption of the interlayer exciton transition [127, 129]. This is in agreement with our measurements shown in Fig. 4.4c, where the HBL has been excited. Here, the free-space PL agrees well with the envelope function of the cavity-coupled resonance peaks.

To summarize, our data indicates that the intralayer emission from monolayer TMDs is strongly reabsorbed compared to the interlayer emission. The integration of a HBL inside the disk resonator consequently has two benefits: 1) strong absorption of the excitation by intralayer excitons and 2) weak reabsorption of the interlayer emission within the cavity.

### 4.2.2 Waveguide-coupled excitation and read-out

To allow for an absolute comparison of intralayer and interlayer coupling to WGMs, we now discuss waveguide-coupled excitation and read-out of the disk resonator (Fig. 4.6a). The data in Fig. 4.6b shows that the highest peak intensity

## 4 Coupling interlayer excitons to whispering gallery modes (WGMs) of h-BN disk resonators

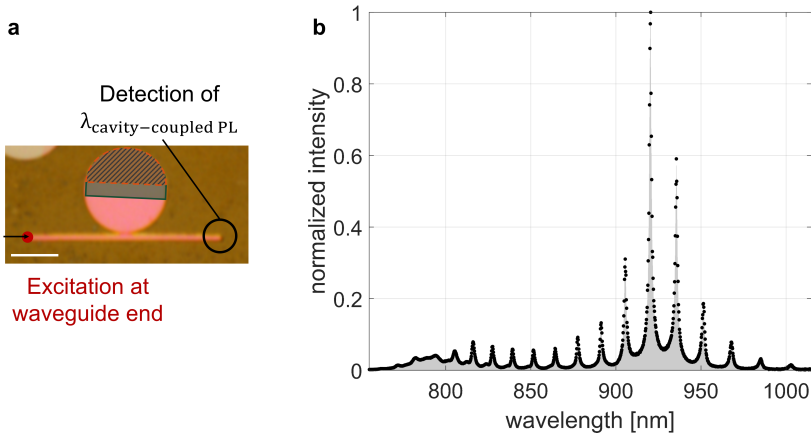


**Figure 4.6:** (a) Optical microscope images, illustrating the measurement scheme when exciting at one waveguide facet and detecting at the other end. The scale bar is 5  $\mu\text{m}$ . (b) Cavity-coupled PL spectrum featuring distinct peaks separated by the FSR of the WGMs of the disk resonator. The resonator is excited at  $\lambda = 633 \text{ nm}$  from one end of the waveguide and the PL is detected at the other end.

is observed at wavelengths corresponding to the interlayer emission.\* In fact, the monolayer emission is suppressed, in agreement with our previous conclusions. Our waveguide-coupled experiments further support our previous assumptions that intralayer emission from TMD monolayers is largely reabsorbed.

### 4.2.3 Q-factor

Figure 4.7 shows the Q-factors of the emission peaks, which again exhibit wavelength dependence that we attribute to the optical properties of the incorporated TMD HBL. The highest values are  $\sim 570$  and occur at wavelengths that correspond to the interlayer emission peak. In contrast, a considerably lower Q-factor is observed for wavelengths near the optical band gap of  $\text{MoSe}_2$ , in agreement with the observations in chapter 3. Because the absorption spectrum of a HBL is mainly governed by the absorption of the individual monolayers [127, 128], the reabsorption of interlayer emission is significantly weaker, which is evidenced by the high Q-factor at wavelengths near the

\*Note that the spectra are corrected for the wavelength-dependent transmission of our measurement setup and the CCD detection efficiency.



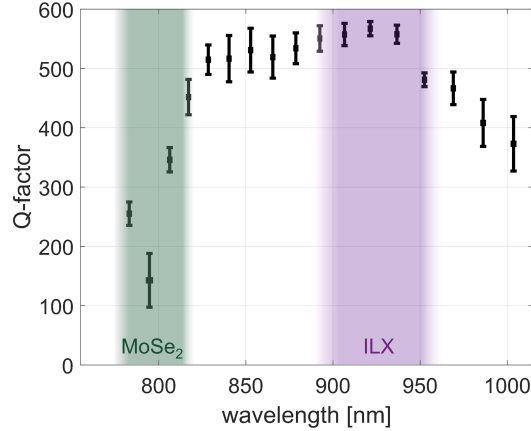


**Figure 4.7:** Wavelength dependence of the Q-factor, determined by fitting Lorentzian functions to the measured resonances. Measurements were taken for different locations of excitation (HBL, monolayer, waveguide end) and detection at both waveguide ends. The means and the standard deviations are shown in the figure. A strong drop in Q-factor can be observed at the absorption wavelengths of the intralayer exciton transition of MoSe<sub>2</sub>. No drop in Q-factor is observed for wavelengths of the interlayer exciton transition, indicating low absorption.

interlayer transition. The decrease in Q-factor at longer wavelengths (>950 nm) might be explained by radiation losses, which increase at longer wavelengths (see subsection 2.2.2).

With the experimental Q-factor and simulations, the Purcell enhancement can be estimated to be  $\sim 3$  (at the resonance wavelength closest to 920 nm).<sup>\*</sup> The enhancement is not very strong owing to the relatively high effective mode volume and the modest Q-factor of the disk resonator in our case.

## 4.3 Conclusion

In this chapter, we have further expanded the vdW photonics platform by coupling interlayer excitons from a TMD HBL to WGMs of an h-BN disk resonator. As in the case of structures with integrated monolayers (chapter 3),

<sup>\*</sup>Details on the determination of the Purcell factor can be found in the Appendix A.2.3.

#### 4 Coupling interlayer excitons to whispering gallery modes (WGMs) of h-BN disk resonators

---

we follow the approach of maximizing the mode overlap between the emitter and the WGMs by sandwiching the HBL inside the h-BN disk. Again, the spectral characteristics of the Q-factors can be attributed to the optical properties of the incorporated TMDs. While the absorption characteristics of a HBL are governed by the absorption of the individual monolayers, the main emission stems from the energetically lower interlayer exciton transition. This gives rise to cavity-coupled interlayer exciton emission that is only weakly reabsorbed, resulting in a higher Q-factor at the emission wavelength.

# 5

---

## Waveguide-coupled exciton LEDs

\*

After the successful demonstration of optically excited emitters integrated with h-BN photonic structures, we now turn to the discussion on the integration of electrically driven light sources. We demonstrate waveguide coupled vdW LEDs and present further steps towards an all 2D material-based on-chip photonics platform to enable the integration of optoelectronic devices at regions of high field intensities. We achieve this by directly integrating vdW-based exciton LEDs inside h-BN waveguide structures, as illustrated in Fig. 5.1. As a result, the light emitted by the LED is successfully coupled to the waveguide.

---

\*This chapter is in parts adapted from Ref. [110]: R. Khelifa<sup>†</sup>, S. Shan<sup>†</sup>, A. J. Moilanen, T. Taniguchi, K. Watanabe, and L. Novotny. *WSe<sub>2</sub> Light-Emitting Device Coupled to an h-BN Waveguide*, *ACS Photonics*, **10**, 1328-1333 (2023), [CC BY 4.0](#).

<sup>†</sup> These two authors contributed equally.

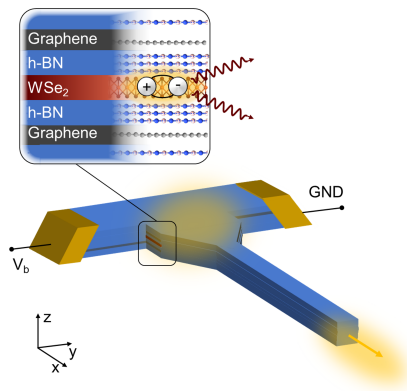


**Figure 5.1:** Illustration of the waveguide-integrated vdW LED: a  $\text{WSe}_2$ -based tunneling device is integrated close to the vertical center of an h-BN waveguide structure.

## 5.1 Device concept and design

The here presented prototype device combines in one structure both: electrically driven photon generation and in-plane redirection of guided light fields. In order to realize this, it is necessary to carefully engineer the design of the structure in such a way that the optical mode is not disturbed by the presence of the metal contacts, while charge carrier injection and photon generation are still possible. In this regard, we first discuss the device configuration of the vdW LED. Next, we elaborate on the contacting scheme of an LED integrated inside a photonic structure. Then, the design of the optical structure and its geometrical requirements are examined.

### 5.1.1 LED and electrical contacts

To date, a wide range of different TMD-based LEDs have been demonstrated [37, 38, 45, 57, 129, 134, 168–170]. We decide to focus on devices with light emission from single TMD monolayers, more precisely from intralayer excitons (in contrast to interlayer excitons from HBLs). Furthermore, to reduce the number of necessary contacts, we choose a device architecture that does not require additional gating.

As illustrated in Fig. 5.1, the tunneling LED design, introduced in section 1.5 was used. Upon charge carrier injection with Gr electrodes via the h-BN tunnel barriers, radiative recombination inside the monolayer WSe<sub>2</sub> leads to light emission from the overlap region. Such a device structure then is expected to have an emission that is dominated by neutral excitons and consequently by in-plane oriented dipole emitters [118, 171].

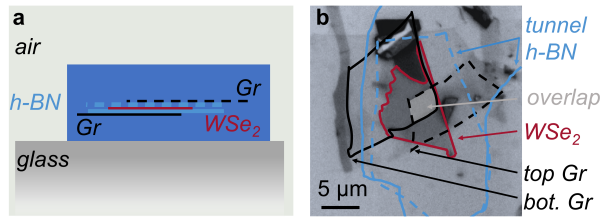


**Figure 5.2:** (a) Schematic cross-section (not to scale) and (b) reflection map of the vdW heterostructure after stacking: top h-BN ( $\sim 130 - 135$  nm) – Gr (1 layer) – h-BN ( $4 \pm 1$  layers) – WSe<sub>2</sub> (1 layer) – h-BN ( $4 \pm 1$  layers) – Gr (1 layer) – bottom h-BN ( $\sim 105$  nm).

The vdW heterostructures, consisting of the LED encapsulated between thick h-BN flakes, were exfoliated and stacked with the same approach as the earlier discussed devices.\* Figure 5.2a and b, show a schematic and a reflection map of the vdW heterostructure on the glass substrate after stacking.

To contact the Gr electrodes that are enclosed by the thick h-BN layers, we used the technique of edge contacts, which has been established as one of the standard approaches for electrical contacting of encapsulated Gr [162, 172] or TMD [173] monolayers. Etching of the vdW stack prior to the metal deposition enables the contacting at the edge of the Gr (cf. Fig. 5.3b). In our devices, the exact location of the Gr flakes was identified with the reflection map shown in Fig. 5.2b. EBL was used to define the pattern of the contacts, next, the stack was etched by RIE, and chromium (Cr) and gold (Au) were evaporated as contact metals (the recipe was adapted from Ref. [162, 172]<sup>†</sup>).

\*Note that due to limitations while stacking with a thick top h-BN, the stack consists of a thin and a thick top h-BN. More details on the stacking process are discussed in the Appendix A.1.1.1.

<sup>†</sup>More details about the fabrication of the edge contacts are discussed in the Appendix A.1.1.3.

The heterostructure after contacting is shown in Fig. 5.3a. The SEM image of the edge contact on a reference device is shown in Fig. 5.3c.

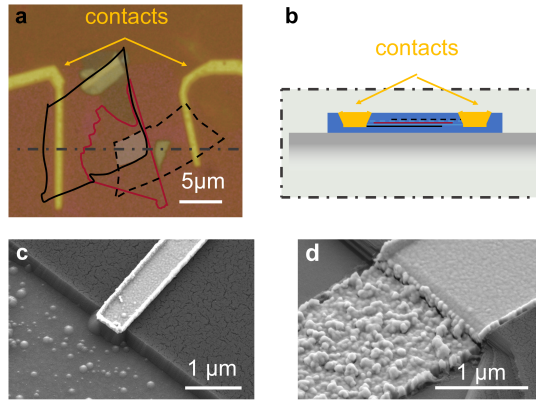


**Figure 5.3:** (a) Optical microscope image of the contacted LED after fabrication of the Gr edge contacts. The gray area indicates the overlap region of all flakes. (b) Schematic cross-section of the contacted LED, as indicated by the dashed line in (a) (not to scale). (c) SEM image of an edge contact on an h-BN – Gr – h-BN reference stack. (d) SEM image of the metal step from the remaining h-BN flake after etching to the glass substrate (reference device with h-BN flake only).

To ensure that the integrated devices are not limited by high contact resistances, we performed transfer length method (TLM) characterizations on a reference stack with encapsulating h-BN thicknesses that are in the same range as for the here presented LED.\* We estimate the contact resistance to be  $200 - 300 \Omega \mu\text{m}$ , which is in a comparable order of magnitude as previously reported [162, 174]. Whereby the resistance of the metal wires is non-negligible, possibly due to the high glass roughness after etching and the large step size, both observable in Fig. 5.3d.

### 5.1.2 Concept and design of the patterned waveguide-structure

To couple the light, emitted from the LED region to the waveguide mode, the vdW stack containing the LED and the thick h-BN slabs is patterned into a photonic structure using EBL and RIE with a Polymethylmethacrylat (PMMA)

\*Details about the TLM characterization can be found in the Appendix A.3.2.

mask (see microscope image and schematic of the final device in Fig. 5.4a and b).\*

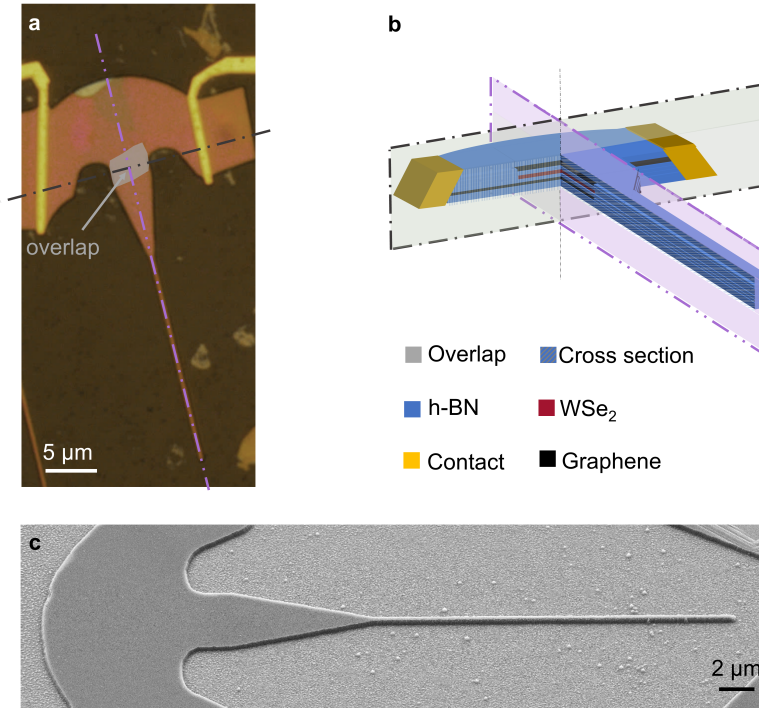


**Figure 5.4:** (a) Optical microscope image of the contacted LED after fabrication of the Gr edge contacts. The gray area indicates the overlap area of all flakes and therefore the emission region of the LED. (b) Schematic cross-sections of the contacted LED, as indicated by the dashed line in (a) (not to scale). (c) SEM image of the photonic structure etched into a reference h-BN flake.

This step utilizes the real space electroluminescence (EL) map of the unpatterned LED as a reference for the device layout, which is favorable compared to fabrication methods that rely on the accurate transfer of vdW stacks on prefabricated photonic structures [19, 24]. We linearly taper the width of the device down to a narrow single-mode waveguide (at the desired target wavelength), as shown in Figs. 5.4a and c. In the following, we discuss in more

\*The approach is almost the same as for the devices in chapters 3 and 4. Adjustments are discussed in the Appendix A.1.1.2.

detail the conceptual design of the photonic structure.

### **Waveguide design**

The waveguide dimensions were chosen based on the simulations introduced in subsection 2.2.1. The emission of the exciton LED is expected to be dominated by in-plane oriented dipole emission. Thus, the waveguide thickness and width are chosen such that in the wavelength range of the exciton emission ( $\sim 760$  nm) only the fundamental TE modes are supported. As shown in Fig. 2.5a, this can be achieved for a total h-BN thickness of  $\sim 240$  nm and a base width of 550 nm. A sidewall angle of  $55^\circ$  was determined from SEM images on the reference device, shown in Fig. 5.4c. Since the exciton emission of the integrated emitter is broader, the waveguide width was chosen such that the single mode condition is also guaranteed for wavelengths slightly shorter than 760 nm.

### **Lateral design (xy-plane)**

The  $\sim 3.85$   $\mu\text{m}$  wide LED emission region is tapered down (linear taper with a length of 7.75  $\mu\text{m}$ ) to the desired waveguide width. The length of the taper is limited by the area of the stack overlay and stacking imperfections like bubbles. To characterize how the lateral design influences the transmission properties of the coupled system, we perform FDTD simulations with Lumerical Inc.. The mode conversion through the taper is numerically estimated for the fundamental TE mode (wavelength of 760 nm) to be around  $\sim 80\%$ . However, because the exciton emission is mainly attributed to in-plane oriented dipole emitters, further losses are introduced in the coupling between the dipole emission and the fundamental TE mode of the waveguide. For comparisons, further simulations with an in-plane (xy-plane, see axes in Fig. 5.1) oriented single dipole source were performed. Since the emitters are distributed throughout the complete LED region, two major factors influence the coupling efficiency: 1) position (x- and y-direction) of the emitter within the LED emission region and 2) orientation angle within the xy-plane. When taking these spatial and angular variations of the in-plane dipole emitters into account, we numerically estimate a mean coupling efficiency of  $\sim 1.2\%$ .\*

---

\*Mean values of individual sweeps were considered for estimations and are discussed in more detail in the Appendix A.3.3.2.



efficiency might be explained by the fact that the emitters in the LED region can couple to other higher order modes. These, however, are not properly converted to the fundamental TE mode of the waveguide, which introduces high losses. In general, the coupling efficiency can be improved by optimizing the lateral design of the patterned structure [175, 176]. This, however, is beyond the scope of this work.

### **Vertical design (z-axis)**

In chapter 3 and 4, the TMDs were sandwiched close to the vertical center of the encapsulating h-BN slabs. As mentioned in subsection 2.1.1 and as shown in Figs. 2.7a and b, the intensity of the waveguide mode reaches its maximum close to the vertical center of the waveguide. However, the field maximum is slightly misplaced from the vertical center of the waveguide ( $z = 0$  nm). The reason is that the refractive indices of the media outside of the two encapsulating h-BN flakes are different, that is, the waveguide mode leaks more strongly into the glass substrate at the bottom than into the air at the top. Consequently, the bottom h-BN thickness ( $\sim 105$  nm) is chosen to be lower than the top h-BN thickness (130 – 140 nm). Simulations with a dipole emitter at the given vertical position and inside the LED region, show a  $\sim 4$  times higher coupling efficiency (to the fundamental TE mode of the waveguide) compared to a placement of the emitter on top of the h-BN.

## **5.2 Optoelectronic characterization of the unpatterned exciton LED**

In order to determine the exact emission region and to investigate the emission characteristics of the exciton LED, the vdW device was characterized before patterning into a photonic structure (cf. sketch in Fig. 5.5a). For a bias of  $V_b=1.7$  V, EL is detected from the complete overlap region and is visualized in the real space image in Fig. 5.5b. We attribute small variations in the emission region to inhomogeneities and bubbles between adjacent flakes. Figure 5.5c shows representative EL spectra, which are symmetrical for both bias polarities, and only slightly differ in intensity. The emission is dominated by the neutral

exciton with a small contribution from trions [38, 60], as also observable in PL measurements (see orange curve in Fig. 5.5d). The slight red-shift of the EL compared to PL has already been observed for devices with the same architecture [37, 38] and might be due to an increased trion contribution (increased doping level) for EL. Therefore, the electrically driven emission from the device can be attributed to the radiative recombination of excitons in the monolayer  $\text{WSe}_2$ . The maximum external quantum efficiency of the device at a bias of  $V_b = 1.7\text{V}$  is around 4%, which is in the same order of magnitude as the values previously reported for tunneling LEDs with monolayer  $\text{WSe}_2$  at room temperature [38].

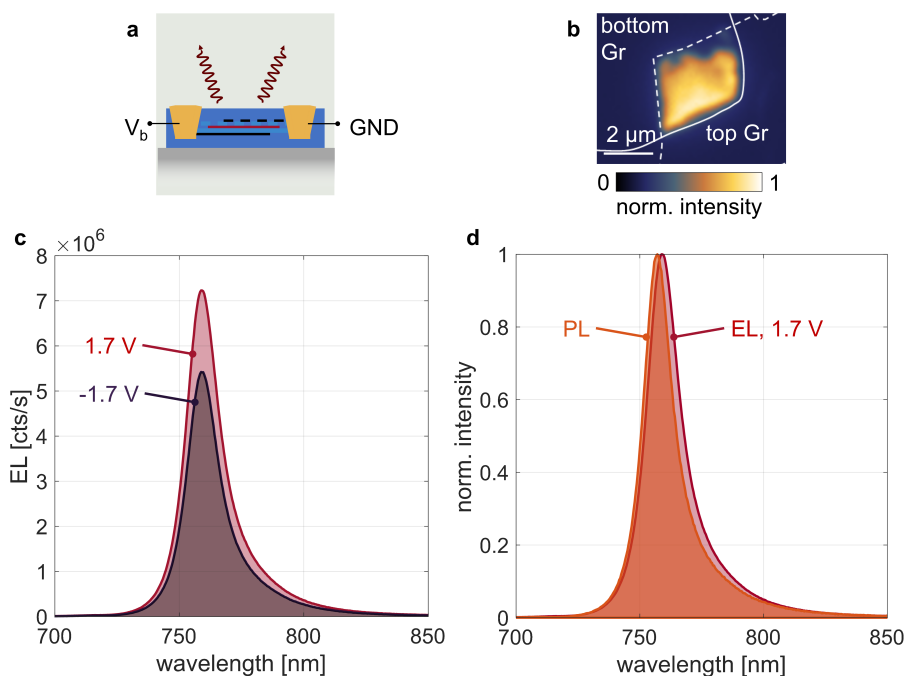
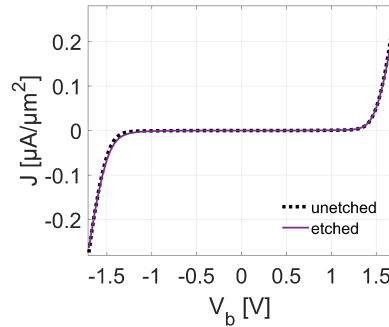


**Figure 5.5:** (a) Schematic cross-section of the unpatterned LED (not to scale). (b) Real space image of the device for an applied bias of 1.7 V. The emission area agrees well with the overlap region. (c) EL spectra of the unpatterned device for a bias of 1.7 V and -1.7 V. (d) PL spectra from a spot at the overlap region of the stack in comparison to the EL emission.

## 5.3 Optoelectronic characterization of the waveguide-coupled exciton LED

Finally, we turn to the main part of this chapter and discuss the electrical and optical characteristics of the vdW LED after patterning into the waveguide structure.

### 5.3.1 Electrical characterization



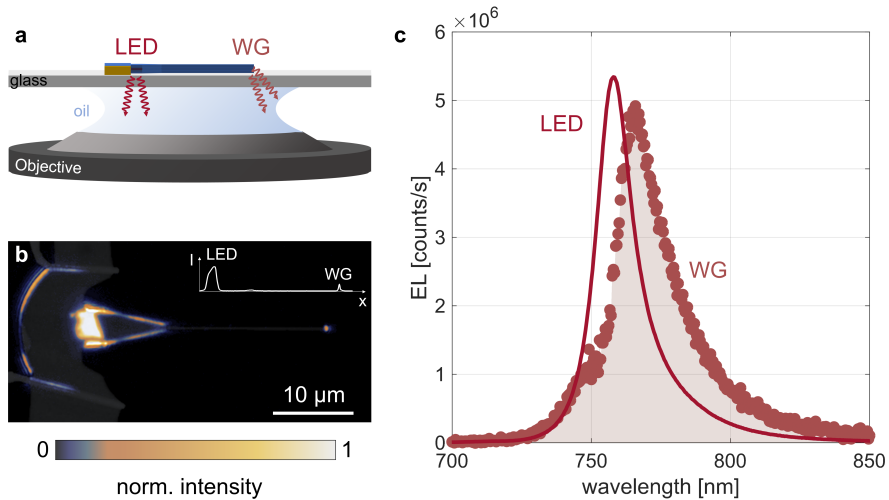
**Figure 5.6:** J-V characteristics of the final device after patterning (purple solid line) in comparison to the J-V measurement before patterning (black dashed line).

Figure 5.6 shows the current density ( $J$ ) characteristics as a function of voltage ( $V$ ) for both, the patterned (purple solid line) and unpatterned (black dashed line) device. The two  $J$ - $V$  curves are nearly identical, indicating that the etching process does not affect the device functionality. For the sake of completeness, it should also be mentioned that the LED showed fluctuations in the current-voltage measurements during a time span of several months. However, these did not affect the characterization of the LED.

### 5.3.2 Electrically driven emission and spatially resolved spectroscopy

After the patterning of the device, we observe a coupling of the electrically driven exciton emission to the waveguide. The etching did therefore not harm

## 5 Waveguide-coupled exciton LEDs



**Figure 5.7:** (a) Illustration of the integrated LED on top of the glass chip, while measuring with the oil immersion objective. As indicated, the LED emission and the waveguide (WG)-coupled emission can be detected at the same time. (b) Real space image of the integrated LED emission, overlaid with the device shape ( $V_b=1.7\text{ V}$ ). Inset: intensity map along the central section of waveguide structure ( $x$ -direction), showing the free-space emission at the LED region and the waveguide-coupled emission. (c) Waveguide-coupled emission (red dotted line) plotted together with the free-space emission (red solid line), demonstrating the successful coupling of the electrically driven exciton emission.

the optoelectronic functionalities of the device.\* The real space image and a spectrum of the waveguide-coupled emission, for an applied bias of 1.7 V, are presented in Figs. 5.7b and c, respectively. In order to detect the emission at the waveguide end, we use the same approach as for the waveguide-coupled disk resonators and collect the light at high angles by an oil-immersion objective ( $\text{NA} = 1.4$ ) through the glass substrate, as illustrated in Fig. 5.7a. As already introduced in earlier chapters, spatially resolved spectral measurements allow us to differentiate between the free-space EL at the LED region and the waveguide-coupled EL at the end facet of the waveguide. However, in the here presented device, the strong scattering at the beginning of the tapering impeded the

\*In the Appendix A.3 two other integrated LEDs are shown. Also for these, EL can still be observed after patterning.

background-free detection of the waveguide-coupled EL. The spectra of the waveguide-coupled emission (red dotted line) after background corrections are plotted in Fig. 5.7c together with the free-space emission at the LED region (red solid line). The spectrum, detected at the end of the waveguide verifies the coupling of the exciton emission from the integrated LED. However, the peak of the waveguide-coupled EL is observed at longer wavelengths compared to the free-space EL. Reasons for this are discussed in subsection 5.3.5.

#### 5.3.3 Angular resolved measurements

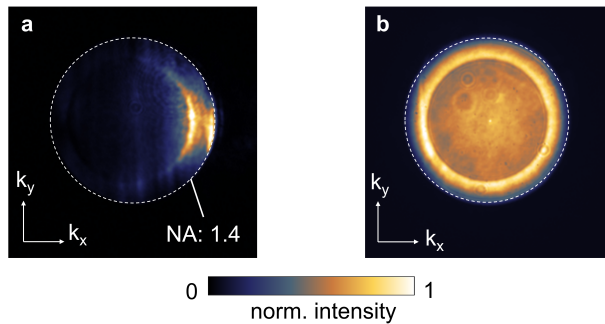


**Figure 5.8:** Normalized Fourier space image of the emission (a) at the end of the waveguide, and (b) of the unpatterned LED.

The angular distribution of the waveguide-coupled EL is measured by Fourier space imaging, shown in Fig. 5.8a.\* We observe light emission into large angles and with high directivity. This emission pattern agrees with the out-coupling of an in-plane propagating waveguide mode. In contrast, Fig. 5.8b shows the Fourier space image from the unpatterned LED before etching. Here, the EL emission pattern agrees with the emission pattern resulting from in-plane oriented emitters. Similar patterns are also observed for PL from monolayer  $\text{WSe}_2$  (see Fig. 1.3b, in section 1.3) and agree with PL studies on TMD monolayers [118].

\*Details on the Fourier space imaging can be found in the Appendix A.1.2.

### 5.3.4 Coupling efficiency

In order to fully characterize the integrated waveguide structure, we now discuss and quantify the experimental coupling efficiency. We determine the coupling efficiency from the integrated spectra (between 700 – 900 nm) shown in Fig. 5.7c according to equation 2.5, which can be approximated to  $\beta \approx \frac{I_{\text{WG}}}{I_{\text{LED}}}$  [156, 157]. For a bias of 1.7V, the uncorrected coupling efficiency is 1.25%. However, as we have seen in the previous subsection (5.3.3), the emission characteristics from the LED region and from the waveguide end are different. The free-space EL at the LED region is, as discussed in subsection 5.3.3, dominated by in-plane emitters oriented in the xy-plane. The waveguide-coupled EL, on the other hand, is an in-plane guided mode, out-coupled through scattering at the end facet of the waveguide. To account for the different collection efficiencies owing to the dissimilar angular distribution of the emission characteristics, correction factors have been determined from simulations. The corrected coupling efficiency is determined to be 0.3% ( $V_b = 1.7\text{V}$ ).<sup>\*</sup> It is important to mention that in the spectral range from 730 – 800 nm, the coupling efficiency varies between 0.1% to 0.8%. The reasons for these spectral variations are discussed in subsection 5.3.5.

Next, we compare the experimental coupling efficiency to the numerically estimated value of 1.2%, presented in subsection 5.1.2. The estimated and measured coupling efficiency are very close and the small variation might be attributed to the losses introduced by the sidewall roughness. In addition, the light passes through part of the WSe<sub>2</sub> monolayer and one of the Gr flakes before reaching the waveguide, which can introduce absorption losses. Overall, we conclude that the experimental coupling efficiency is close to the range expected from numerical simulations, confirming the successful implementation of the presented waveguide-integrated LED.

The coupling efficiency of our device is lower than that of the p-n junction LED evanescently coupled to a Si-based photonic crystal waveguide demonstrated by Bie et al. [19]. However, the total output efficiency (the external quantum

---

<sup>\*</sup>The correction factors for both regions are discussed in the Appendix A.3.3.1.

efficiency of the device multiplied by the coupling efficiency) is more than one order of magnitude higher. In their implementation, the device area has the same dimensions as the waveguide width, which loosens the lateral design restrictions and reduces mode conversion losses (between LED region and the waveguide). As we have mentioned in subsection 5.1.2, our simulations show that the major loss is due to the conversion of higher-order modes from the LED region to the single-mode waveguide. Here, we present a first proof-of-concept device in a photonic platform that is still in its infancy. Consequently, it is expected that with an improved device with optimized lateral design, the coupling efficiency can be further improved to then outperform the coupling efficiency of integrated LEDs with evanescent coupling.

#### 5.3.5 Spectral characteristics of the waveguide-coupled emission

In all integrated devices presented earlier in this thesis, the peak of the waveguide/cavity-coupled intralayer exciton emission is red-shifted relative to the free-space PL/EL emission peak. As visible in Fig. 5.7c, also the peak of the waveguide-coupled EL of the integrated LED is positioned at longer wavelengths. Therefore, after having discussed the important characteristics of the integrated LED, we now turn to a secondary but non-negligible analysis and try to understand the reason for the red-shifted peak of the waveguide-coupled emission in more detail.

In chapter 3 and 4, we have attributed the shift mainly to the reabsorption inside the disk by the monolayer TMD itself. Therefore, we should also investigate if reabsorption can be a possible reason for the shifted waveguide-coupled EL in Fig. 5.7c. Before doing so, however, we shall discuss other effects that could affect the spectral characteristics of the waveguide-coupled EL.

#### Transmission characteristics of the photonic structure

First, we elaborate on the transmission characteristics of the photonic structure and discuss if these can contribute to the shifted peak for the waveguide-coupled EL. The simulated transmission of a waveguide (10  $\mu\text{m}$  long) is shown in Fig. 5.9b (blue circles): for fundamental TE modes, confined in the h-BN

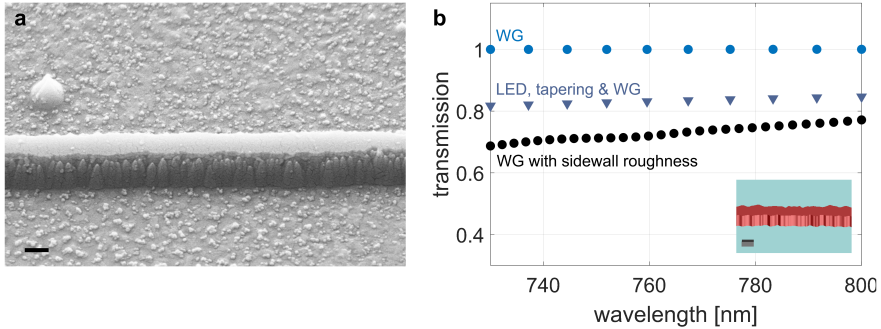


**Figure 5.9:** (a) SEM image of a reference waveguide with identical design and fabrication procedure as the integrated LED structure. The scale bar is 200 nm. (b) Simulated transmission of a waveguide (blue circles), LED, tapering and waveguide (blue triangles) and a waveguide with sidewall roughness (black circles). For all simulations, a mode source and the fundamental TE modes were considered. Inset: Illustration of the waveguide with sidewall roughness for the numerical simulations.

waveguide with a base width of 550 nm and a sidewall angle of  $55^\circ$ , no wavelength-dependent losses are observed. When including the LED and tapering region (blue triangles), the overall losses increase, but the changes with wavelength are negligible. Note that for these simulations the dipolar emission properties are neglected and only the influences of the shape on the confined waveguide modes are considered (mode source in the simulations).

Since the fabricated waveguides have some sidewall roughness, scattering losses might impact the spectrum of the waveguide-coupled EL. This is characterized by the simulated transmission of waveguides with a sidewall roughness ( $\sigma_{\text{RMS}} = 25 \text{ nm}$ ,  $L_{\text{Correlation}} = 50 \text{ nm}$ ), shown in Fig. 5.9b. The root mean square (RMS) values and the correlation length describe the extent of the roughness vertical and horizontal to the waveguide [177] and were estimated according to SEM images of the reference waveguide, shown in Fig. 5.9a (identical fabrication procedure). In subsection 2.1.1, we have discussed that for longer wavelengths the modes are less confined and consequently interact to a higher extent with the sidewall roughness. However, this stands in contrast to the observed increase in transmission for longer wavelengths. A possible reason for this are higher scattering losses for shorter wavelengths at the irregular



scatterers that the sidewall roughness introduces [178, 179]. Thus, the sidewall roughness in our waveguides might explain to some extent the spectral change of the waveguide-coupled EL.

#### Outcoupling and collection efficiency

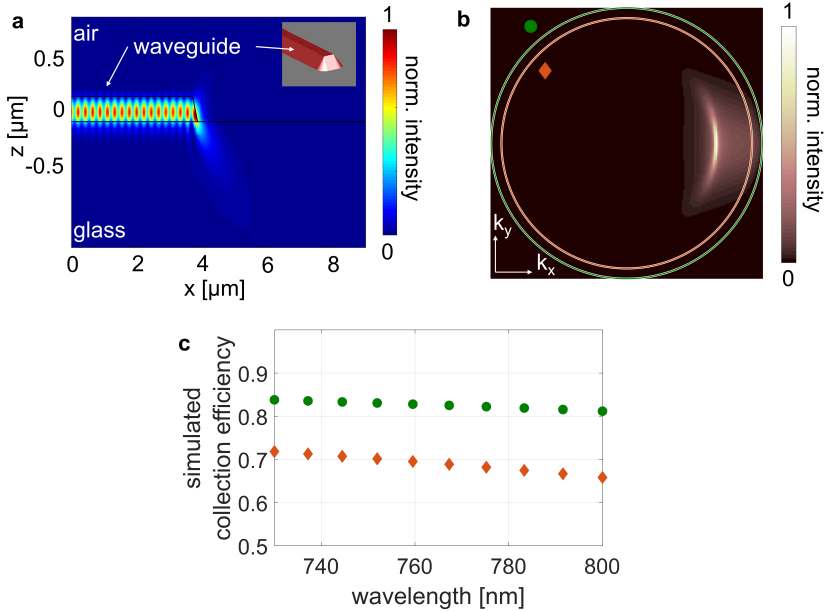


**Figure 5.10:** (a) Simulated field distribution of a cut through the air – waveguide – glass interface, showing that a big fraction of the confined mode is out-coupled into the glass substrate. Inset: simulated waveguide. (b) Simulated angular field distribution. The orange circle (diamond) indicates the collection cone defined by the oil immersion objective (NA=1.4). (c) Wavelength dependence of the simulated collection efficiency for the collection cones, indicated in (b).

Another factor is the spectral dependence of the out-coupling and collection efficiency of the emission at the waveguide end. The waveguide-coupled EL is an in-plane guided mode that is out-coupled without a grating coupler, just by scattering from the end facet of the waveguide. As shown in the simulated field distribution of a cut through the air – waveguide – glass interface in Fig. 5.10a, a large part of the mode is scattered in high angles into the glass substrate. For the simulations, the etching angle at the end facet is taken into

account, as illustrated in the inset of Fig. 5.10a. In the plot of the simulated angular far-field distribution inside the glass (for the fundamental TE mode with  $\lambda = 760$  nm), shown in Fig. 5.10b, the collection cone of our objective (NA of 1.4) is indicated by the orange circle. Within this range, the simulated emission pattern qualitatively coincides with the Fourier measurements shown in Fig. 5.8a. From integration over the simulated intensity, within the collection cone of our objective, the collection efficiency is determined. Figure 5.10c shows that the collection of the out-coupled waveguide mode through the glass substrate changes the spectrum to a small extent, but cannot be responsible for the shift.

### Absorption of the nearby monolayer

Lastly, we turn to the consideration of how the absorption of light by WSe<sub>2</sub> can affect the spectrum as well. This is because part of the WSe<sub>2</sub> is sticking out (red/orange area in Fig. 5.11a) of the overlap region (gray area), penetrating into the tapered region where the light is coupled to. To visualize this effect, we normalize the spectrum at the end of the waveguide to the spectrum at the LED region.  $EL_{WG}(\lambda)/EL_{LED}(\lambda)$  is plotted in Fig. 5.11b for a voltage of 1.7 V (solid black line). To obtain results with a better signal-to-noise ratio, for the waveguide-coupled spectra, measurements for the same voltage but with longer integration times and while blocking the free-space emission from the LED region were used.\* Within the given wavelength range a distinct dip can be observed at around 755 nm, several nm below the free-space EL emission peak, plotted in red (in Fig. 5.11b). Such an abrupt dip has not been observed for the simulations discussed before and also not for the transmission measurements of an identical bare h-BN waveguide (see Fig. 2.4a). This is why we suggest that the spectral behavior can mainly be attributed to the optical properties of the incorporated monolayer.

For comparison, we visualize the absorption characteristics of a monolayer

---

\*Note: small variations in the current were observed between the measurements. Therefore, in this analysis, we focus on the spectral shape and not the absolute values.

### 5.3 Optoelectronic characterization of the waveguide-coupled exciton LED

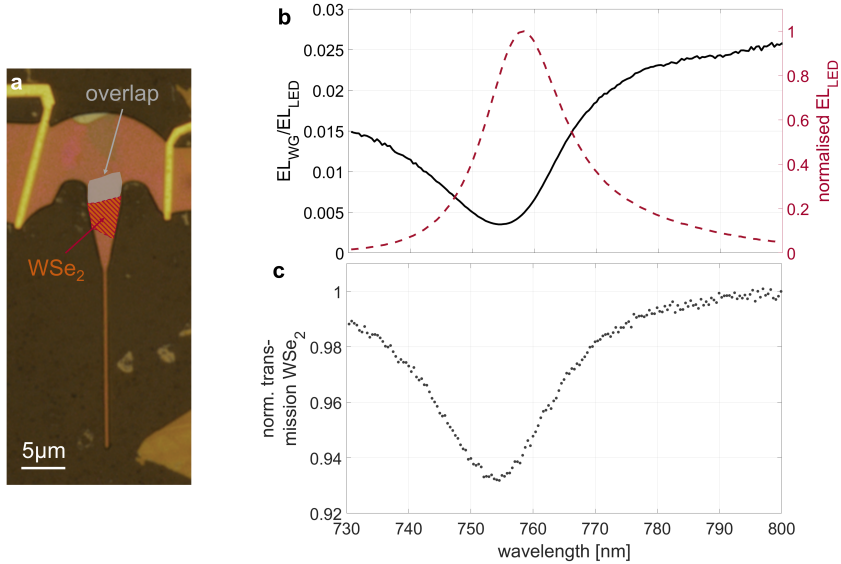


**Figure 5.11:** (a) Optical microscope image of the integrated LED. The light emitted at the LED region (gray area) has to pass through part of the monolayer  $\text{WSe}_2$  that is sticking out (orange area) before reaching the waveguide. (b) Waveguide-coupled EL normalized to the free-space EL (black solid line), visualizing the changes between the two spectra. For comparison, the free-space EL is plotted in red (dashed line). (c)\* Transmission measurement of a  $\text{WSe}_2$  monolayer (encapsulated inside two h-BN flakes) illuminated with a broadband source from the top with detection from below with a second objective. The detected light was normalized to a reference spectrum obtained on the h-BN flakes.

$\text{WSe}_2$  by plotting a free-space transmission spectrum in Fig. 5.11c.\* The monolayer (encapsulated by two h-BN flakes) was illuminated with a broadband source from the top and the transmitted light was detected from below with a second objective. Clearly, the spectral behavior of the integrated LED, plotted in Fig. 5.11b coincides with the free-space measured absorption characteristics of the monolayer (Fig. 5.11c). Furthermore, both measurements agree with the imaginary part of the refractive index ( $\kappa_{\text{WSe}_2}$ ), plotted in Fig. 1.3c (section 1.3) [111]. In earlier studies, the absorption has already been determined to be at wavelengths slightly shorter than the exciton PL

\*This measurement and the post-processing was performed by Antti Moilanen on a stack that was fabricated by him.

emission [167]. Therefore, we can conclude that the spectral agreement with the absorption characteristics of WSe<sub>2</sub> indicates that the absorption of the monolayer part that is sticking out of the overlap region indeed contributes to the spectral shape of the waveguide-coupled EL.

The influence of absorption on the shift of the waveguide-coupled spectrum is further characterized by PL measurements on a reference device, discussed in the Appendix A.3.4. Thereby, the emitted PL has a varying interaction path length (absorption) with the monolayer WSe<sub>2</sub> before reaching the waveguide. The waveguide-coupled spectra show that an increase in interaction length leads 1) to a broadening of the peak at the red-side of the spectrum and 2) to a shift of the peak maximum towards longer wavelengths.

In summary, we observe differences in the spectral properties, when comparing the free-space EL and the waveguide-coupled EL. These differences manifest itself in a pronounced dip, in the  $EL_{WG}(\lambda)/EL_{LED}(\lambda)$ -curve. We verify with FDTD simulations and measurements on a bare h-BN waveguide, that in the given wavelength range the spectral influences by the waveguide and the tapering, even with rough sidewalls are expected to be minor. Furthermore, the simulations show that the collection of the in-plane guided mode at the end of the waveguide does not lead to a strong spectral dependence. We conclude that the spectral characteristics of the  $EL_{WG}(\lambda)/EL_{LED}(\lambda)$ -curve (Fig. 5.11b) coincide with the absorption characteristics of monolayer WSe<sub>2</sub>. This reinforces that the influence by the absorption of the sticking-out part of the monolayer can not be neglected.

Overall we have seen that the introduced platform enables an enhanced mode overlap between the confined modes and the integrated monolayers. Even though this mainly leads to the benefit of an improved coupling, it also introduces enhanced reabsorption by the monolayer itself. For the integrated LED these losses can be reduced by an improved alignment of the individual layers of the stack. This in turn should lead to an improved experimental coupling efficiency.

## 5.4 Conclusion

In summary, in this chapter, we show waveguide-coupled EL from vdW LEDs in an all 2D material-based on-chip photonics platform. We demonstrate the successful integration of exciton LEDs inside h-BN-based waveguide structures. Thereby, the electrically driven emitter is positioned near highest field intensities inside the light confining dielectrics. After having established in the last two chapters a promising platform for the integration of optically excited emitters, in this chapter we have now expanded this approach for electrically driven light sources. The experimentally determined coupling efficiency is close to the numerically expected value, confirming the reliability of the platform.



# 6

---

## Conclusions & Outlook

### 6.1 Conclusions

In this work we have experimentally implemented an on-chip photonics platform that enables waveguide integration of optically and electrically driven light sources. The presented devices are solely based on 2D materials, which enables us to achieve higher mode overlap by sandwiching emitters inside h-BN photonic structures.

For a first device structure in **chapter 3**, we integrate monolayer TMDs as emitters and couple their exciton PL to the WGMs of waveguide-coupled disk resonators. We verify the improved coupling, by the Q-factor of the resonator, which exhibits spectral dependence that can be attributed to the optical properties of the incorporated monolayer. The integration at higher field intensities leads to an increased absorption by the monolayer. This in turn decreases the Q-factor at the exciton transition and can lead to reabsorption of the cavity-coupled light by the monolayer itself.

To improve the device concept, in **chapter 4**, we integrate a HBL of

two dissimilar monolayers to couple the PL of the interlayer exciton to the WGMs of waveguide-coupled disk resonators. The interlayer transition has a weak oscillator strength and an emission energy that is smaller than the optical band gaps of the two individual monolayers. Therefore, the interlayer exciton emission is only weakly reabsorbed, which gives rise to a strong cavity-coupled interlayer emission and a higher Q-factor at the emission wavelength.

Furthermore, to demonstrate the integration of optoelectronic devices, in **chapter 5** we present a waveguide-integrated LED. Our waveguide-coupled LEDs are fabricated by embedding a TMD-based light-emitting vdW heterostructure inside thick layers of h-BN and subsequently patterning the whole stack. The encapsulated LEDs are contacted by Gr edge contacts. We observe waveguide-coupled exciton EL from the end of the waveguide.

## 6.2 Outlook

### 6.2.1 Device optimizations

#### **Design optimizations of the photonic structures**

For both device architectures, only first proof-of-concept devices were presented. Furthermore, the main focus was placed on optimizing the vertical emitter position. Therefore, in a next step, improved device performance can be achieved by optimizing the shape of the photonic structures. Such improvements can be adapted from research on photonics platforms from other material classes. For example, to improve the coupling efficiency of the waveguide-integrated LED, the lateral design of the LED area and the tapering geometry can be adapted [175, 176]. For the waveguide-coupled disk resonators, it is beneficial to further characterize and revise the waveguide width and distance to the disk [148]. Reduction of the propagation/radiation losses in the waveguides and the WGM resonators can for example be achieved by mode shaping with a corresponding waveguide design to reduce the overlap of the mode and the sidewall [180, 181]. Furthermore, for an improved waveguide in- and out-coupling, grating couplers could be added.



**Design optimizations for the output efficiency of the integrated LED**

One key figure of merit of integrated LEDs is the total output efficiency. More precisely, the external quantum efficiency of the LED and how efficient the emitted light can be further transmitted or used. As discussed in the last paragraph the therewith associated coupling efficiency can be increased by optimization of the lateral design of the photonic structures. Moreover, more light could be redirected to the waveguide mode by patterning the h-BN around and above the emitter region [182]. In addition, the quantum efficiency of the LED itself should be optimized. For PL measurements it has been shown that chemical treatment [183], electrostatic doping by gating [184] and strain [185] can lead to near unity PL quantum yields for monolayer TMDs. These considerations should also result in an improved internal quantum efficiency for LEDs with exciton emission based on monolayer TMDs. Compared to other monolayer TMD-based LEDs, the tunneling design that is discussed in section 1.5 and experimentally demonstrated in chapter 5 exhibits the highest external quantum efficiency [186]. Nevertheless, it might be further enhanced by band structure engineering and improvements of the LED design. One approach to improve the quantum efficiency is to increase the probability that the injected charge carriers form excitons. Potential ways to achieve this could be to optimize the barrier thicknesses and to use alternative barrier materials. More specifically, similar to organic LEDs [187], asymmetric barriers could be added to block preferably either only holes or only electrons.

**Fabrication optimizations**

Keeping in mind that patterning photonic structures out of vdW heterostructures and h-BN is yet in its infancy, additional advancements in performance can be expected through optimized fabrication techniques. An important step in this regard is the optimization of the etching process to achieve a low sidewall roughness to reduce the scattering losses of the photonic structures. This can lower the propagation losses of the waveguides and increase the Q-factors of the resonators. In this thesis two different etching masks were used: 1) Al and 2) PMMA. However, neither of the two masks is optimal. 1) The edges of the patterned Al after lift-off are very rough. This roughness is then transferred during the etching step onto the h-BN. 2) PMMA on the other

side is smoother but gets attacked during the etching process, which might lead to an inhomogeneous etching and consequently a rough sidewall. To address this, we have begun to explore other techniques, including the NanoFrazor [70], using focused ion beam (FIB) [188] for sidewall polishing, and experimenting with more etch-resistant resists. Not all of these approaches are dead ends; further research and optimization could be beneficial for reducing scattering losses. In the Appendix A.2.4 more details about the difficulties, observations and suggestions for the continuation are discussed.

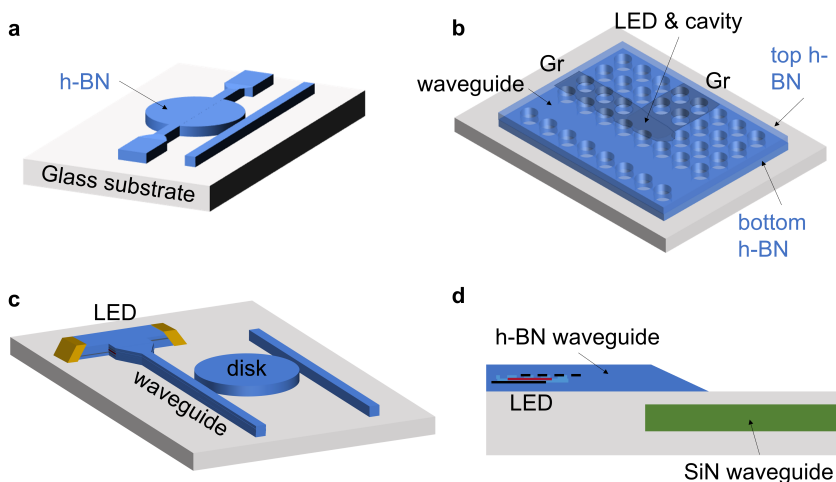


**Figure 6.1:** (a) h-BN waveguide-coupled disk resonator with fins that could enable a contacting of an LED integrated inside the disk. (b) h-BN photonic crystal cavity with integrated LED. To contact the two Gr electrodes, the shape of the cavity and waveguide does not have to be changed. (c) Waveguide-integrated LED coupled to an h-BN disk resonator. (d) Side view of a waveguide-integrated LED, coupled to a buried SiN waveguide. The mode coupler between the two is just schematically illustrated.

## 6.2.2 Expansion of the vdW on-chip photonics platform

All devices presented in this thesis are waveguide-coupled to enable integration with other on-chip photonic circuits. While in our work we focus on first prototype devices, this platform provides a versatile building block which

can be further advanced by integrating different vdW-based optoelectronic devices. In this section, we elaborate on different possibilities how to expand this platform and what requirements should be considered.

### **Integration of LEDs with waveguide-coupled h-BN cavities**

As a first continuation of the project, the combination of the two structures is envisionable. Our platform could enable the integration of electrically driven light sources with waveguide-coupled cavities made of h-BN. A difficulty here is the contacting of the integrated LED inside the disk resonator. One possibility is to use Gr as electrodes and to pattern narrow contact fins at the side of the disk, as illustrated in Fig. 6.1a. In a preliminary test, we have tried to investigate the influence of the integrated Gr and the fins on the Q-factor of the disk. The results are discussed in the Appendix A.2.4 and let us conclude that there is a decrease in Q-factor. One reason is that the mode inside the disk resonator is confined at the outer rim where the fins are positioned. Contacting at the lateral center of the disk should therefore reduce the introduced losses. This approach, however, would require more advanced fabrication procedures, for example as proposed in Ref. [67]. Another strategy is the integration of an LED inside a different kind of h-BN cavity, for example photonic crystal cavities. Also for these cavities, the LED can be integrated inside the vertical center at high field intensities. And most importantly, the designs of such cavities would facilitate the contacting of the LED with Gr layers (see Fig. 6.1b). First trials on the fabrication of h-BN photonic crystal structures have been made [68], also in our group [189]\*.

Another approach of how to combine the two devices presented in this thesis is to add an h-BN disk next to the waveguide of the integrated LED (Fig. 6.1c). In this way, the LED is not integrated into the disk, which facilitates contacting, but spectral filtering to narrow the LED emission can still be achieved.

---

\*This work has been realized in a supervised master thesis.

### **Integration of other light sources**

During the last years, a broad variety of LEDs based on 2D materials have been developed. For example LEDs with electrical control of single photon emitters [45] and fast modulation speed (MHz range for TMDs [43, 44], GHz for Gr [88]) have been demonstrated. All these LEDs could be combined with the presented platform to allow efficient integration with PICs and promote for example development towards quantum photonic chips.

Overall throughout this thesis, we have observed that the positioning of the monolayer TMDs inside the photonic structures at high field intensities leads to reabsorption. For integration inside cavities it would therefore be beneficial to integrate interlayer exciton LEDs with an electrically driven emission below the optical band gap of the two individual monolayers [57, 129, 134]. Furthermore, the recent progress in electrical control and emission energy tuning of interlayer excitons [57] further expands the spectrum of possibilities for electrically driven light sources with HBLs.

### **Integration of photodetectors and modulators**

One important property of on-chip integrated photodetectors is the bandwidth. For a vdW device with multilayer MoTe<sub>2</sub> as absorber, the carrier transit time has been reduced, which resulted in a bandwidth close to 50 GHz [24]. Important for the high bandwidth was thereby the vertical device geometry with a thin multilayer MoTe<sub>2</sub> and a small active device area [89]. In addition to bandwidth, however, photoresponsivity and the associated external quantum efficiency are also important figures of merit. By integrating such a photodetector inside the dielectric, the field confined inside the absorption medium could be enhanced drastically. This would lead to an improved device responsivity for thin devices without the need for a larger active area.

TMDs are also promising for optical modulators, as their optical properties can be modified by electrostatic doping [190]. When integrating the monolayer TMDs for modulation inside the dielectric at high field intensities, the interaction length and therefore the device size, could be reduced. However, a problem when integrating the TMDs inside the dielectric is the high absorption

at the exciton transition, which introduces losses. Recently, it has been demonstrated that monolayer TMDs also show a strong electrorefractive response in the transparency window of the monolayer (in the near-IR wavelengths) [29]. Integrating such a modulator at high field intensities would therefore benefit from improved light-matter interactions without the disadvantage of high absorption losses.

### **Using novel layered materials from the 2D family**

Overall, there are hundreds of other layered materials which can potentially be exfoliated [191]. This expands the potential of the platform to a new level. Especially because the presented platform also enables the usage of 2D materials that are air sensitive. This is due to the fact that the surrounding h-BN can act not only as a light-confining medium but also as a protective encapsulation layer.

### **Further expansion towards the IR range**

Throughout this thesis, we focus on devices that emit in the visible to near IR window. This platform can be expanded further towards the IR, for example by the integration of interlayer exciton emission from MoS<sub>2</sub>/WSe<sub>2</sub> (~ 1340 nm) [60]. Furthermore, photodetectors with multilayer MoTe<sub>2</sub> that operate at the standard O-band wavelength range (1260 – 1360 nm) could be integrated [24, 152]. In this spectral range, instead of h-BN other bulk 2D materials could be used as light confining layers [192, 193]. The bulk band gaps of MoSe<sub>2</sub>, WSe<sub>2</sub>, MoS<sub>2</sub> and WS<sub>2</sub> are in the range of 1.09 – 1.35 eV (~ 918 – 1137 nm) [58] and could therefore transmit and confine light in the wavelength range of the O- and C-band (~ 1530 – 1565 nm). Here, one advantage is the high refractive index of TMDs, which is increasing the confinement inside the photonic structure. The usage of bulk TMDs might even enable the possibility of charge carrier injection through the light-confining medium [194, 195].

### **2D PICs and co-integration with silicon photonics**

With the latest accomplishments in wafer-scale CVD-grown 2D materials [77, 196], the demonstrated prototype platform can be extended into larger photonic

circuits with integrated vdW optoelectronic devices. Furthermore, vdW-based photonic circuits with high mode overlap and increased light-matter interaction could be integrated with the well-established Si photonics platform. A coupling could for example be achieved by placing the h-BN waveguide-coupled vdW-heterostructures on top of buried SiN waveguides. This is schematically illustrated in Fig. 6.1d, but the mode coupler between the two waveguides is just indicating the idea and would need optimizations for improved coupling [197, 198].



---

## Appendix

\*

### A.1 Methods

#### A.1.1 Fabrication

##### A.1.1.1 Stacking of van der Waals hetrostructures

**M**onolayer MoS<sub>2</sub>, MoSe<sub>2</sub>, WSe<sub>2</sub> and Gr, as well as multilayer h-BN flakes were mechanically exfoliated on top of Si/SiO<sub>2</sub> substrates. An optical microscope was used to identify suitable flakes and AFM scans allowed

---

\*This Appendix is in parts adapted from the articles and the corresponding Supporting Information of the following two publications:

R. Khelifa, P. Back, N. Flöry, S. Nashashibi, K. Malchow, T. Taniguchi, K. Watanabe, and L. Novotny. *Coupling Interlayer Excitons to Whispering Gallery Modes in van der Waals Heterostructures*, *Nano Letters*, **20**, 6155-6161 (2020). Adapted with permission from [73]. Copyright 2020 American Chemical Society.

And Ref. [110]: R. Khelifa<sup>†</sup>, S. Shan<sup>†</sup>, A. J. Moilanen, T. Taniguchi, K. Watanabe, and L. Novotny. *WSe<sub>2</sub> Light-Emitting Device Coupled to an h-BN Waveguide*, *ACS Photonics*, **10**, 1328-1333 (2023), CC BY 4.0.

<sup>†</sup> These two authors contributed equally.

the exact determination of the flake thicknesses. The heterostructures were stacked under ambient or inert Ar atmosphere, using a polydimethylsiloxane (PDMS) stamp, covered with a polycarbonate (PC) film [162, 163]. The desired stack was picked up onto the PDMS/PC stamp. Finally, the stack was transferred onto the glass by melting the PC film, which detaches at high temperatures from the PDMS stamp and sticks to the glass. After the transfer, the PC film was dissolved in chloroform at room temperature.

### **Notes on devices in chapter 3:**

The vdW stack with sandwiched MoS<sub>2</sub> (device 1) was stacked with a straight (not curved) stamp in ambient conditions. The transferred stack was then annealed in a quartz tube furnace in Ar (95 %) and H<sub>2</sub> (5 %) atmosphere for 3 hours at 200°. For device 2, a monolayer MoS<sub>2</sub> was exfoliated directly on PDMS and transferred without a PC film on top of the prefabricated h-BN disk resonator (according to the procedure described in Ref. [199]).

### **Notes on devices in chapter 4:**

The vdW heterostructure was stacked using a curved PDMS stamp covered with a PC film in an inert Ar atmosphere (glovebox). Care was taken to rotationally align the MoSe<sub>2</sub> and WSe<sub>2</sub> monolayers.

### **Notes on devices in chapter 5:**

Also this stack was assembled using a curved PDMS stamp covered with a PC film in a glovebox filled with Ar gas. In order to see the Gr through the flakes during stacking and for better alignment, a thin top h-BN, ~5 nm was picked up as the first layer. In the following steps, this thin top h-BN was used to pick up a top Gr, a tunneling h-BN, a monolayer WSe<sub>2</sub>, a second tunneling h-BN, a bottom Gr and a bottom thick h-BN (~105 nm) sequentially. This stack then was transferred onto a glass coverslip. Finally, a thick h-BN flake (130 nm – 135 nm) was picked up with a new PC film. This thick h-BN was used as the top layer to pick up the previous stack. The final stack, consisting of the LED encapsulated in between thick h-BNs, was transferred onto a glass substrate. We have observed that when stacking clean layers, individual flakes shift with respect to each other. This can be prevented by aligning each flake



such that part of it sticks out of the topmost flake and touches the PC film.

### **A.1.1.2 Etching of the van der Waals stack**

#### **Etching of the waveguide-coupled disk resonators**

The structures were defined by means of electron-beam lithography using PMMA. The positioning and dimensions of the disk resonators were adapted to the shape of the individual flakes and the overall stack thickness. To prevent charging, an electrically conductive polymer, Espacer 300z was spin-coated over the PMMA. Following the removal of the Espacer and the development of the PMMA resist, 50 nm Al was evaporated to serve as a hard mask. RIE with SF<sub>6</sub> and Ar was used to etch the stack. As a starting point for the etching we used parameters from [151]. The etching was performed in short time steps with a total time that depended on the stack thickness. For the presented heterostructure in chapter 4 with integrated HBL, the total etch time was adjusted to 40 sec. The Al mask was removed with a tetramethylammonium hydroxide based solution. The etching angle is estimated to be in the range of 50°C – 60°C.

Details of the recipe for the waveguide-coupled disks in chapter 2, 3 and 4:

- spin-coating
  - take Espacer 300z out of the fridge
  - PMMA 50K pure in CB: spin-coating parameters: 5 sec to 5000 rpm, 45 sec to 5000 rpm, bake at 180 °C for 240 sec on the hotplate
  - PMMA 950K pure in Anisole: spin-coating parameters: 5 sec to 5000 rpm, 45 sec to 5000 rpm, bake at 180 °C for 240 sec on the hotplate
  - Espacer 300z: spin-coating parameters: 3 sec to 3000 rpm, 30 sec to 3000 rpm, bake at 110 °C for 300 sec on the hotplate

- EBL
  - Raith 150TWO
  - 30 kV
  - aperture: 10  $\mu\text{m}$
  - dose: 390  $\mu\text{As}/\text{cm}^2$
  - smallest step size
- development
  - to remove Spacer: 1 min in de-ionized (DI)-water
  - 60 sec in Methylisobutylketon(MIBK):isopropanol(IPA) 1:3
  - 60 sec in IPA
- metal evaporation and lift off
  - no  $\text{O}_2$  Asher
  - evaporate 50 nm Al (PLASSYS I (MEB550S) in FIRST cleanroom)
  - lift-off in Acetone on hot plate ( $\sim 65^\circ\text{C}$ ), in vertical sample holder, for 30 – 60 min, blow with pipette, very gently, no air
- Etching
  - RIE 80 Insulators (Oxford Instruments)
  - $\text{SF}_6$  and Ar (20 sccm:20 sccm)
  - RF power of 95 W
  - chamber pressure of 100 mTorr
  - Before the etching, 1 min of conditioning run
  - etch in steps of 5 sec
- Mask removal
  - remove Al mask for 30 min in ma-D 533 from micro resist
  - rinse for 5 min in DI-water

Note this recipe sometimes led to small cracks in the PMMA after development. These were then transferred into the Al and consequently led to irregularities in the patterned stack. The recipe was therefore adjusted and the development was performed with freezing cold IPA:H<sub>2</sub>O (3:1, weight ratio) for 1 min and 30 sec, ending it with 1 min in IPA at room temperature. Furthermore, it is recommended to exchange the recipe to a recipe with PMMA in anisole, 50K, diluted 1:1, and PMMA in anisole, 950 K, undiluted, with the following starting parameters: spin-coating of both resists with 40 sec to 4000 rpm, bake at 160 °C for 300 sec on the hotplate. Expose with a dose in the range of  $\sim 300 - 400 \mu\text{As}/\text{cm}^2$ .

### **Etching of the integrated LED**

For the etching of the LED structures, the etch mask was changed to PMMA and proximity corrections were performed. The recipe for the mask patterning was adjusted by Shengyu Shan in her master thesis [189] and the steps were also executed by her, therefore they are not introduced as detailed. By measuring the EL of the device after contacting, the position of the overlap region was confirmed and the waveguide structure was designed accordingly. A layer of 450 nm-thick 950K PMMA was spin-coated as EBL resist followed by a layer of Spacer. The designed pattern was exposed under 30 kV at a dose of  $400 \mu\text{A}/\text{cm}^2$  after proximity effect correction. The Spacer was removed in DI-water within 2 min. The sample was developed for 90 s in a cold mixture of IPA and DI water with a weight ratio of 3:1. The stack was etched in steps with RIE (SF<sub>6</sub> and Ar (20 sccm: 20 sccm), 95 W and 100 mTorr). The cross-linked PMMA at the surface was removed by RIE with O<sub>2</sub> (20 sccm, 60 W and 40 mTorr). Then the rest of the PMMA was removed in warm Acetone (40 min). Note that the PMMA mask gets attacked during etching. For the waveguide devices in chapter 2 and 5 this led to the fact that the final waveguide width is narrower than originally defined (with EBL). This has to be taken into account.

### **Etching in steps**

The biggest difficulty when etching vdW stacks was the movement of the remaining flakes during etching. In Fig. A.1a, an optical microscope image with

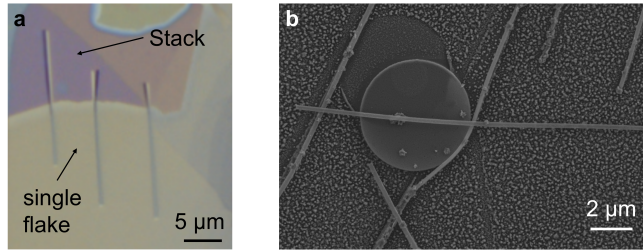


**Figure A.1:** (a) Optical microscope image of a stack with Al mask before etching, overlaid with the color inverted image after etching (without breaks). At the region of the stack, the flakes and the etch mask moved. (b) SEM image of a sample after etching (without breaks) with Al etch mask. The patterned mask and (partially etched) flakes moved.

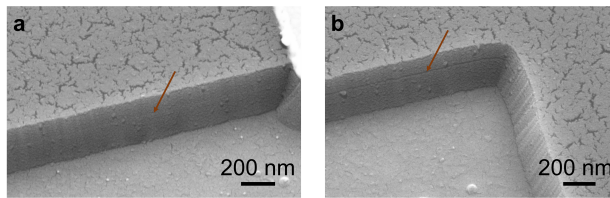


**Figure A.2:** SEM images of an h-BN – Gr – h-BN vdW heterostructure after etching. The arrows indicate the interface of the two h-BN flakes, thus the position of the integrated Gr. The interface in (a) is not as clear as the interface at a different location shown in (b). The reason could be defects, contamination or folds/bubbles that lead to a less smooth interface in (b).

etch mask (Al) from before etching is overlaid with a colour inverted image after etching. The etch mask on top of the stack and the flakes of the stack moved with respect to each other. Even more clearly this effect can be seen in the SEM image in Fig. A.1b. To understand the reason for this, we varied and adjusted several fabrication steps, such as, stacking without PC only with PDMS, align the flakes crystallographically, annealing of the stack, preheating before transfer, preetching of a bigger area, stacking in the glovebox. Finally, the problem was resolved by etching in short steps of 5 sec. After every etching step the chamber was vented and the sample was investigated under the optical microscope. Noteworthy is, that the movement of the stack during etching (in the RIE 80) did not occur for etching with a slower recipe with ( $\text{CHF}_3$  and  $\text{O}_2$

(40 sccm:4 sccm), 37.5 mTorr, 50 W). We suspect the reason for the movements to be either the heating up or the charging of the sample with a glass substrate. However, a further try with a 7 min purging step in between every etching step did not solve the problem. For the integrated LED projects the samples were then etched in steps of 2 times 5 sec and then investigated under the microscope.

In Figs. A.2 the SEM images of an h-BN – Gr – h-BN stack are shown. The arrows indicate the location of the monolayer Gr, sandwiched between the two h-BN flakes. In Fig. A.2a, the interface between the flakes is very smooth, whereas in Fig. A.2b the interface is more clearly visible. Contamination or bubbles between the flakes, and defects or folds within a flake could be the cause.

### A.1.1.3 Edge contacts

In the following, we discuss the fabrication of the edge contacts for the integrated LEDs (chapter 5). The position of the Gr flakes was identified by performing a reflection map. We contacted the encapsulated Gr flakes following the Gr edge contact recipe described in Refs. [162, 172]. EBL was used to define the pattern of the contacts. Here a bilayer of PMMA 50K 1:1 in anisole (40 sec 4000 rpm, baking 3 min at 160 °C) and PMMA 950K in pure anisole 450nm (40 sec 4000 rpm, baking 3 min at 160 °C) was used. The resist was exposed with 20 kV and a dose of 580  $\mu\text{As}/\text{cm}^2$  (aperture of 10  $\mu\text{m}$ ) and 450  $\mu\text{As}/\text{cm}^2$  (aperture of 120  $\mu\text{m}$ ) for the fine and the larger structures, respectively. Then the stack was etched by RIE (RIE NGP 80 Insulators, Oxford Instruments) with  $\text{CHF}_3$  and  $\text{O}_2$  (40 sccm:4 sccm, 60 W). Before the etching, 1 min of conditioning run was performed. The etching was executed in steps of 20 sec. The sample was not taken out after every step, only whenever the etch depth was checked with the optical microscope. For some contacts, again a slight movement of the metal relative to the etched trench was observed, indicating that a movement of the stack also in this recipe might be occurring. Therefore, further optimization of the recipe might be beneficial. The etch depth was determined by optical inspection of a reference h-BN flake with a thickness corresponding to the desired etch depth (on the same chip). After the etching,

10 nm Cr and 120 nm Au were evaporated as contact metals (PLASSYS II in FIRST clean room). For the device discussed in chapter 5, the etching depth was chosen around 150 nm, so that the Gr edges were exposed while the Au remained continuous at the etched step.

#### **A.1.1.4 General remarks and characterization techniques**

All devices were fabricated on glass slides with the following dimensions:  $22 \times 22 \times 0.13$  mm. Optical microscope images were acquired with a Nikon Eclipse LV100 and a Nikon Eclipse L200 optical microscope. For AFM scans we used a Bruker Innova. If not stated differently all SEM images were taken with a Zeiss ULTRA 55. To image the devices on glass substrates in the SEM, either the Al etch mask was still left on, Espacer was spin-coated or an additional thin layer of Platinum/Palladium was deposited on top.

#### **A.1.2 Measurement setup**

All measurements were performed in ambient conditions with a customized inverted Nikon TE300 microscope and an 100x oil immersion objective with an NA of 1.4 (Nikon). The samples were positioned on an x,y piezostage. An illustration of the measurement setup is shown in Fig. A.3.

#### **Photoluminescence (PL) measurements**

For the PL measurements we used a 532 nm or a 633 nm cw laser. The piezostage allowed the precise positioning of the incoming laser light onto the region of interest. The excitation power was measured to be  $\sim 47 \mu\text{W}$  for Fig. 4.4c and Fig. 4.5b and  $\sim 186 \mu\text{W}$  for Fig. 4.6b before the objective (633 nm). For the PL measurements in chapter 5 it was in the order of  $1 \mu\text{W}$  (532 nm). The emitted light was collected with the same objective from the entire structure. By scanning the piezostage, we obtained reflection maps with an Avalanche photodetector (APD). To record the PL signal, in addition, a 532 nm or 633 nm long pass filter was used to block the laser source. A Princeton Instruments Acton SpectraPro 300i spectrometer and a 300 grooves per mm grating were utilized for spatially resolved spectral measurements of the devices discussed in chapter 3 and 4. For the measurements in chapter 5, the

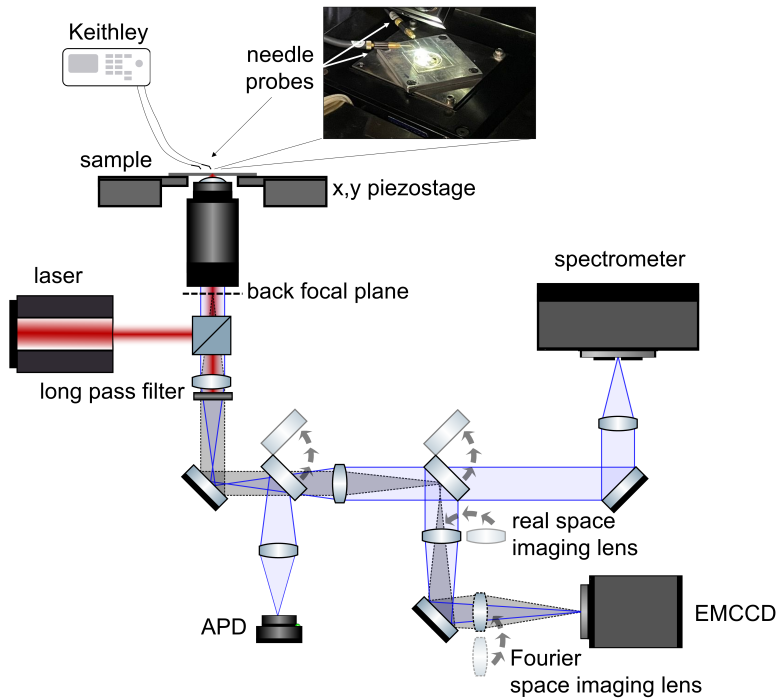


**Figure A.3:** Illustration of the optoelectronic measurement setup, adapted from Ref. [160].

PL spectra were acquired with a Princeton Instruments SpectraPro HRS-300 spectrometer with a BLAZE 400-HRX camera and a 150 grooves per mm grating. The entrance slit width of the spectrometer was used to spatially limit the detection area. After dispersion by the grating, each row of the spectrometer CCD recorded a spectrum corresponding to a specific position along the slit. Imaging different parts of the device, i.e. excitation spot or waveguide facet, on the spectrometer opening allowed us to differentiate and compare spectra of individual regions.

### Broadband excitation

For the transmission measurements, a fiber-coupled broadband supercontinuum source (NKT SuperK EXTREME) was used. The light was focused on one waveguide end and detected at the other waveguide end. For excitation

and detection the same objective was used. The excitation was spatially blocked.

### **Electroluminescence (EL) measurements**

For the EL measurements, the bias voltage was provided by a Keithley 2602B source meter unit. The gold pads on the sample were contacted with probe needles, as shown in Fig.A.3. To prevent electrostatic discharge over the device, during contacting and alignment, an ionizing fan was used. The emitted light was detected with the same objective as used for the other optical measurements. For real space imaging, an Andor iXon Ultra electron-multiplying charge-coupled device (EMCCD) camera was utilized. For spectral imaging, the same spectrometer as for PL imaging was used. If necessary, an additional aperture at the back focal plane of the objective was inserted to additionally block the light from a specific region.

### **Fourier space imaging**

For Fourier space imaging, the back focal plane of the objective is imaged onto the same EMCCD camera used for real space imaging. The optical path for Fourier space imaging is shown in Fig. A.3 in black.

### **Background and transmission corrections**

For all PL and EL measurements, background spectra were detected and subtracted from all measurements. Because for the device in chapter 5, the scattering at the edge of the LED region is very strong, additional background corrections (with rows around the waveguide end) were performed and measurements with spatially blocked LED emission were conducted. In a Si CCD camera, the detection efficiency for longer wavelengths is strongly reduced. To take this into account, we corrected all measurements (except broadband transmission measurements) to the transmission of the setup and the detection efficiency of the CCD camera.



### A.1.3 Numerical Simulations

#### A.1.3.1 Disk resonators

2D simulations of the disk resonator without coupled waveguide were executed using the Wave Optics module of COMSOL multiphysics. For the simulations the refractive index of h-BN was defined as constant over the considered wavelength range and was defined as:  $n_{\parallel} = 2.12$ ,  $\kappa_{\parallel} = 0.000048$ ,  $n_{\perp} = 1.83$ ,  $\kappa_{\perp} = 0.000043$ . The values for  $\kappa$  were taken from Ref. [107], whereas for  $n$ , we used values from Ref. [93] as an orientation. The h-BN disk was simulated on top of a glass substrate ( $n = 1.52$ ) and surrounded by air ( $n = 1$ ).

#### A.1.3.2 Waveguides

For the numerical simulations of the integrated LED, the FDTD solver of Lumerical Inc. was used. All simulations were executed in 3D. The mesh accuracy was commonly chosen to be 4. Mode sources and dipole sources were used for the excitation. The dipole sources are coherent, which is why in our simulations we only integrated one dipole source at once. Furthermore, due to the Purcell factor, the emission power of the dipole source depends on the surrounding environment. For simulations of the coupling efficiency, corresponding corrections had to be taken into account. To determine the coupling efficiency to specific waveguide modes, mode expansion monitor simulations were performed. For the simulations of the sidewall roughness, the structure group rough waveguide was used. To determine the angular distribution at the end of the waveguide, far field projections in FDTD were utilized. To minimize errors due to field truncation at the edge of the monitor, the far field data was spatially filtered to remove higher frequency noise. For all Lumerical simulations the absorption by h-BN was neglected. The refractive index of h-BN was defined as:  $n_{\parallel} = 2.12$ ,  $n_{\perp} = 1.84$  [93]. To understand if the dispersion of  $n$  has an influence on the spectral characteristics of the waveguide-coupled EL, discussed in subsection 5.3.5, we performed trial simulations including the material dispersion. However, the observed effect was minor.

## A.2 SI: disk resonators

### A.2.1 Sandwiched MoS<sub>2</sub> disk with signatures of the B-exciton

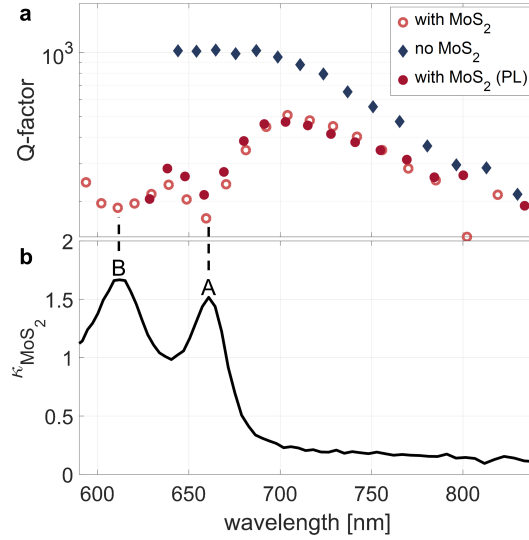


**Figure A.4:** (a) Q-factors of a waveguide-coupled disk resonator with sandwiched MoS<sub>2</sub> monolayer. The Q-factors drawn as filled red circles are extracted from PL measurements. The Q-factors drawn as empty orange circles are for the same device but extracted from measurements with a broadband source, coupled in at one waveguide end and detected at the other. Two dips in Q-factor can be resolved. These spectrally overlap with the A- and B-exciton absorption peaks of the monolayer MoS<sub>2</sub>. For comparison the Q-factors of an h-BN disk without incorporated monolayer are plotted (blue diamonds). There is no drop in Q-factors observable at wavelengths corresponding to the exciton transition of the monolayer. (b) Extinction coefficient of a monolayer MoS<sub>2</sub> taken from Ref. [111].

In the following, we discuss another waveguide-coupled disk resonator with embedded monolayer MoS<sub>2</sub>. The monolayer is sandwiched between a 122 nm thick bottom h-BN and a 100 nm thick top h-BN. The designed disk radius is 3  $\mu\text{m}$  and the designed waveguide top width is 200 nm. Also for this device, a coupling of the monolayer PL to the WGMs can be observed. The wavelength-dependent Q-factors are plotted in Fig. A.4a. The full red circles and the empty orange circles are Q factors extracted from PL measurements and from

measurements with a broadband source, respectively. The broadband source was coupled in at one waveguide end and detected at the other. This allows the determination of Q-factors for a broader wavelength range. Interestingly, the Q-factor exhibits two minima, which coincide with the spectral positions of the A- and B-exciton transitions of the monolayer MoS<sub>2</sub>. The A- and B-exciton transitions are visible in the extinction coefficient,  $\kappa_{\text{MoS}_2}$  [111], which is plotted as a function of wavelength in Fig. A.4b.

In addition to the devices with incorporated monolayer, a waveguide-coupled disk resonator with identical device geometry that consists of the same top and bottom h-BN but without integrated monolayer h-BN is fabricated (device discussed in subsection 2.2.2). In Fig. A.4a, the Q-factors (blue diamonds) are plotted as a function of wavelength. The overall Q-factor is higher and there is no strong drop observable for wavelengths that coincide with the exciton transition of the incorporated monolayer MoS<sub>2</sub>. This verifies again that the spectral characteristics of the sandwiched structures in this wavelength range are governed by the optical properties of the incorporated monolayer. However, for long wavelengths, a strong drop of Q-factor is observable for the bare h-BN disk and the sandwiched structure. As mentioned in subsection 2.2.2, this might be explained by the increasing radiation losses.

### A.2.2 Determination of Q-factor

To determine the wavelength-dependent Q-factor, each resonance of the measured spectra was fitted individually with Lorentzian functions and a linear background. The Q-factor was determined by approximating equation 2.2 to be

$$Q = \frac{\omega_0}{\Delta\omega} \approx \frac{\lambda_0}{\Delta\lambda}, \quad (\text{A.1})$$

with the center wavelength of the resonance  $\lambda_0$  and half the width of the resonance  $\Delta\lambda$  [143]. Here, this assumption introduces a negligible error. To minimize the influence of the background, in Fig. 4.7, we calculated the mean value and the standard deviation for each fitted Q-factor for different excitation positions (at both waveguide ends, on the monolayer region and on the interlayer

region), as well as for detection at both waveguide ends separately. In addition, we also considered the fitted Q-factors for a grating with 600 grooves per mm and a smaller slit opening, with a better resolution, but in return a reduced intensity.

### A.2.3 Purcell factor

To further characterize the h-BN disk resonators, in the following we estimate the corresponding Purcell factor of the device discussed in chapter 4. We estimate the enhancement by a cavity with a radius of  $4.25\ \mu\text{m}$  and a height of  $310\ \text{nm}$  for the resonance wavelength closest to  $920\ \text{nm}$ . We determine the effective mode volume from numerical simulations [200], whereas for the Q-factor we use a value of 570, which was determined from measurements. According to equation 2.6, the estimated enhancement then comes out to be  $\sim 3$ . Due to the relatively high effective mode volume and the modest Q-factor of the disk resonator in our case, the enhancement is not very strong. In principle, a higher Purcell enhancement can for example be achieved by designing an optical cavity with a smaller effective mode volume.

### A.2.4 Fabrication pretests

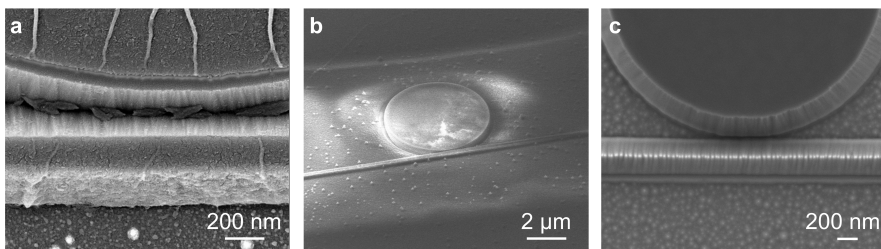


**Figure A.5:** SEM images of h-BN waveguide-coupled disk resonators: (a) after patterning with AR-N 7520.18 as etch mask, (b) after sidewall polishing with a FIB, (c) after patterning with the NanoFrazor.

#### Pretests to reduce the sidewall roughness

In order to optimize the sidewall roughness, different pretests were performed. First, the negative resist AR-N 7520.18 was used as a new etch mask. It was

observed that the resist is very sensitive to the exposure dose. But from visual inspection, the sidewall roughness seemed to have improved, as visible in the SEM image in Fig. A.5a. However, no drastic improvement in the Q-factor could be determined from measurements on h-BN disks. We assume that the reason is the residues that remain after stripping (AR 300-76 heated to 80 °C for 30 min), which are visible in the SEM image in Fig. A.5a. A solution might be the removal of the cross-linked resist with a short O<sub>2</sub> plasma step before chemical stripping.

Another approach to improve the sidewall roughness was the polishing of the sidewall with a Gallium FIB.\* Before the polishing, the samples were spin-coated with Espacer. Only the sidewall of the disk resonator was polished, and as can be seen in the SEM image in Fig. A.5b, the sidewall angle became very steep. The alignment was very difficult, which is why the coupling area between the waveguide and the disk was not polished. Measurements showed that the Q-factor after polishing decreased. Furthermore, for a device with integrated monolayer MoS<sub>2</sub>, no more PL signal was detectable after polishing. Reasons for this might be ion implantation. A way to reduce this might be achieved by annealing the sample or by the usage of a different FIB.

Furthermore, we tried the usage of thermal scanning-probe lithography with a NanoFrazor Explore (SwissLitho) combined with RIE to pattern waveguide-coupled disk resonators [70].† This is a comparably new method to pattern materials, which has the benefit to enable the patterning of freeform landscapes. In the first try, the patterning of h-BN flakes placed on top of a glass substrate did not work. Here, the sample was not coated with Espacer. Whether coating with a conductive polymer could potentially allow h-BN to be processed on glass requires further investigation. However, on a Si chip with 285 nm SiO<sub>2</sub> layer, the patterning was possible. The result is shown in the SEM image in Fig. A.5c. Very small sidewall angles can be observed. These

---

\*These pretests have been performed with the help of Joakim Reuteler at ScopeM at ETH Zurich. The SEM image was taken with a Helios 600i.

†The patterning has been performed by Nolan Lassaline at the Binnig and Rohrer Nanotechnology Center (BRNC).

are defined by the tip of the NanoFrazor. Therefore, the design of the disk resonator would need to be adapted for a successful implementation.

### Towards contacting inside disk resonators

In order to integrate a vdW LED inside a disk resonator, electrical contacting has to be enabled. For a first trial, a reference stack with integrated monolayer Gr (top h-BN:  $\sim 155$  nm, bottom h-BN:  $\sim 140$  nm) was fabricated. As shown in the optical microscope image in Fig. A.6b, the stack was patterned into a waveguide-coupled disk resonator with integrated monolayer Gr with (right) and without (left) contact fins. For the disk without contact fins (Fig. A.6c), signatures of the WGM resonances can be observed in the transmission measurement that is shown in Fig. A.6a. The Q-factors are relatively constant and in a range of 200 – 300. To compare the device an identical device without Gr was patterned on the same stack. For short wavelengths, this device exhibits higher Q factors ( $\sim 500$ ), however, higher-order resonances that spectrally overlap, impede the determination of the correct Q-factors for longer wavelengths.

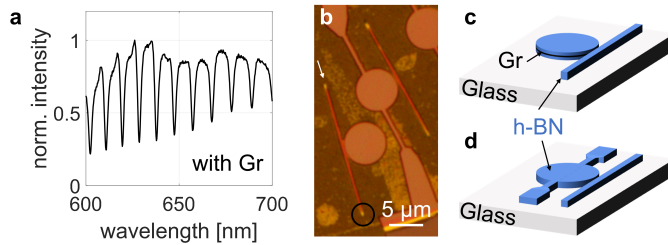


**Figure A.6:** (a) Transmission measurement of an h-BN disk resonator with integrated monolayer Gr without contact fins. (b) Optical microscope image of the disk resonator with integrated Gr without (left) and with (right) contact fins. (c) and (d) Schematic illustration of the two devices shown in (b).

When measuring the device with Gr and contact fins (Fig. A.6d), barely any signatures of WGM resonances were observed, indicating a strong drop in Q-factor. On another reference h-BN flake (thickness of  $\sim 115$  nm) in a shorter wavelength range (around 500 nm) bare h-BN disks with and without fins were

compared. Overall the Q-factor was higher and for the devices with fins, a decrease in Q-factor by a factor 2 – 3 was observed. In summary, this first pretest lets us conclude that, as expected, the integrated Gr introduces some losses but signatures of the WGM resonances are still observable. Using contact fins seems to decrease the Q-factor to a higher extent. However, the design of the contact fins was not optimized, reducing the width and the shape might improve the result.

### A.3 SI: waveguide-integrated LEDs

#### A.3.1 Waveguide-integrated LEDs

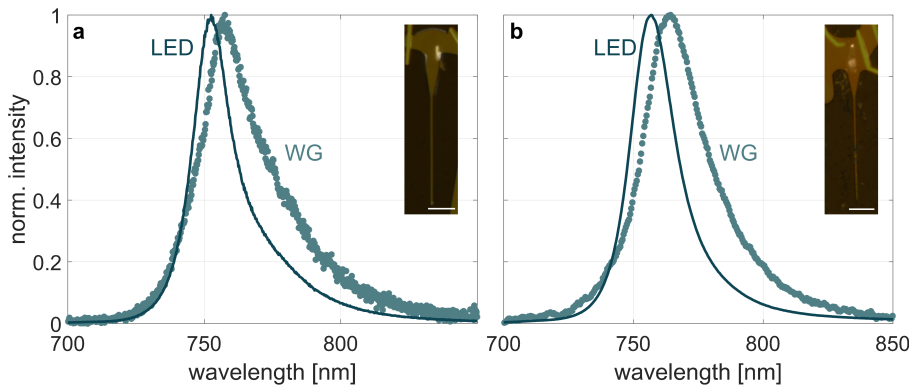


**Figure A.7:** (a) and (b) Waveguide (WG)-coupled EL (blue dotted line) plotted together with the free-space EL (blue solid line), for two other waveguide-integrated LEDs. For both the electrically driven exciton emission was successfully coupled to the waveguide. The insets show the microscope images of the corresponding device overlaid with the real space image of the integrated LED emission. The scale bar is 5 μm.

In Fig. A.7, two other waveguide-integrated LEDs are shown. For both devices, the waveguide-coupled and the free-space EL are plotted as a function of wavelength. In the inset, the optical microscope images are overlaid with the real-space EL images. Both devices verify that the etching did not harm the optoelectronic characteristics of the device. This further proves the reliability

of the demonstrated platform. Also here the peak of the waveguide-coupled EL is shifted towards longer wavelengths and the spectral characteristics of the  $EL_{WG}(\lambda)/EL_{LED}(\lambda)$ -curve also show a distinct peak close to the exciton transition. Due to alignment, for both devices, part of the monolayer WSe<sub>2</sub> is sticking out. Consequently, reabsorption by the sticking-out monolayer could also here be responsible for the spectral characteristics.

### A.3.2 Electrical characterization of the edge contacts

The contacting method of Gr edge contacts is a well-established approach for encapsulated structures. However, earlier studies have only contacted Gr flakes sandwiched between thin h-BN flakes with thicknesses in the range of tens of nanometers [162, 172]. Since, in our devices, the encapsulating h-BNs are much thicker, in the following we characterize the edge contacts to Gr when integrated inside thick stacks. For this reason, we discuss TLM measurements on an h-BN – Gr – h-BN reference stack. The total stack thickness is ~245 nm, whereby the Gr flake is integrated close to the vertical center. The fabrication of the edge contacts was performed as described in subsection A.1.1.3. For the TLM characterization, Gr channels with lengths varying from 1 to 5  $\mu\text{m}$  with a channel width of 2.2  $\mu\text{m}$  ( $\pm 0.2 \mu\text{m}$ ) were defined (see Fig. A.8a).

The total resistance for every channel can be described with

$$R_{tot} = 2R_{met} + 2R_C + R_{sheet} \frac{l_{channel}}{W}. \quad (\text{A.2})$$

$R_{met}$  is the metal resistance,  $R_C$  is the contact resistance between Cr/Au and Gr,  $R_{sheet}$  is the sheet resistance of the Gr channel,  $l_{channel}$  and  $W$  are the channel length and width, respectively. The total resistance of each channel is evaluated with I-V measurements and plotted in Fig A.8b. By a linear fit of the results (dashed line in Fig A.8b), the contact resistance can be determined, according to equation A.2. The contact resistivity  $\rho_C = R_C \cdot W$  can be extracted from the y-intercept. In our device the contact resistivity is  $258 \Omega\mu\text{m} \pm 23 \Omega\mu\text{m}$ , assuming a negligible metal resistance.

The assumption of a negligible metal resistance is correct for most devices [174].



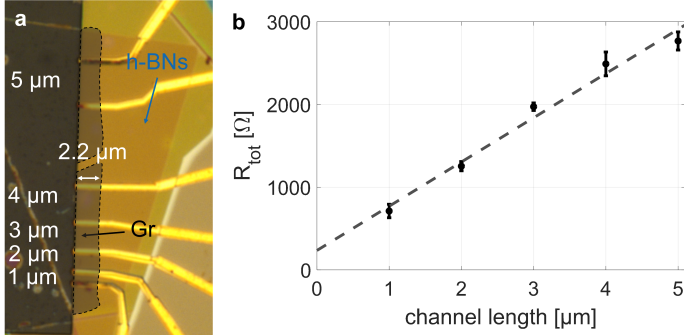


**Figure A.8:** (a) Optical microscope image of the reference stack for TLM measurements. The Gr sheet is indicated by the gray area. The channel lengths vary from 1 to 5 μm. The channel width is defined on one side by the edge of the Gr flake and on the other side by etching of the stack. (b) The total resistance of each channel, plotted together with a linear fit.

In our devices, however, the resistance by the metal seems to have a non-negligible contribution to the total resistance. We attribute this to two reasons, which both are visible in the SEM image in Fig. 5.3d: 1) the large step size from the remaining h-BN to the glass substrate and 2) the strong glass surface roughness after etching. To estimate the order of magnitude of the metal resistance, the overall resistance of a metal short  $2R_{met}$ , fabricated in the same way onto a 165 nm thick h-BN flake, is determined to be in the range of 50 – 100 Ω. Note that the length of the metal contact and the flake thickness (step height) are different compared to the reference stack and the integrated LED. Therefore, the metal resistance of the TLM device in Fig. A.8a is assumed to differ and we can only estimate the order of magnitude of  $R_{met}$ .

Overall, the TLM measurements help to estimate the contact resistance in our integrated LED structures. We conclude, that even when integrated inside thick h-BN flakes, the contact to the Gr electrodes is in a comparable order of magnitude as previously presented [162, 174].

### **A.3.3 Coupling efficiency**

#### **A.3.3.1 Corrections for the experimental coupling efficiency**

The free-space EL at the LED region is, as discussed in subsection 5.3.3, dominated by in-plane emitters oriented in the  $xy$ -plane. A big fraction is consequently expected to be emitted in out-of-plane direction. For dipole emitters, integrated inside thick h-BN slabs, the majority of emission is, however, guided in in-plane direction. Simulations for a single dipole, placed inside h-BN layers (top and bottom thickness as in the here presented device), show that for  $\lambda = 760\text{ nm}$  only  $\sim 16.5\%$  are emitted into the glass substrate and collected by our oil immersion objective with an NA of 1.4.

As discussed earlier in subsection 5.3.5 (collection efficiency), the waveguide-coupled EL, on the other hand, is an in-plane guided mode, out-coupled through scattering at the end facet of the waveguide. From integration over the simulated intensity, within the collection cone of our objective (cf. Fig. 5.10b), a collection efficiency of  $\sim 70\%$  is determined. Thereby a fundamental TE mode with  $\lambda = 760\text{ nm}$  was considered.

These correction factors were used to estimate the absolute value of the experimental coupling efficiency of the waveguide-integrated LED. Moreover, the correction for the LED region was also used to estimate the absolute value of the external quantum efficiency of the unpatterned LED.

#### **A.3.3.2 Simulated coupling efficiency**

Here, we present further simulations to discuss the numerically estimated coupling efficiency. The emitter was placed inside the h-BN structure at the same vertical position ( $z$ -axis) as the experimentally demonstrated LED. The determined coupling efficiency is representing the fraction of the dipole emission that is coupled into the fundamental TE mode of the waveguide. We focus more detailed on two factors that influence the coupling efficiency of the dipole emitters: 1) position ( $x$ - and  $y$ -direction) of the emitter within the LED emission region and 2) orientation angle within the  $xy$ -plane. When

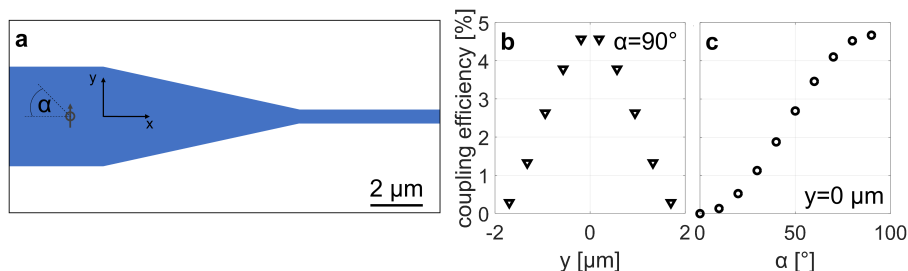


**Figure A.9:** (a) Sketch to illustrate the LED, tapering and waveguide as defined in the simulations. Simulated coupling efficiency when varying (b) the dipole position in  $y$ -direction and (c) the dipole orientation in the  $xy$ -plane.

sweeping the dipole in  $x$ -direction, only a small decrease is observed for an increased distance to the beginning of the tapering. When sweeping however the position of the dipole in  $y$ -direction (see Fig. A.9b), the coupling efficiency decreases from 4.7 % to 0.3 % ( $x$ -position and angle of the dipole were still kept as shown in Fig. A.9a). Similarly, when sweeping the angle  $\alpha$  of the dipole within the  $xy$ -plane (see Fig. A.9c), the coupling efficiency decreases to nearly 0 % for a dipole with an orientation along the  $x$ -axis ( $x$ - and  $y$ -position of the dipole as shown in Fig. A.9c). For the determined average, discussed in 5.1.2 (lateral design), the mean values of the individual sweeps were considered. It is therefore only a rough estimate.

### A.3.4 Waveguide-coupled PL measurements

To reaffirm the influence of absorption effects, PL measurements were performed on a reference device shown in Fig. A.10b. A single  $\text{WSe}_2$  monolayer is integrated close to the vertical center in between two thick  $\text{h-BN}$  flakes (top:  $\sim 130$  nm, bottom:  $\sim 110$  nm) and positioned close to the tapering. The emission at the waveguide end was detected while sweeping the excitation spot (532 nm cw laser) as indicated in Fig. A.10b. The longer the distance between the excitation spot and the tapering (lighter blue curves), the longer the interaction length of the emitted PL with the  $\text{WSe}_2$  layer before reaching the waveguide. This leads to a changed waveguide-coupled emission, plotted in Fig. A.10a. The spectra show that an increase in interaction length leads 1) to a

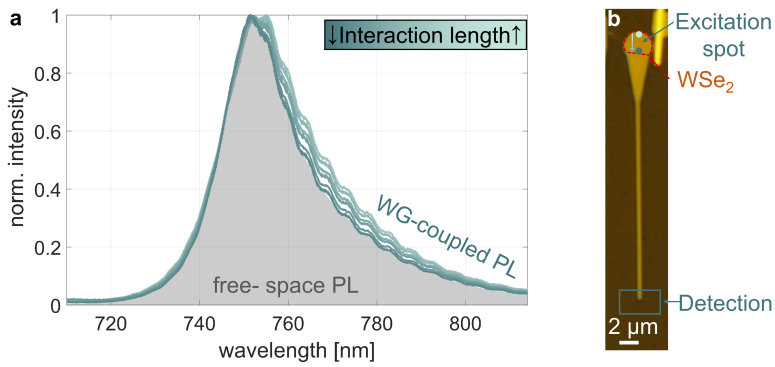


**Figure A.10:** (a) Waveguide-coupled PL measurements on the reference device shown in (b). The laser spot is swept on the monolayer changing the interaction length with the rest of the WSe<sub>2</sub> layer. With increased interaction length a larger shift towards higher wavelengths can be observed for the waveguide-coupled PL. (b) Optical microscope image of the reference device, indicating the excitation spot and the detection region.

broadening of the peak at the red-side of the spectrum and 2) to a shift of the peak maximum towards longer wavelengths. The spectrum of the free-space PL (gray area) coincides more with waveguide-coupled spectra with short interaction lengths and is consequently verifying that the spectral changes increase for longer interactions with the WSe<sub>2</sub> layer.

---

## References

- [1] Cisco public, *Cisco Visual Networking Index: Forecast and Trends, 2017-2022 White Paper*, 2019.
- [2] L. Schumann, T. V. Doan, T. Shreedhar, R. Mok, and V. Bajpai, *Impact of Evolving Protocols and COVID-19 on Internet Traffic Shares*, arXiv preprint , arXiv:2201.00142 (2022).
- [3] A. Andrae and T. Edler, *On Global Electricity Usage of Communication Technology: Trends to 2030*, *Challenges* **6**, 117 (2015).
- [4] N. Jones, *How to stop data centres from gobbling up the world's electricity*, *Nature* **561**, 163 (2018).
- [5] C. A. Thraskias, E. N. Lallas, N. Neumann, L. Schares, B. J. Offrein, R. Henker, D. Plettemeier, F. Ellinger, J. Leuthold, and I. Tomkos, *Survey of photonic and plasmonic interconnect technologies for intra-datacenter and high-performance computing communications*, *IEEE Communications Surveys and Tutorials* **20**, 2758 (2018).
- [6] Q. Cheng, M. Bahadori, M. Glick, S. Rumley, and K. Bergman, *Recent advances in optical technologies for data centers: a review*, *Optica* **5**, 1354 (2018).
- [7] X. Zhou, H. Liu, R. Urata, and S. Zebian, *Scaling large data center interconnects: Challenges and solutions*, *Optical Fiber Technology* **44**, 61 (2018).
- [8] M. A. Porcel, A. Hinojosa, H. Jans, A. Stassen, J. Goyvaerts, D. Geuzebroek, M. Geiselman, C. Dominguez, and I. Artundo, *Silicon nitride photonic integration for visible light applications*, *Optics and Laser Technology* **112**, 299 (2019).
- [9] A. Hänsel and M. J. Heck, *Opportunities for photonic integrated circuits in optical gas sensors*, *J. Phys. Photonics* **2**, 012002 (2020).
- [10] P. Dong, Y. K. Chen, G. H. Duan, and D. T. Neilson, *Silicon photonic devices and integrated circuits*, *Nanophotonics* **3**, 215 (2014).

## REFERENCES

---

- [11] M. Lipson, *The revolution of silicon photonics*, Nature Materials **21**, 974 (2022).
- [12] F. Gardes, A. Shoaib, G. De Paoli, I. Skandalos, S. Ilie, T. Rutirawut, W. Talataisong, J. Faneca, V. Vitali, Y. Hou, T. D. Bucio, I. Zeimpekis, C. Lacava, and P. Petropoulos, *A Review of Capabilities and Scope for Hybrid Integration Offered by Silicon-Nitride-Based Photonic Integrated Circuits*, Sensors **22**, 4227 (2022).
- [13] E. L. Wooten, K. M. Kissa, A. Yi-Yan, E. J. Murphy, D. A. Lafaw, P. F. Hallemeier, D. Maack, D. V. Attanasio, D. J. Fritz, G. J. McBrien, and D. E. Bossi, *Review of lithium niobate modulators for fiber-optic communications systems*, IEEE Journal of Selected Topics in Quantum Electronics **6**, 69 (2000).
- [14] D. A. Pohl, *Integrated Lithium Niobate Photonics for Spectrometry and Modulation*, PhD thesis, ETH Zürich, 2022.
- [15] D. Zhu, L. Shao, M. Yu, R. Cheng, B. Desiatov, C. J. Xin, Y. Hu, J. Holzgrafe, S. Ghosh, A. Shams-Ansari, E. Puma, N. Sinclair, C. Reimer, M. Zhang, and M. Lončar, *Integrated photonics on thin-film lithium niobate*, Advances in Optics and Photonics **13**, 242 (2021).
- [16] Y. Han, H. Park, J. Bowers, and K. M. Lau, *Recent advances in light sources on silicon*, Advances in Optics and Photonics **14**, 404 (2022).
- [17] T. Komljenovic, D. Huang, P. Pintus, M. A. Tran, M. L. Davenport, and J. E. Bowers, *Photonic Integrated Circuits Using Heterogeneous Integration on Silicon*, Proceedings of the IEEE **106**, 2246 (2018).
- [18] F. Xia, H. Wang, D. Xiao, M. Dubey, and A. Ramasubramaniam, *Two-dimensional material nanophotonics*, Nature Photonics **8**, 899 (2014).
- [19] Y. Q. Bie, G. Grosso, M. Heuck, M. M. Furchi, Y. Cao, J. Zheng, D. Bunandar, E. Navarro-Moratalla, L. Zhou, D. K. Efetov, T. Taniguchi, K. Watanabe, J. Kong, D. Englund, and P. Jarillo-Herrero, *A MoTe<sub>2</sub>-based light-emitting diode and photodetector for silicon photonic integrated circuits*, Nature Nanotechnology **12**, 1124 (2017).
- [20] K. Thakar and S. Lodha, *Optoelectronic and photonic devices based on transition metal dichalcogenides*, Materials Research Express **7**, 014002 (2020).
- [21] J. An, X. Zhao, Y. Zhang, M. Liu, J. Yuan, X. Sun, Z. Zhang, B. Wang, S. Li, and D. Li, *Perspectives of 2D Materials for Optoelectronic Integration*, Advanced Functional Materials **32**, 2110119 (2022).
- [22] D.-S. Liu, J. Wu, H. Xu, and Z. Wang, *Emerging Light-Emitting Materials for Photonic Integration*, Advanced Materials **33**, 2003733 (2021).
- [23] P. Ma, Y. Salamin, B. Baeuerle, A. Josten, W. Heni, A. Emboras, and J. Leuthold, *Plasmonically Enhanced Graphene Photodetector Featuring 100 Gbit/s Data Reception, High Responsivity, and Compact Size*, ACS Photonics **6**, 154 (2019).

- [24] N. Flöry, P. Ma, Y. Salamin, A. Emboras, T. Taniguchi, K. Watanabe, J. Leuthold, and L. Novotny, *Waveguide-integrated van der Waals heterostructure photodetector at telecom wavelengths with high speed and high responsivity*, Nature Nanotechnology **15**, 118 (2020).
- [25] R. J. Shiue, Y. Gao, Y. Wang, C. Peng, A. D. Robertson, D. K. Efetov, S. Assefa, F. H. Koppens, J. Hone, and D. Englund, *High-Responsivity Graphene-Boron Nitride Photodetector and Autocorrelator in a Silicon Photonic Integrated Circuit*, Nano Letters **15**, 7288 (2015).
- [26] W. Yu, S. Li, Y. Zhang, W. Ma, T. Sun, J. Yuan, K. Fu, and Q. Bao, *Near-Infrared Photodetectors Based on MoTe<sub>2</sub>/Graphene Heterostructure with High Responsivity and Flexibility*, Small **13**, 1700268 (2017).
- [27] Q. Ma, C. H. Lui, J. C. Song, Y. Lin, J. F. Kong, Y. Cao, T. H. Dinh, N. L. Nair, W. Fang, K. Watanabe, T. Taniguchi, S. Y. Xu, J. Kong, T. Palacios, N. Gedik, N. M. Gabor, and P. Jarillo-Herrero, *Giant intrinsic photoresponse in pristine graphene*, Nature Nanotechnology **14**, 145 (2019).
- [28] M. Liu, X. Yin, E. Ulin-Avila, B. Geng, T. Zentgraf, L. Ju, F. Wang, and X. Zhang, *A graphene-based broadband optical modulator*, Nature **474**, 64 (2011).
- [29] I. Datta, S. H. Chae, G. R. Bhatt, M. A. Tadayon, B. Li, Y. Yu, C. Park, J. Park, L. Cao, D. N. Basov, J. Hone, and M. Lipson, *Low-loss composite photonic platform based on 2D semiconductor monolayers*, Nature Photonics **14**, 256 (2020).
- [30] X. Yang, R. Wu, B. Zheng, Z. Luo, W. You, H. Liu, L. Li, Y. Zhang, Q. Tan, D. Liang, Y. Chen, J. Qu, X. Yi, X. Wang, J. Zhou, H. Duan, S. Wang, S. Chen, and A. Pan, *A Waveguide-Integrated Two-Dimensional Light-Emitting Diode Based on p-Type WSe<sub>2</sub>/n-Type CdS Nanoribbon Heterojunction*, ACS Nano **16**, 4371 (2022).
- [31] F. Li, J. Zheng, Q. Yao, and Y.-Q. Bie, *Recent progress of silicon integrated light emitters and photodetectors for optical communication based on two-dimensional materials*, Optical Materials Express **11**, 3298 (2021).
- [32] J. Wu, H. Ma, P. Yin, Y. Ge, Y. Zhang, L. Li, H. Zhang, and H. Lin, *Two-Dimensional Materials for Integrated Photonics: Recent Advances and Future Challenges*, Small Science **1**, 2000053 (2021).
- [33] A. K. Geim and I. V. Grigorieva, *Van der Waals heterostructures*, Nature **499**, 419 (2013).
- [34] Y. Liu, N. O. Weiss, X. Duan, H. C. Cheng, Y. Huang, and X. Duan, *Van der Waals heterostructures and devices*, Nature Reviews Materials **1**, 16042 (2016).
- [35] R. S. Sundaram, M. Engel, A. Lombardo, R. Krupke, A. C. Ferrari, P. Avouris,

## REFERENCES

---

- and M. Steiner, *Electroluminescence in Single Layer MoS<sub>2</sub>*, Nano Lett. **13**, 1416 (2013).
- [36] D.-H. Lien, M. Amani, S. B. Desai, G. H. Ahn, K. Han, J. H. He, J. W. Ager, M. C. Wu, and A. Javey, *Large-area and bright pulsed electroluminescence in monolayer semiconductors*, Nature Communications **9**, 1229 (2018).
- [37] F. Withers, O. Del Pozo-Zamudio, A. Mishchenko, A. P. Rooney, A. Gholinia, K. Watanabe, T. Taniguchi, S. J. Haigh, A. K. Geim, A. I. Tartakovskii, and K. S. Novoselov, *Light-emitting diodes by band-structure engineering in van der Waals heterostructures*, Nature Materials **14**, 301 (2015).
- [38] F. Withers, O. Del Pozo-Zamudio, S. Schwarz, S. Dufferwiel, P. M. Walker, T. Godde, A. P. Rooney, A. Gholinia, C. R. Woods, P. Blake, S. J. Haigh, K. Watanabe, T. Taniguchi, I. L. Aleiner, A. K. Geim, V. I. Fal'ko, A. I. Tartakovskii, and K. S. Novoselov, *WSe<sub>2</sub> Light-Emitting Tunneling Transistors with Enhanced Brightness at Room Temperature*, Nano Letters **15**, 8223 (2015).
- [39] A. Pospischil, M. M. Furchi, and T. Mueller, *Solar-energy conversion and light emission in an atomic monolayer p-n diode*, Nature Nanotechnology **9**, 257 (2014).
- [40] B. W. Baugher, H. O. Churchill, Y. Yang, and P. Jarillo-Herrero, *Optoelectronic devices based on electrically tunable p-n diodes in a monolayer dichalcogenide*, Nature Nanotechnology **9**, 262 (2014).
- [41] J. S. Ross, P. Klement, A. M. Jones, N. J. Ghimire, J. Yan, D. G. Mandrus, T. Taniguchi, K. Watanabe, K. Kitamura, W. Yao, D. H. Cobden, and X. Xu, *Electrically tunable excitonic light-emitting diodes based on monolayer WSe<sub>2</sub> p-n junctions*, Nature Nanotechnology **9**, 268 (2014).
- [42] A. Kuzmina, M. Parzefall, P. Back, T. Taniguchi, K. Watanabe, A. Jain, and L. Novotny, *Resonant Light Emission from Graphene/Hexagonal Boron Nitride/Graphene Tunnel Junctions*, Nano Letters **21**, 8332 (2021).
- [43] J. F. Gonzalez Marin, D. Unuchek, Z. Sun, C. Y. Cheon, F. Tagarelli, K. Watanabe, T. Taniguchi, and A. Kis, *Room-temperature electrical control of polarization and emission angle in a cavity-integrated 2D pulsed LED*, Nature Communications **13**, 4884 (2022).
- [44] C. H. Liu, G. Clark, T. Fryett, S. Wu, J. Zheng, F. Hatami, X. Xu, and A. Majumdar, *Nanocavity integrated van der Waals heterostructure light-emitting tunneling diode*, Nano Letters **17**, 200 (2017).
- [45] C. Palacios-Berraquero, M. Barbone, D. M. Kara, X. Chen, I. Goykhman, D. Yoon, A. K. Ott, J. Beitner, K. Watanabe, T. Taniguchi, A. C. Ferrari, and M. Atatüre, *Atomically thin quantum light-emitting diodes*, Nature Communications **7**, 12978 (2016).



- [46] K. F. Mak, C. Lee, J. Hone, J. Shan, and T. F. Heinz, *Atomically thin MoS<sub>2</sub> : A new direct-gap semiconductor*, Physical Review Letters **105**, 136805 (2010).
- [47] A. Splendiani, L. Sun, Y. Zhang, T. Li, J. Kim, C. Y. Chim, G. Galli, and F. Wang, *Emerging photoluminescence in monolayer MoS<sub>2</sub>*, Nano Letters **10**, 1271 (2010).
- [48] S. Wu, S. Buckley, J. R. Schaibley, L. Feng, J. Yan, D. G. Mandrus, F. Hatami, W. Yao, J. Vučković, A. Majumdar, and X. Xu, *Monolayer semiconductor nanocavity lasers with ultralow thresholds*, Nature **520**, 69 (2015).
- [49] Y. Ye, Z. J. Wong, X. Lu, X. Ni, H. Zhu, X. Chen, Y. Wang, and X. Zhang, *Monolayer excitonic laser*, Nature Photonics **9**, 733 (2015).
- [50] O. Salehzadeh, M. Djavid, N. H. Tran, I. Shih, and Z. Mi, *Optically Pumped Two-Dimensional MoS<sub>2</sub> Lasers Operating at Room-Temperature*, Nano Letters **15**, 5302 (2015).
- [51] J. C. Reed, S. C. Malek, F. Yi, C. H. Naylor, A. T. Charlie Johnson, and E. Cubukcu, *Photothermal characterization of MoS<sub>2</sub> emission coupled to a microdisk cavity*, Applied Physics Letters **109**, 193109 (2016).
- [52] Y. Li, J. Zhang, D. Huang, H. Sun, F. Fan, J. Feng, Z. Wang, and C. Z. Ning, *Room-temperature continuous-wave lasing from monolayer molybdenum ditelluride integrated with a silicon nanobeam cavity*, Nature Nanotechnology **12**, 987 (2017).
- [53] J. Shang, C. Cong, Z. Wang, N. Peimyoo, L. Wu, C. Zou, Y. Chen, X. Y. Chin, J. Wang, C. Soci, W. Huang, and T. Yu, *Room-temperature 2D semiconductor activated vertical-cavity surface-emitting lasers*, Nature Communications **8**, 543 (2017).
- [54] C. Javerzac-Galy, A. Kumar, R. D. Schilling, N. Piro, S. Khorasani, M. Barbone, I. Goykhman, J. B. Khurgin, A. C. Ferrari, and T. J. Kippenberg, *Excitonic Emission of Monolayer Semiconductors Near-Field Coupled to High-Q Microresonators*, Nano Letters **18**, 3138 (2018).
- [55] P. Rivera, J. R. Schaibley, A. M. Jones, J. S. Ross, S. Wu, G. Aivazian, P. Klement, K. Seyler, G. Clark, N. J. Ghimire, J. Yan, D. G. Mandrus, W. Yao, and X. Xu, *Observation of long-lived interlayer excitons in monolayer MoSe<sub>2</sub>-WSe<sub>2</sub> heterostructures*, Nature Communications **6**, 6242 (2015).
- [56] A. F. Rigosi, H. M. Hill, Y. Li, A. Chernikov, and T. F. Heinz, *Probing Interlayer Interactions in Transition Metal Dichalcogenide Heterostructures by Optical Spectroscopy: MoS<sub>2</sub>/WS<sub>2</sub> and MoSe<sub>2</sub>/WSe<sub>2</sub>*, Nano Letters **15**, 5033 (2015).
- [57] L. A. Jauregui, A. Y. Joe, K. Pistunova, D. S. Wild, A. A. High, Y. Zhou, G. Scuri, K. de Greve, A. Sushko, C. H. Yu, T. Taniguchi, K. Watanabe, D. J. Needleman, M. D. Lukin, H. Park, and P. Kim, *Electrical control of interlayer*

## REFERENCES

---

- exciton dynamics in atomically thin heterostructures*, Science **366**, 870 (2019).
- [58] J. Gusakova, X. Wang, L. L. Shiau, A. Krivosheeva, V. Shaposhnikov, V. Borisenko, V. Gusakov, and B. K. Tay, *Electronic Properties of Bulk and Monolayer TMDs: Theoretical Study Within DFT Framework (GVJ-2e Method)*, Physica Status Solidi (A) **214**, 1700218 (2017).
- [59] J. He, I. Paradisanos, T. Liu, A. R. Cadore, J. Liu, M. Churaev, R. N. Wang, A. S. Raja, C. Javerzac-Galy, P. Roelli, D. D. Fazio, B. L. Rosa, S. Tongay, G. Soavi, A. C. Ferrari, and T. J. Kippenberg, *Low-Loss Integrated Nanophotonic Circuits with Layered Semiconductor Materials*, Nano Letters **21**, 2709 (2021).
- [60] O. Karni, E. Barré, S. C. Lau, R. Gillen, E. Y. Ma, B. Kim, K. Watanabe, T. Taniguchi, J. Maultzsch, K. Barmak, R. H. Page, and T. F. Heinz, *Infrared Interlayer Exciton Emission in MoS<sub>2</sub>/WSe<sub>2</sub> Heterostructures*, Physical Review Letters **123**, 247402 (2019).
- [61] Y. Liu, H. Fang, A. Rasmita, Y. Zhou, J. Li, T. Yu, Q. Xiong, N. Zheludev, J. Liu, and W. Gao, *Room temperature nanocavity laser with interlayer excitons in 2D heterostructures*, Science Advances **5**, eaav4506 (2019).
- [62] E. Y. Paik, L. Zhang, G. W. Burg, R. Gogna, E. Tutuc, and H. Deng, *Interlayer exciton laser with extended spatial coherence in an atomically-thin heterostructure*, Nature **576**, 80 (2019).
- [63] X. Gan, R. J. Shiue, Y. Gao, I. Meric, T. F. Heinz, K. Shepard, J. Hone, S. Assefa, and D. Englund, *Chip-integrated ultrafast graphene photodetector with high responsivity*, Nature Photonics **7**, 883 (2013).
- [64] S. Schuler, J. E. Muench, A. Ruocco, O. Balci, D. v. Thourhout, V. Sorianello, M. Romagnoli, K. Watanabe, T. Taniguchi, I. Goykhman, A. C. Ferrari, and T. Mueller, *High-responsivity graphene photodetectors integrated on silicon microring resonators*, Nature Communications **12**, 3733 (2021).
- [65] T. Ren, P. Song, J. Chen, and K. P. Loh, *Whisper Gallery Modes in Monolayer Tungsten Disulfide-Hexagonal Boron Nitride Optical Cavity*, ACS Photonics **5**, 353 (2018).
- [66] K. Parto, S. I. Azzam, N. Lewis, S. D. Patel, S. Umezawa, K. Watanabe, T. Taniguchi, and G. Moody, *Cavity-Enhanced 2D Material Quantum Emitters Deterministically Integrated with Silicon Nitride Microresonators*, Nano Letters **22**, 9748 (2022).
- [67] T. Ren and K. P. Loh, *On-chip integrated photonic circuits based on two-dimensional materials and hexagonal boron nitride as the optical confinement layer*, Journal of Applied Physics **125**, 230901 (2019).
- [68] S. Kim, J. E. Fröch, J. Christian, M. Straw, J. Bishop, D. Totonjian, K. Watanabe, T. Taniguchi, M. Toth, and I. Aharonovich, *Photonic crystal cavities from*

- hexagonal boron nitride*, Nature Communications **9**, 2623 (2018).
- [69] J. E. Fröch, Y. Hwang, S. Kim, I. Aharonovich, and M. Toth, *Photonic Nanostructures from Hexagonal Boron Nitride*, Advanced Optical Materials **7**, 1801344 (2019).
- [70] N. Lassaline, D. Thureja, T. Chervy, D. Petter, P. A. Murthy, A. W. Knoll, and D. J. Norris, *Freeform Electronic and Photonic Landscapes in Hexagonal Boron Nitride*, Nano Letters **21**, 8175 (2021).
- [71] C. Li, J. E. Fröch, M. Nonahal, T. N. Tran, M. Toth, S. Kim, and I. Aharonovich, *Integration of hBN Quantum Emitters in Monolithically Fabricated Waveguides*, ACS Photonics **8**, 2966 (2021).
- [72] J. E. Fröch, C. Li, Y. Chen, M. Toth, M. Kianinia, S. Kim, and I. Aharonovich, *Purcell Enhancement of a Cavity-Coupled Emitter in Hexagonal Boron Nitride*, Small **18**, 2104805 (2022).
- [73] R. Khelifa, P. Back, N. Flöry, S. Nashashibi, K. Malchow, T. Taniguchi, K. Watanabe, A. Jain, and L. Novotny, *Coupling Interlayer Excitons to Whispering Gallery Modes in van der Waals Heterostructures*, Nano Letters **20**, 6155 (2020).
- [74] P. Ajayan, P. Kim, and K. Banerjee, *Two-dimensional van der Waals materials*, Physics Today **69**, 38 (2016).
- [75] K. S. Novoselov, A. Geim, S. V. Morozov, D. Jiang, Y. Zhang, S. V. Dubonos, I. V. Grigorieva, and A. A. Firsov, *Electric Field Effect in Atomically Thin Carbon Films*, **306**, 666 (2004).
- [76] Y. Huang, E. Sutter, N. N. Shi, J. Zheng, T. Yang, D. Englund, H. J. Gao, and P. Sutter, *Reliable Exfoliation of Large-Area High-Quality Flakes of Graphene and Other Two-Dimensional Materials*, ACS Nano **9**, 10612 (2015).
- [77] T.-A. Chen, C. P. Chuu, C. C. Tseng, C. K. Wen, H. S. Wong, S. Pan, R. Li, T. A. Chao, W. C. Chueh, Y. Zhang, Q. Fu, B. I. Yakobson, W. H. Chang, and L. J. Li, *Wafer-scale single-crystal hexagonal boron nitride monolayers on Cu (111)*, Nature **579**, 219 (2020).
- [78] F. G. Aras, A. Yilmaz, H. G. Tasdelen, A. Ozden, F. Ay, N. K. Perkgoz, and A. Yeltik, *A review on recent advances of chemical vapor deposition technique for monolayer transition metal dichalcogenides ( $MX_2$ : Mo, W; S, Se, Te)*, Materials Science in Semiconductor Processing **148**, 106829 (2022).
- [79] K. S. Novoselov, A. K. Geim, S. V. Morozov, D. Jiang, M. I. Katsnelson, I. V. Grigorieva, S. V. Dubonos, and A. A. Firsov, *Two-dimensional gas of massless Dirac fermions in graphene*, Nature **438**, 197 (2005).
- [80] *It's still all about graphene*, Nature Materials **10**, 1 (2011).
- [81] S. Manzeli, D. Ovchinnikov, D. Pasquier, O. V. Yazyev, and A. Kis, *2D transition*

## REFERENCES

---

- metal dichalcogenides*, Nature Reviews Materials **2**, 17033 (2017).
- [82] M. J. Molaei, M. Younas, and M. Rezakazemi, *A Comprehensive Review on Recent Advances in Two-Dimensional (2D) Hexagonal Boron Nitride*, ACS Applied Electronic Materials **3**, 5165 (2021).
- [83] A. A. Balandin, S. Ghosh, W. Bao, I. Calizo, D. Teweldebrhan, F. Miao, and C. N. Lau, *Superior Thermal Conductivity of Single-Layer Graphene*, Nano Letters **8**, 902 (2008).
- [84] K. Cao, S. Feng, Y. Han, L. Gao, T. Hue Ly, Z. Xu, and Y. Lu, *Elastic straining of free-standing monolayer graphene*, Nature Communications **11**, 284 (2020).
- [85] A. H. Castro Neto, F. Guinea, N. M. Peres, K. S. Novoselov, and A. K. Geim, *The electronic properties of graphene*, Reviews of Modern Physics **81**, 109 (2009).
- [86] A. S. Mayorov, R. V. Gorbachev, S. V. Morozov, L. Britnell, R. Jalil, L. A. Ponomarenko, P. Blake, K. S. Novoselov, K. Watanabe, T. Taniguchi, and A. K. Geim, *Micrometer-Scale Ballistic Transport in Encapsulated Graphene at Room Temperature*, Nano Letters **11**, 2396 (2011).
- [87] L. Banszerus, M. Schmitz, S. Engels, M. Goldsche, K. Watanabe, T. Taniguchi, B. Beschoten, and C. Stampfer, *Ballistic Transport Exceeding 28  $\mu\text{m}$  in CVD Grown Graphene*, Nano Letters **16**, 1387 (2016).
- [88] Y. D. Kim, Y. Gao, R. J. Shiue, L. Wang, O. B. Aslan, M. H. Bae, H. Kim, D. Seo, H. J. Choi, S. H. Kim, A. Nemilentsau, T. Low, C. Tan, D. K. Efetov, T. Taniguchi, K. Watanabe, K. L. Shepard, T. F. Heinz, D. Englund, and J. Hone, *Ultrafast Graphene Light Emitters*, Nano Letters **18**, 934 (2018).
- [89] N. Flöry, *Waveguide-integration of 2D heterostructures for high-speed photodetection*, PhD thesis, ETH Zürich, 2019.
- [90] R. R. Nair, P. Blake, A. N. Grigorenko, K. S. Novoselov, T. J. Booth, T. Stauber, N. M. Peres, and A. K. Geim, *Fine Structure Constant Defines Visual Transparency of Graphene*, Science **320**, 1308 (2008).
- [91] K. F. Mak, J. Shan, and T. F. Heinz, *Seeing Many-Body Effects in Single- and Few-Layer Graphene: Observation of Two-Dimensional Saddle-Point Excitons*, Physical Review Letters **106**, 046401 (2011).
- [92] B. Song, H. Gu, S. Zhu, H. Jiang, X. Chen, C. Zhang, and S. Liu, *Broadband optical properties of graphene and HOPG investigated by spectroscopic Mueller matrix ellipsometry*, Applied Surface Science **439**, 1079 (2018).
- [93] Y. Rah, Y. Jin, S. Kim, and K. Yu, *Optical analysis of the refractive index and birefringence of hexagonal boron nitride from the visible to near-infrared*, Optics Letters **44**, 3797 (2019).
- [94] J. D. Caldwell, I. Aharonovich, G. Cassabois, J. H. Edgar, B. Gil, and D. N.

- Basov, *Photonics with hexagonal boron nitride*, Nature Reviews Materials **4**, 552 (2019).
- [95] K. Watanabe, T. Taniguchi, and H. Kanda, *Direct-bandgap properties and evidence for ultraviolet lasing of hexagonal boron nitride single crystal*, Nature Materials **3**, 404 (2004).
- [96] G. Cassabois, P. Valvin, and B. Gil, *Hexagonal boron nitride is an indirect bandgap semiconductor*, Nature Photonics **10**, 262 (2016).
- [97] M. Ishigami, J. H. Chen, W. G. Cullen, M. S. Fuhrer, and E. D. Williams, *Atomic structure of graphene on SiO<sub>2</sub>*, Nano Letters **7**, 1643 (2007).
- [98] C. R. Dean, A. F. Young, I. Meric, C. Lee, L. Wang, S. Sorgenfrei, K. Watanabe, T. Taniguchi, P. Kim, K. L. Shepard, and J. Hone, *Boron nitride substrates for high-quality graphene electronics*, Nature Nanotechnology **5**, 722 (2010).
- [99] G. Mirabelli, C. McGeough, M. Schmidt, E. K. McCarthy, S. Monaghan, I. M. Povey, M. McCarthy, F. Gity, R. Nagle, G. Hughes, A. Cafolla, P. K. Hurley, and R. Duffy, *Air sensitivity of MoS<sub>2</sub>, MoSe<sub>2</sub>, MoTe<sub>2</sub>, HfS<sub>2</sub>, and HfSe<sub>2</sub>*, Journal of Applied Physics **120**, 125102 (2016).
- [100] Y. Cao et al., *Quality Heterostructures from Two-Dimensional Crystals Unstable in Air by Their Assembly in Inert Atmosphere*, Nano Letters **15**, 4914 (2015).
- [101] G. H. Lee, X. Cui, Y. D. Kim, G. Arefe, X. Zhang, C. H. Lee, F. Ye, K. Watanabe, T. Taniguchi, P. Kim, and J. Hone, *Highly Stable, Dual-Gated MoS<sub>2</sub> Transistors Encapsulated by Hexagonal Boron Nitride with Gate-Controllable Contact, Resistance, and Threshold Voltage*, ACS Nano **9**, 7019 (2015).
- [102] F. Cadiz, E. Courtade, C. Robert, G. Wang, Y. Shen, H. Cai, T. Taniguchi, K. Watanabe, H. Carrere, D. Lagarde, M. Manca, T. Amand, P. Renucci, S. Tongay, X. Marie, and B. Urbaszek, *Excitonic Linewidth Approaching the Homogeneous Limit in MoS<sub>2</sub>-Based van der Waals Heterostructures*, Physical Review X **7**, 021026 (2017).
- [103] G. H. Lee, Y. J. Yu, C. Lee, C. Dean, K. L. Shepard, P. Kim, and J. Hone, *Electron tunneling through atomically flat and ultrathin hexagonal boron nitride*, Applied Physics Letters **99**, 243114 (2011).
- [104] L. Britnell, R. V. Gorbachev, R. Jalil, B. D. Belle, F. Schedin, M. I. Katsnelson, L. Eaves, S. V. Morozov, A. S. Mayorov, N. M. Peres, A. H. Castro Neto, J. Leist, A. K. Geim, L. A. Ponomarenko, and K. S. Novoselov, *Electron Tunneling through Ultrathin Boron Nitride Crystalline Barriers*, Nano Letters **12**, 1707 (2012).
- [105] M. Parzefall, P. Bharadwaj, A. Jain, T. Taniguchi, K. Watanabe, and L. Novotny, *Antenna-coupled photon emission from hexagonal boron nitride tunnel junctions*, Nature Nanotechnology **10**, 1058 (2015).

## REFERENCES

---

- [106] M. Parzefall, Á. Szabó, T. Taniguchi, K. Watanabe, M. Luisier, and L. Novotny, *Light from van der Waals quantum tunneling devices*, Nature Communications **10**, 292 (2019).
- [107] S. Adachi, *Optical Constants of Crystalline and Amorphous Semiconductors*, Springer, 1999.
- [108] T. T. Tran, K. Bray, M. J. Ford, M. Toth, and I. Aharonovich, *Quantum emission from hexagonal boron nitride monolayers*, Nature Nanotechnology **11**, 37 (2016).
- [109] T. Mueller and E. Malic, *Exciton physics and device application of two-dimensional transition metal dichalcogenide semiconductors*, npj 2D Materials and Applications **2**, 29 (2018).
- [110] R. Khelifa, S. Shan, A. J. Moilanen, T. Taniguchi, K. Watanabe, and L. Novotny, *WSe<sub>2</sub> Light-Emitting Device Coupled to an h-BN Waveguide*, ACS Photonics **10**, 1328 (2023).
- [111] G. H. Jung, S. J. Yoo, and Q. H. Park, *Measuring the optical permittivity of twodimensional materials without a priori knowledge of electronic transitions*, Nanophotonics **8**, 263 (2019).
- [112] A. Chernikov, T. C. Berkelbach, H. M. Hill, A. Rigosi, Y. Li, O. B. Aslan, D. R. Reichman, M. S. Hybertsen, and T. F. Heinz, *Exciton binding energy and nonhydrogenic Rydberg series in monolayer WS<sub>2</sub>*, Physical Review Letters **113**, 076802 (2014).
- [113] K. He, N. Kumar, L. Zhao, Z. Wang, K. F. Mak, H. Zhao, and J. Shan, *Tightly bound excitons in monolayer WSe<sub>2</sub>*, Physical Review Letters **113**, 026803 (2014).
- [114] G. Wang, A. Chernikov, M. M. Glazov, T. F. Heinz, X. Marie, T. Amand, and B. Urbaszek, *Colloquium: Excitons in atomically thin transition metal dichalcogenides*, Reviews of Modern Physics **90**, 021001 (2018).
- [115] J. P. Echeverry, B. Urbaszek, T. Amand, X. Marie, and I. C. Gerber, *Splitting between bright and dark excitons in transition metal dichalcogenide monolayers*, Physical Review B **93**, 1 (2016).
- [116] J. S. Ross, S. Wu, H. Yu, N. J. Ghimire, A. M. Jones, G. Aivazian, J. Yan, D. G. Mandrus, D. Xiao, W. Yao, and X. Xu, *Electrical control of neutral and charged excitons in a monolayer semiconductor*, Nature Communications **4**, 1474 (2013).
- [117] K. F. Mak, K. He, C. Lee, G. H. Lee, J. Hone, T. F. Heinz, and J. Shan, *Tightly bound trions in monolayer MoS<sub>2</sub>*, Nature Materials **12**, 207 (2013).
- [118] J. A. Schuller, S. Karaveli, T. Schiros, K. He, S. Yang, I. Kymissis, J. Shan, and R. Zia, *Orientation of luminescent excitons in layered nanomaterials*, Nature

- Nanotechnology **8**, 271 (2013).
- [119] M. Brotons-Gisbert, R. Proux, R. Picard, D. Andres-Penares, A. Branny, A. Molina-Sánchez, J. F. Sánchez-Royo, and B. D. Gerardot, *Out-of-plane orientation of luminescent excitons in two-dimensional indium selenide*, Nature Communications **10**, 3913 (2019).
- [120] M. Bernardi, M. Palummo, and J. C. Grossman, *Extraordinary sunlight absorption and one nanometer thick photovoltaics using two-dimensional monolayer materials*, Nano Letters **13**, 3664 (2013).
- [121] Y. Li, A. Chernikov, X. Zhang, A. Rigosi, H. M. Hill, A. M. Van Der Zande, D. A. Chenet, E. M. Shih, J. Hone, and T. F. Heinz, *Measurement of the optical dielectric function of monolayer transition-metal dichalcogenides:  $MoS_2$ ,  $MoSe_2$ ,  $WS_2$ , and  $WSe_2$* , Physical Review B **90**, 205422 (2014).
- [122] J. Kim, C. Jin, B. Chen, H. Cai, T. Zhao, P. Lee, S. Kahn, K. Watanabe, T. Taniguchi, S. Tongay, M. F. Crommie, and F. Wang, *Observation of ultralong valley lifetime in  $WSe_2/MoS_2$  heterostructures*, Science Advances **3**, e1700518 (2017).
- [123] D. Unuchek, A. Ciarrocchi, A. Avsar, K. Watanabe, T. Taniguchi, and A. Kis, *Room-temperature electrical control of exciton flux in a van der Waals heterostructure*, Nature **560**, 340 (2018).
- [124] K. Kosmider and J. Fernández-Rossier, *Electronic properties of the  $MoS_2$ - $WS_2$  heterojunction*, Physical Review B **87**, 075451 (2013).
- [125] C. Zhang, C. P. Chuu, X. Ren, M. Y. Li, L. J. Li, C. Jin, M. Y. Chou, and C. K. Shih, *Interlayer couplings, Moiré patterns, and 2D electronic superlattices in  $MoS_2/WSe_2$  hetero-bilayers*, Science Advances **3**, e1601459 (2017).
- [126] L. Sigl, M. Troue, M. Katzer, M. Selig, F. Sigger, J. Kiemle, M. Brotons-Gisbert, K. Watanabe, T. Taniguchi, B. D. Gerardot, A. Knorr, U. Wurstbauer, and A. W. Holleitner, *Optical dipole orientation of interlayer excitons in  $MoSe_2$ - $WSe_2$  heterostacks*, Physical Review B **105**, 035417 (2022).
- [127] M. Förg, L. Colombier, R. K. Patel, J. Lindlau, A. D. Mohite, H. Yamaguchi, M. M. Glazov, D. Hunger, and A. Högele, *Cavity-control of interlayer excitons in van der Waals heterostructures*, Nature Communications **10**, 3697 (2019).
- [128] E. Barré, O. Karni, E. Liu, A. L. O’Beirne, X. Chen, H. B. Ribeiro, L. Yu, B. Kim, K. Watanabe, T. Taniguchi, K. Barmak, C. H. Lui, S. Refaely-Abramson, F. H. da Jornada, and T. F. Heinz, *Optical absorption of interlayer excitons in transition-metal dichalcogenide heterostructures*, Science **376**, 406 (2022).
- [129] J. S. Ross, P. Rivera, J. Schaibley, E. Lee-Wong, H. Yu, T. Taniguchi, K. Watanabe, J. Yan, D. Mandrus, D. Cobden, W. Yao, and X. Xu, *Interlayer Exciton Optoelectronics in a 2D Heterostructure p-n Junction*, Nano Letters **17**,

## REFERENCES

---

- 638 (2017).
- [130] J. Binder, F. Withers, M. R. Molas, C. Faugeras, K. Nogajewski, K. Watanabe, T. Taniguchi, A. Kozikov, A. K. Geim, K. S. Novoselov, and M. Potemski, *Sub-bandgap Voltage Electroluminescence and Magneto-oscillations in a WSe<sub>2</sub> Light-Emitting van der Waals Heterostructure*, *Nano Letters* **17**, 1425 (2017).
- [131] Y. Lian, D. Lan, S. Xing, B. Guo, Z. Ren, R. Lai, C. Zou, B. Zhao, R. H. Friend, and D. Di, *Ultralow-voltage operation of light-emitting diodes*, *Nature Communications* **13**, 3845 (2022).
- [132] S. Papadopoulos, L. Wang, T. Taniguchi, K. Watanabe, and L. Novotny, *Energy transfer from tunneling electrons to excitons*, arXiv preprint , arXiv:2209.11641 (2022).
- [133] S. Shan, J. Huang, S. Papadopoulos, R. Khelifa, T. Taniguchi, K. Watanabe, L. Wang, and L. Novotny, *Overbias photon emission from light-emitting devices based on monolayer transition metal dichalcogenides*, arXiv preprint , arXiv:2303.00363 (2023).
- [134] J. Binder, J. Howarth, F. Withers, M. R. Molas, T. Taniguchi, K. Watanabe, C. Faugeras, A. Wyszomolek, M. Danovich, V. I. Falko, A. K. Geim, K. S. Novoselov, M. Potemski, and A. Kozikov, *Upconverted electroluminescence via Auger scattering of interlayer excitons in van der Waals heterostructures*, *Nature Communications* **10**, 2335 (2019).
- [135] R. G. Hunsperger, *Integrated Optics*, Springer, 6th edition, 2009.
- [136] B. E. Saleh and M. C. Teich, *Fundamentals of photonics*, John Wiley & Sons, Inc., 2nd edition, 2007.
- [137] C. R. Pollock and M. Lipson, *Integrated Photonics*, Springer New York, 2003.
- [138] M. R. Escala, *Generation, Modulation and Detection of Light in Lithium Niobate Nanophotonic devices*, PhD thesis, ETH Zürich, 2019.
- [139] U. Koch, *Plasmonic Transmitters - Miniaturization and Parallelization for Co-Integration with Electronics*, PhD thesis, ETH Zürich, 2019.
- [140] O. Lord Rayleigh, *The problem of the whispering gallery*, *The London, Edinburgh, and Dublin Philosophical Magazine and Journal of Science* **20**, 1001 (1910).
- [141] A. L. Gaeta, M. Lipson, and T. J. Kippenberg, *Photonic-chip-based frequency combs*, *Nature Photonics* **13**, 158 (2019).
- [142] N. Toropov, G. Cabello, M. P. Serrano, R. R. Gutha, M. Rafti, and F. Vollmer, *Review of biosensing with whispering-gallery mode lasers*, *Light: Science and Applications* **10**, 42 (2021).
- [143] J. Heebner, R. Grover, and T. Ibrahim, *Optical Microresonators*, Springer, 2008.
- [144] L. Novotny and B. Hecht, *Principles of Nano-Optics*, Cambridge University



- Press, 2nd edition, 2012.
- [145] T. Kippenberg, *Nonlinear Optics in Ultra-high-Q Whispering-Gallery Optical Microcavities*, PhD thesis, California Institute of Technology Pasadena, California, 2004.
- [146] R. E. Slusher, A. F. Levi, U. Mohideen, S. L. McCall, S. J. Pearton, and R. A. Logan, *Threshold characteristics of semiconductor microdisk lasers*, Applied Physics Letters **63**, 1310 (1993).
- [147] M. Mexis, S. Sergent, T. Guillet, C. Brimont, T. Bretagnon, B. Gil, F. Semond, M. Leroux, D. Néel, S. David, X. Chécoury, and P. Boucaud, *High quality factor nitride-based optical cavities: microdisks with embedded GaN/Al(Ga)N quantum dots*, Optics Letters **36**, 2203 (2011).
- [148] A. Yariv, *Critical coupling and its control in optical waveguide-ring resonator systems*, IEEE Photonics Technology Letters **14**, 483 (2002).
- [149] M. Cai, O. Painter, and K. J. Vahala, *Observation of critical coupling in a fiber taper to a silica-microsphere whispering-gallery mode system*, Physical Review Letters **85**, 74 (2000).
- [150] M. Soltani, *Novel Integrated Silicon Nanophotonic Structures using Ultra-high Q Resonators*, PhD thesis, Georgia Institute of Technology, 2009.
- [151] M. Autore, P. Li, I. Dolado, F. J. Alfaro-Mozaz, R. Esteban, A. Atxabal, F. Casanova, L. E. Hueso, P. Alonso-González, J. Aizpurua, A. Y. Nikitin, S. Vélez, and R. Hillenbrand, *Boron nitride nanoresonators for Phonon-Enhanced molecular vibrational spectroscopy at the strong coupling limit*, Light: Science and Applications **7**, 17172 (2018).
- [152] P. Ma, N. Flöry, Y. Salamin, B. Baeuerle, A. Emboras, A. Josten, T. Taniguchi, K. Watanabe, L. Novotny, and J. Leuthold, *Fast MoTe<sub>2</sub> Waveguide Photodetector with High Sensitivity at Telecommunication Wavelengths*, ACS Photonics **5**, 1846 (2018).
- [153] G. Wei, T. K. Stanev, D. A. Czaplewski, I. W. Jung, and N. P. Stern, *Silicon-nitride photonic circuits interfaced with monolayer MoS<sub>2</sub>*, Applied Physics Letters **107**, 091112 (2015).
- [154] L. Huang, A. Krasnok, A. Alú, Y. Yu, D. Neshev, and A. E. Miroshnichenko, *Enhanced light-matter interaction in two-dimensional transition metal dichalcogenides*, Reports on Progress in Physics **85**, 046401 (2022).
- [155] M. Arcari, I. Söllner, A. Javadi, S. Lindskov Hansen, S. Mahmoodian, J. Liu, H. Thyrrstrup, E. H. Lee, J. D. Song, S. Stobbe, and P. Lodahl, *Near-Unity Coupling Efficiency of a Quantum Emitter to a Photonic Crystal Waveguide*, Physical Review Letters **113**, 093603 (2014).
- [156] S. Khasminskaya, F. Pyatkov, K. Słowik, S. Ferrari, O. Kahl, V. Kovalyuk,

## REFERENCES

---

- P. Rath, A. Vetter, F. Hennrich, M. M. Kappes, G. Gol'tsman, A. Korneev, C. Rockstuhl, R. Krupke, and W. H. Pernice, *Fully integrated quantum photonic circuit with an electrically driven light source*, *Nature Photonics* **10**, 727 (2016).
- [157] K. G. Fehler, A. P. Ovvyan, N. Gruhler, W. H. Pernice, and A. Kubanek, *Efficient Coupling of an Ensemble of Nitrogen Vacancy Center to the Mode of a High-Q, Si<sub>3</sub>N<sub>4</sub> Photonic Crystal Cavity*, *ACS Nano* **13**, 6891 (2019).
- [158] L. Liebermeister, *Photonic Waveguides Evanescently Coupled with Single NV-centers*, PhD thesis, Ludwig-Maximilians-Universität München, 2015.
- [159] T. Hoehne, P. Schnauber, S. Rodt, S. Reitzenstein, and S. Burger, *Numerical Investigation of Light Emission from Quantum Dots Embedded into On-Chip, Low-Index-Contrast Optical Waveguides*, *Physica Status Solidi B* **256**, 1800437 (2019).
- [160] M. Parzefall, *Optical Antennas Driven by Quantum Tunneling*, PhD thesis, ETH Zürich, 2017.
- [161] E. M. Purcell, *Spontaneous emission probabilities at radio frequencies*, *Physical Review* **69**, 681 (1946).
- [162] L. Wang, I. Meric, P. Y. Huang, Q. Gao, Y. Gao, H. Tran, T. Taniguchi, K. Watanabe, L. M. Campos, D. A. Muller, J. Guo, P. Kim, J. Hone, K. L. Shepard, and R. C. Dean, *One-Dimensional Electrical Contact to a Two-Dimensional Material*, *Science* **342**, 614 (2013).
- [163] P. J. Zomer, M. H. Guimarães, J. C. Brant, N. Tombros, and B. J. Van Wees, *Fast pick up technique for high quality heterostructures of bilayer graphene and hexagonal boron nitride*, *Applied Physics Letters* **105**, 013101 (2014).
- [164] C. Hsu, R. Frisenda, R. Schmidt, A. Arora, S. M. de Vasconcellos, R. Bratschitsch, H. S. van der Zant, and A. Castellanos-Gomez, *Thickness-Dependent Refractive Index of 1L, 2L, and 3L MoS<sub>2</sub>, MoSe<sub>2</sub>, WS<sub>2</sub>, and WSe<sub>2</sub>*, *Advanced Optical Materials* **7**, 1900239 (2019).
- [165] D. Rosser, T. Fryett, A. Ryou, A. Saxena, and A. Majumdar, *Exciton-phonon interactions in nanocavity-integrated monolayer transition metal dichalcogenides*, *npj 2D Materials and Applications* **4**, 20 (2020).
- [166] D. Rosser, T. Fryett, A. Saxena, A. Ryou, and A. Majumdar, *High-precision local transfer of van der Waals materials on nanophotonic structures*, *Optical Materials Express* **10**, 645 (2020).
- [167] D. Kozawa, R. Kumar, A. Carvalho, K. Kumar Amara, W. Zhao, S. Wang, M. Toh, R. M. Ribeiro, A. H. Castro Neto, K. Matsuda, and G. Eda, *Photocarrier relaxation pathway in two-dimensional semiconducting transition metal dichalcogenides*, *Nature Communications* **5**, 4543 (2014).
- [168] S. Wang, J. Wang, W. Zhao, F. Giustiniano, L. Chu, I. Verzhbitskiy, J. Zhou Yong,

- and G. Eda, *Efficient carrier-to-exciton conversion in field emission tunnel diodes based on MIS-Type van der waals heterostack*, Nano Letters **17**, 5156 (2017).
- [169] C. Wang, F. Yang, and Y. Gao, *The highly-efficient light-emitting diodes based on transition metal dichalcogenides: From architecture to performance*, Nanoscale Advances **2**, 4323 (2020).
- [170] R. Cheng, D. Li, H. Zhou, C. Wang, A. Yin, S. Jiang, Y. Liu, Y. Chen, Y. Huang, and X. Duan, *Electroluminescence and photocurrent generation from atomically sharp  $WSe_2/MoS_2$  heterojunction p-n diodes*, Nano Letters **14**, 5590 (2014).
- [171] R. J. Peña Román, D. Pommier, R. Bretel, L. E. Parra López, E. Lorchat, J. Chaste, A. Ouerghi, S. Le Moal, E. Boer-Duchemin, G. Dujardin, A. G. Borisov, L. F. Zagonel, G. Schull, S. Berciaud, and E. Le Moal, *Electroluminescence of monolayer  $WS_2$  in a scanning tunneling microscope: Effect of bias polarity on spectral and angular distribution of emitted light*, Physical Review B **106**, 085419 (2022).
- [172] H. Overweg, H. Eggimann, X. Chen, S. Slizovskiy, M. Eich, R. Pisoni, Y. Lee, P. Rickhaus, K. Watanabe, T. Taniguchi, V. Fal'Ko, T. Ihn, and K. Ensslin, *Electrostatically Induced Quantum Point Contacts in Bilayer Graphene*, Nano Letters **18**, 553 (2018).
- [173] A. Jain, Á. Szabó, M. Parzefall, E. Bonvin, T. Taniguchi, K. Watanabe, P. Bharadwaj, M. Luisier, and L. Novotny, *One-Dimensional Edge Contacts to a Monolayer Semiconductor*, Nano Letters **19**, 6914 (2019).
- [174] F. Giubileo and A. Di Bartolomeo, *The role of contact resistance in graphene field-effect devices*, Progress in Surface Science **92**, 143 (2017).
- [175] Y. Fu, T. Ye, W. Tang, and T. Chu, *Efficient adiabatic silicon-on-insulator waveguide taper*, Photonics Research **2**, A41 (2014).
- [176] N. M. Andrade, S. Hooten, S. A. Fortuna, K. Han, E. Yablonovitch, and M. C. Wu, *Inverse design optimization for efficient coupling of an electrically injected optical antenna-LED to a single-mode waveguide*, Optics Express **27**, 19802 (2019).
- [177] F. Bailly, T. David, T. Chevolleau, M. Darnon, N. Posseme, R. Bouyssou, J. Ducote, O. Joubert, and C. Cardinaud, *Roughening of porous SiCOH materials in fluorocarbon plasmas*, Journal of Applied Physics **108**, 014906 (2010).
- [178] P. K. Tien, *Light Waves in Thin Films and Integrated Optics*, Applied Optics **10**, 2395 (1971).
- [179] F. P. Payne and J. P. Lacey, *A theoretical analysis of scattering loss from planar optical waveguides*, Optical and Quantum Electronics **26**, 977 (1994).
- [180] X. Ji, S. Roberts, M. Corato-Zanarella, and M. Lipson, *Methods to achieve ultra-high quality factor silicon nitride resonators*, APL Photonics **6**, 071101

## REFERENCES

---

- (2021).
- [181] X. Ji, J. K. Jang, U. D. Dave, M. Corato-Zanarella, C. Joshi, A. L. Gaeta, and M. Lipson, *Exploiting Ultralow Loss Multimode Waveguides for Broadband Frequency Combs*, *Laser and Photonics Reviews* **15**, 2000353 (2021).
- [182] A. Salehi, X. Fu, D. H. Shin, and F. So, *Recent Advances in OLED Optical Design*, *Advanced Functional Materials* **29**, 1808803 (2019).
- [183] M. Amani, D. H. Lien, D. Kiriya, J. Xiao, A. Azcatl, J. Noh, S. R. Madhupathy, R. Addou, K. C. Santosh, M. Dubey, K. Cho, R. M. Wallace, S. C. Lee, J. H. He, J. W. Ager, X. Zhang, E. Yablonovitch, and A. Javey, *Near-unity photoluminescence quantum yield in MoS<sub>2</sub>*, *Science* **350**, 1065 (2015).
- [184] D. H. Lien, S. Z. Uddin, M. Yeh, M. Amani, H. Kim, J. W. Ager, E. Yablonovitch, and A. Javey, *Electrical suppression of all nonradiative recombination pathways in monolayer semiconductors*, *Science* **364**, 468 (2019).
- [185] H. Kim, S. Z. Uddin, N. Higashitarumizu, E. Rabani, and A. Javey, *Inhibited nonradiative decay at all exciton densities in monolayer semiconductors*, *Science* **373**, 448 (2021).
- [186] S. Z. Uddin, N. Higashitarumizu, H. Kim, I. K. Rahman, and A. Javey, *Efficiency Roll-Off Free Electroluminescence from Monolayer WSe<sub>2</sub>*, *Nano Letters* **22**, 5316 (2022).
- [187] S. Negi, P. Mittal, and B. Kumar, *Impact of different layers on performance of OLED*, *Microsystem Technologies* **24**, 4981 (2018).
- [188] S. Busschaert, R. Reimann, M. Cavigelli, R. Khelifa, A. Jain, and L. Novotny, *Transition Metal Dichalcogenide Resonators for Second Harmonic Signal Enhancement*, *ACS Photonics* **7**, 2482 (2020).
- [189] S. Shan, *Fabrication and Characterization of hBN Photonic Crystal Cavity*, Master Thesis, ETH Zürich, 2021.
- [190] I. Datta, S. H. Chae, G. R. Bhatt, B. Li, Y. Yu, L. Cao, J. Hone, and M. Lipson, *Giant electro-refractive modulation of monolayer WS<sub>2</sub> embedded in photonic structures*, in *Conference on Lasers and Electro-Optics*, page STu4N.7, Optica Publishing Group, 2018.
- [191] N. Mounet, M. Gibertini, P. Schwaller, D. Campi, A. Merkys, A. Marrazzo, T. Sohler, I. E. Castelli, A. Cepellotti, G. Pizzi, and N. Marzari, *Two-dimensional materials from high-throughput computational exfoliation of experimentally known compounds*, *Nature Nanotechnology* **13**, 246 (2018).
- [192] H. Ling, R. Li, and A. R. Davoyan, *All van der Waals Integrated Nanophotonics with Bulk Transition Metal Dichalcogenides*, *ACS Photonics* **8**, 721 (2021).
- [193] B. Munkhbat, B. Küçüköz, D. G. Baranov, T. J. Antosiewicz, and T. O. Shegai, *Nanostructured transition metal dichalcogenide multilayers for advanced*

- nanophotonics*, Laser & Photonics Reviews , 2200057 (2022).
- [194] D. Bajoni, E. Semenova, A. Lemaître, S. Bouchoule, E. Wertz, P. Senellart, and J. Bloch, *Polariton light-emitting diode in a GaAs-based microcavity*, Physical Review B **77**, 113303 (2008).
- [195] C. Schneider, A. Rahimi-iman, N. Y. Kim, J. Fischer, I. G. Savenko, M. Amthor, M. Lermer, A. Wolf, L. Worschech, V. D. Kulakovskii, I. A. Shelykh, and M. Kamp, *An electrically pumped polariton laser*, Nature **497**, 348 (2013).
- [196] J. S. Lee, S. H. Choi, S. J. Yun, Y. I. Kim, S. Boandoh, J. H. Park, B. G. Shin, H. Ko, S. H. Lee, Y. M. Kim, Y. H. Lee, K. K. Kim, and S. M. Kim, *Wafer-scale single-crystal hexagonal boron nitride film via self-collimated grain formation*, Science **362**, 817 (2018).
- [197] R. Sun, M. Beals, A. Pomerene, J. Cheng, C.-y. Hong, L. Kimerling, and J. Michel, *Impedance matching vertical optical waveguide couplers for dense high index contrast circuits*, Optics Express **16**, 11682 (2008).
- [198] D. Van Thourhout, G. Roelkens, R. Baets, W. Bogaerts, J. Brouckaert, P. Debackere, P. Dumon, S. Scheerlinck, J. Schrauwen, D. Taillaert, F. Van Laere, and J. Van Campenhout, *Coupling mechanisms for a heterogeneous silicon nanowire platform*, Semiconductor Science and Technology **23**, 064004 (2008).
- [199] A. Jain, P. Bharadwaj, S. Heeg, M. Parzefall, T. Taniguchi, K. Watanabe, and L. Novotny, *Minimizing residues and strain in 2D materials transferred from PDMS*, Nanotechnology **29**, 265203 (2018).
- [200] K. Srinivasan, M. Borselli, O. Painter, A. Stintz, and S. Krishna, *Cavity  $Q$ , mode volume, and lasing threshold in small diameter AlGaAs microdisks with embedded quantum dots*, Optics Express **14**, 1094 (2006).



---

## List of Publication

### **This thesis is based in part on the following publications:**

**R. Khelifa**, P. Back, N. Flöry, S. Nashashibi, K. Malchow, T. Taniguchi, K. Watanabe and L. Novotny. *Coupling Interlayer Excitons to Whispering Gallery Modes in van der Waals Heterostructures*, *Nano Letters*, **20**, 6155-6161 (2020).

**R. Khelifa\***, S. Shan\*, A. J. Moilanen, T. Taniguchi, K. Watanabe and L. Novotny. *WSe<sub>2</sub> Light-Emitting Device Coupled to an h-BN Waveguide*, *ACS Photonics*, **10**, 1328-1333 (2023).

### **Other publications by the author:**

**R. Khelifa**, N. Flöry, S. Nashashibi, K. Malchow, M. Parzefall, A. Jain, T. Taniguchi, K. Watanabe and L. Novotny. *Waveguide-Coupled Disk Resonators Fabricated from Hexagonal Boron Nitride*, in *Light-Matter Interactions Towards the Nanoscale. NATO Science for Peace and Security Series B: Physics and Biophysics*, edited by M. Cesaria, A. Calà Lesina, J. Collins, pages 325-327, Springer, Dordrecht (2022).

S. Busschaert, R. Reimann, M. Cavigelli, **R. Khelifa**, A. Jain and L. Novotny, *Transition Metal Dichalcogenide Resonators for Second Harmonic Signal Enhancement*, *ACS Photonics* **7**, 2482-2488 (2020).

---

\*These two authors contributed equally.

## List of Publication

---

S. Shan\*, J. Huang\*, S. Papadopoulos, **R. Khelifa**, T. Taniguchi, K. Watanabe, L. Wang, L. Novotny, *Overbias photon emission from light-emitting devices based on monolayer transition metal dichalcogenides*, arXiv:2303.00363 (2023), under review.

---

\*These two authors contributed equally.